Chem Soc Rev

REVIEW ARTICLE

View Article Online
View Journal



Cite this: DOI: 10.1039/d5cs01179e

# Intelligent optoelectronics and electronics based on electrospinning technology

Shuwen Xin,[a] You Meng,*[ab] Li Ni,[a] Aolin Wang,[a] Jinwei Pu,[a] Siyuan Wu,[a] Xin Peng,[a] Yujin Liu,[a] Kun Tang,[a] Zhengxun Lai,[a] He Shao*[b] and Johnny C. Ho*[bc]

Electrospinning (ES) has emerged as a cutting-edge technology for the development of next-generation intelligent optoelectronics and flexible electronics, thanks to its high-throughput production capabilities, structural versatility, and multifunctional potential. Electrospun nanofibers (NFs), characterized by their high specific surface area, structural adaptability, and customizable properties, present a compelling alternative to conventional materials and fabrication strategies. Despite notable research advancements, a systematic understanding of the optimization of structure–property relationships and scalable integration techniques for ES-based intelligent (opto)electronic devices remains lacking. In this review, we provide a comprehensive summary of recent advances in ES NFs for intelligent electronic and optoelectronic systems, including photodetectors, synaptic devices, transistors, and gas sensors. Next, we critically analyze mechanisms for property modulation *via* control of crystallinity, defect engineering, and heterostructure design, demonstrating how these microscale strategies enhance device performance and multifunctionality. Furthermore, we discuss broader implications and persistent technological bottlenecks in ES technology, identifying key opportunities for future research. Finally, we emphasize the need for precise multi-scale engineering and innovative designs to advance ES NFs toward intelligent, multifunctional, and commercially viable applications.

Received 2nd January 2026

DOI: 10.1039/d5cs01179e

rsc.li/chem-soc-rev



[a] National Key Laboratory of Power Semiconductor and Integration Technology, Engineering Research Center of Advanced Semiconductor Technology and Application of Ministry of Education, College of Semiconductors (College of Integrated Circuits), Hunan University, Changsha 410082, China
[b] Department of Materials Science and Engineering and State Key Laboratory of Terahertz and Millimeter Waves, City University of Hong Kong, Hong Kong 999077, China. E-mail: johnnyho@cityu.edu.hk
[c] Institute for Materials Chemistry and Engineering, Kyushu University, Fukuoka 816 8580, Japan

## 1. Introduction

With the rapid development of advanced technologies such as artificial intelligence, autonomous driving, and wearable electronics, optoelectronic and electronic devices are evolving toward miniaturization, high integration, and multifunctionality.[1–5] To meet the needs of diverse application scenarios, industry production demands higher requirements on electrical conductivity, structural stability, and material flexibility.[6–8] Therefore,

**Shuwen Xin**

*Shuwen Xin received her bachelor's degree in 2021 from Nantong University and her master's degree in 2024 from Qingdao University. Now she is a PhD student at the College of Semiconductor (College of Integrated Circuit), Hunan University, under the supervision of Prof. You Meng. Her research focuses on low-dimensional optoelectronic devices.*

**You Meng**

*Dr You Meng is a Professor at the College of Semiconductor (College of Integrated Circuit), Hunan University. He received his BS degree in Applied Physics and MS degree in Physics from Qingdao University in 2015 and 2018, respectively, and a PhD degree in Materials Science and Engineering from the City University of Hong Kong in 2021. His research interests mainly focus on nanomaterial-based electronics and circuits.*

developing material systems with precise spatial control and synergistic functional integration has become a key scientific challenge. While conventional methods offer stability, they often struggle to integrate multi-dimensional heterostructures seamlessly, which are essential for next-generation electronics.

Electrospun nanofibers (NFs), due to their high specific surface area, excellent flexibility, and favorable electrical properties, have become fundamental building blocks for constructing high-performance devices.[9–12] Various techniques have been developed for fabricating 1D materials, such as chemical vapor deposition and template-assisted methods.[13,14] However, these methods often suffer from limitations, including the need for complex equipment, high costs, and limited process control. In contrast, electrospinning (ES) is a simple, low-cost, highly versatile method well-suited for fabricating 1D NFs with diverse structures and functions. ES enables efficient production of NFs and offers tunable processing parameters (such as solution composition, nozzle design, and collector configuration), allowing for precise control over the materials' morphology, structure, and performance.[15–17] Critically, ES bridges the gap between bottom-up molecular design and top-down structural assembly, providing a unique platform for engineering charge transport at the nanoscale. Based on these advantages, the ES technique shows great promise for high-performance device integration and functional customization. It has been widely explored in fields such as optoelectronics, flexible sensing, and energy conversion.[18–20]

To date, hundreds of kinds of polymers, inorganic compounds, and 1D composite materials have been successfully fabricated using ES techniques.[21,22] The composition of electrospun fibers is diverse and can be tailored through the combination of polymers, colloids, small molecules, and composites to suit specific physical and electrical properties for various applications.[23,24] For example, adjusting the grain size of NFs by modulating the element ratio allows a transition from semiconductor to conductor behavior, enabling the construction of all-ES electronic devices.[25] Moreover, electrospun fibers exhibit a variety of structural configurations, with core–shell NFs being the most representative example.[26–28] This type of structure reflects a microscopic heterostructure within a single fiber and is typically achieved through coaxial ES. Beyond the microscale, spatial heterostructures can also be constructed by modifying the injection setup to enable the interweaving of fibers with different compositions.[29,30] This macroscopic heterostructure enables hierarchical material design, further expanding the potential of ES in specific device architectures.

With continued research, ES has been applied to fabricate a wide range of 1D nanomaterials for advanced devices such as photodetectors, synaptic devices, and gas sensors (as discussed in the following sections).[30–37] These studies demonstrate the great potential of ES technology for electronic and optoelectronic devices. Despite these advances, most current research still focuses on specific material systems or single-device types, lacking comparative studies across different device categories fabricated by ES. Moreover, systematic strategies for constructing structure-determined and/or interface-driven ES-based intelligent (opto)electronic devices are still lacking. Therefore, a comprehensive review is needed to summarize the structural features, performance improvements, and application routes of ES NFs in intelligent electronic and optoelectronic devices. This will provide valuable theoretical insights and practical guidance for future research and the development of ES devices.

In this review, we focus on the recent advances in ES NFs for intelligent electronic and optoelectronic devices. First, we briefly revisit the development history of ES and introduce its fundamental working principles. Then, various ES techniques are discussed in detail, including parameter control and equipment optimization. Next, we highlight the regulating mechanism based on ES at both the micro- and macro-scales. Finally, the application of electrospun NFs in key devices (such as photodetectors, synaptic devices, transistors, gas sensors, and triboelectric generators) is systematically summarized and analyzed as outlined in Fig. 1.

**He Shao**

*Dr He Shao is a Postdoctoral Research Fellow at the Department of Materials Science and Engineering, City University of Hong Kong. She obtained her BS degree from Jilin Normal University in 2016 and her PhD degree from Jilin University in 2021. Her research interests focus on phototransistors, memristors, and synaptic devices.*

**Johnny C. Ho**

*Johnny C. Ho is a Chair Professor at the Department of Materials Science and Engineering, City University of Hong Kong. He received his PhD in Materials Science and Engineering from the University of California, Berkeley, in 2009. After postdoctoral training at Lawrence Livermore National Laboratory in California, he joined the City University of Hong Kong in 2010. His research group focuses on exploring novel nanomaterials and nano-engineering techniques for various technological applications, including electronics, energy-harvesting, photonics, and sensors.*

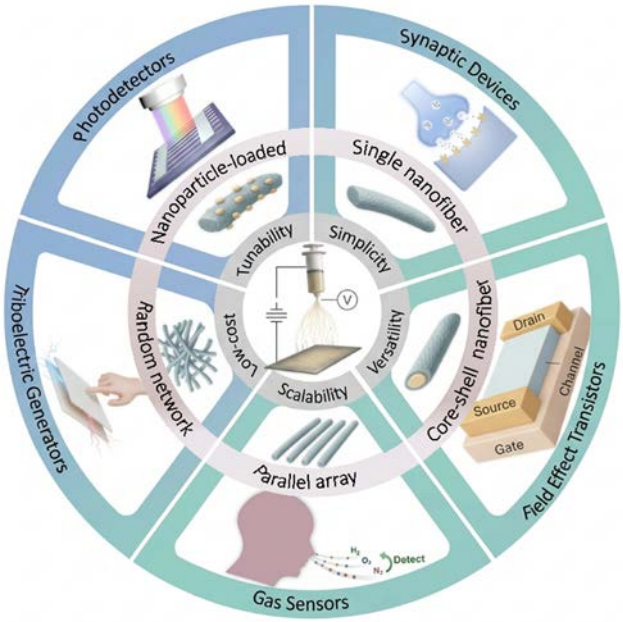


Fig. 1 Overview of intelligent (opto)electronics based on ES technology.

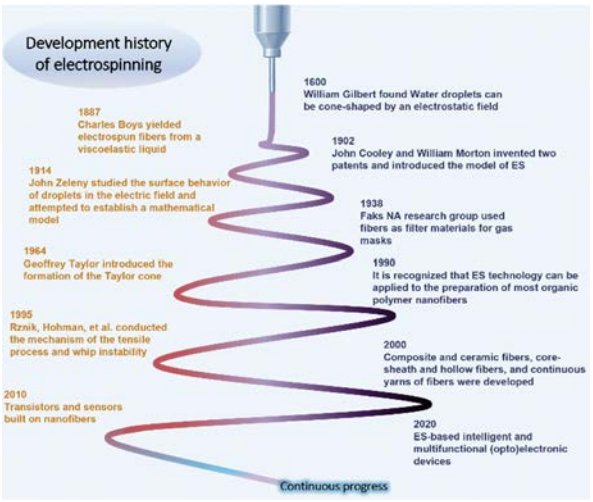


Fig. 2 The development route of ES technology.

## 2. Development of electrospinning technology

### 2.1. Fundamentals of electrospinning

The ES of nanoscale fibers is achieved by spinning and stretching polymer solutions or melts under electrostatic field.[38] It is a simple, practical technique widely used in the production of NFs. Historically, its origin can be traced back to the 17th century, during the era of Elizabeth I, when William Gilbert discovered that a charged piece of amber could deform a nearby water droplet into a cone and eventually cause it to eject smaller droplets.[39] This phenomenon laid the groundwork for the development of electrohydrodynamic theory. In 1887, Charles Boys observed that fibers could be drawn from a viscoelastic liquid under an electric field, marking a significant step toward the concept of ES.[40] In 1902, John Cooley and William Morton introduced the term ''electrospinning'' and filed two patents on the technique.[41] This was followed by John Zeleny's investigation into the surface behavior of droplets in electric fields and his attempt to establish a mathematical model in 1914.[42,43] ES saw its first practical application in 1938, when researchers used electrospun fibers as filter materials for gas masks. In 1964, Geoffrey Taylor introduced the concept of the Taylor cone and published a series of foundational studies, initiating the theoretical exploration of ES.[38,44,45]

Afterwards, the field experienced a period of stagnation until the early 1990s, when advances in electron microscopy enabled nanoscale characterization. Researchers demonstrated that a wide range of polymers could be electrospun into NFs, revitalizing interest in the technique and leading to the broader use of ES.[46–48] Since 1995, theoretical studies by Reznik, Hohman, and others have focused on stretching, whipping instability, and Taylor cone morphology, deepening understanding of fiber-forming mechanisms. As the theory evolved, the scope of ES expanded to produce composite and ceramic NFs, core–sheath and hollow fiber architectures, and continuous fiber yarns.[49–54] The ES technique gained intense attention in the early 21st century for fabricating inorganic NFs, including various polyoxides and chalcogenide-based materials. The development route of ES is shown in Fig. 2.[55–58]

Nowadays, ES is widely known as a technique for producing ultrafine fibers with nanoscale diameters.[59–63] As shown in Fig. 3a and b, the ES setup is generally classified into far-field ES and near-field ES.[64–66] The former operates with a nozzle-to-collector distance from several to tens of centimeters and is commonly used to fabricate random or non-woven NFs. In contrast, near-field ES can yield well-aligned and patterned fibers with high precision under a relatively low applied voltage.[67] Both techniques have been widely adopted for materials processing in emerging electronic and photonic devices.[21,68–71] Regardless of the mode used, the basic ES setup consists of three indispensable components: a high-voltage power supply, a syringe pump, and a collector.

ES works by ejecting charged polymer jets under the influence of an electric field. As shown in Fig. 3a, the polymer droplet at the needle tip is initially sagging due to gravity. Electrostatic forces overcome surface tension when a high voltage is applied between the needle and collector, causing the droplet to deform into a Taylor cone. Once the electrostatic repulsion reaches a critical point, a fine charged jet is ejected from the cone's apex.[72] Fig. 3b illustrates the near-field mode, in which the shorter distance enables localized fiber deposition. As time progresses, the ejected jet transitions from a straight, stable region into a region of bending instability, as shown in Fig. 3c. This well-known phenomenon of whipping instability is driven by electrostatic repulsion.[73] Fig. 3d depicts the force components responsible for this behavior: upward and downward forces from the outer segments of the jet ($F_{UO}$, $F_{DO}$) combine to produce a radial force ($F_R$), which deflects the jet and initiates spiraling motion. During this instability, the polymer jet is continuously stretched, its diameter gradually decreases, and

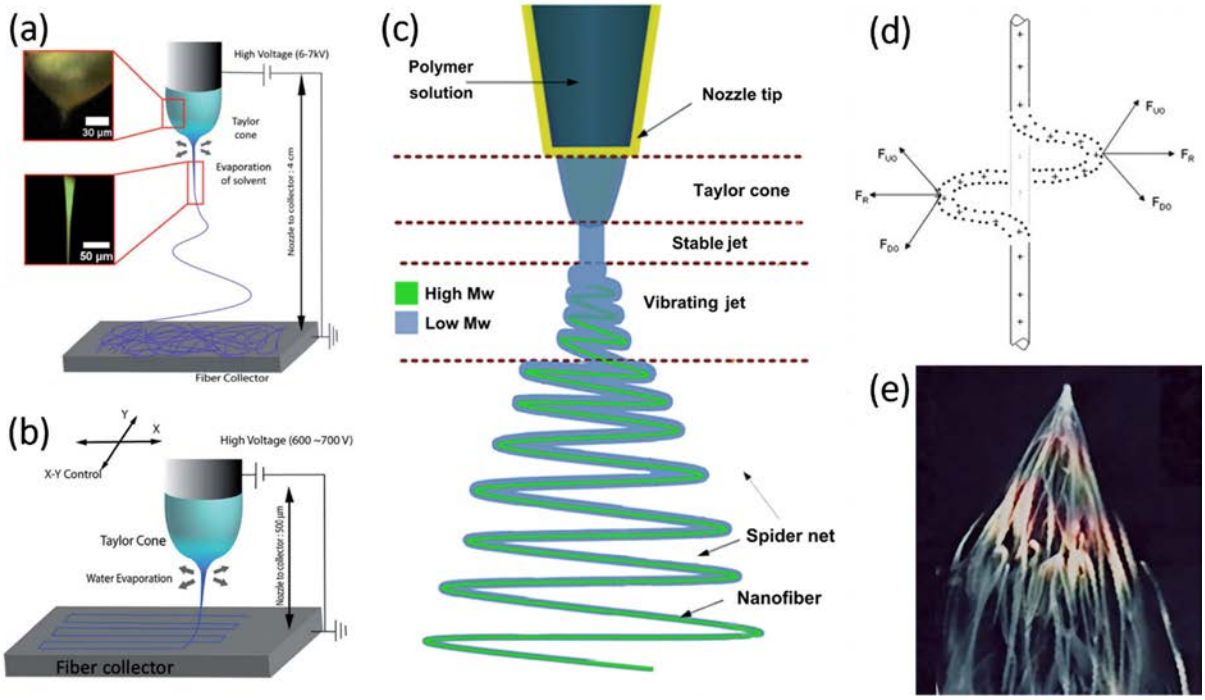


Fig. 3 Electrospinning configurations and jet dynamics. (a) Schematic illustration of the far-field ES and (b) near-field ES setups.[72] Reproduced with permission from ref. 72. Copyright 2019, this article is licensed under a Creative Commons Attribution-NonCommercial 3.0 Unported Licence. (c) Jet evolution from Taylor cone formation, jet ejection, to fiber whipping.[73] Reproduced with permission from ref. 73. Copyright 2012, Elsevier. (d) Schematic of electrostatic forces causing fiber bending instability. (e) High-speed optical image showing the conical envelope formed by rapid jet oscillation.[74] Reproduced with permission from ref. 74. Copyright 2008, Elsevier.

it undergoes rapid solidification through solvent evaporation.[74] Fig. 3e presents a high-speed optical image of the jet captured under illumination.[74] The colorful, cone-shaped envelope consisting of many branches is an optical illusion caused by the high-frequency oscillation of a single filament. This dynamic behavior promotes further thinning and uniform deposition of NFs onto the collector. The final form is deposited as solid NFs with diameters typically in the hundreds of nanometers, arranged in a random orientation.

To systematically illustrate the material design and functional diversity enabled by ES, Table 1 summarizes representative studies of ES NF-based optoelectronic and electronic devices, categorized by material type, polymeric matrix, solvent, working mechanism, and device application. A wide range of functional devices, from photodetectors, synaptic transistors, field-effect transistors (FETs), gas sensors, to self-powered generators, have been fabricated using both inorganic (*e.g.*, ZnO, InGaZnO, and $In_2O_3$) and organic (*e.g.*, P3HT (poly(3-hexylthiophene))) semiconductors. These materials are often dispersed in polymers like PVP (polyvinyl pyrrolidone), PVDF (polyvinylidene fluoride), or PEO (polyethylene oxide) to facilitate fiber formation and alignment.[31–33,35,36,75–77] Notably, diverse working mechanisms, such as heterojunction engineering, ionic migration, phase transition, and piezo-triboelectric coupling, have been leveraged to achieve tunable plasticity, enhanced photoresponses, and self-powered sensing. These mechanisms are intimately correlated with the structural and interfacial characteristics imparted by ES morphology.[18,78–80]

Depending on the target application, NFs should be precisely tuned in terms of morphology and diameter to meet specific device requirements. A clear understanding of the ES process and its physical mechanisms is crucial for achieving such control. A detailed discussion on parameter optimization will be provided in the following sections.

### 2.2. Methodology of the electrospinning process

ES technology offers excellent advantages in fabricating continuous NFs. However, the experiment will be affected by internal and external factors. NFs with different morphologies can be obtained by controlling various parameters and improving the device during the ES process.[101] The related regulation methods will be introduced in the following section.

**2.2.1. Precursor design and process parameters.** The formation of continuous and uniform electrospun NFs depends on the interplay between the intrinsic properties of the precursor solution and the external parameters applied during processing. The precursor solution provides the molecular foundation that determines whether a stable jet can be initiated and sustained. The selection of polymer type, molecular weight, and concentration directly affects the degree of chain entanglement in the solution. As illustrated in Fig. 4, representative polymers such as PAN (polyacrylonitrile), PVP, PVA (polyvinyl alcohol), PS (polystyrene), and PVDF show distinct molecular structures that influence solubility, viscosity, and dielectric response. Adequate chain entanglement is essential for ensuring cohesive jet

Table 1 Summary of optoelectronics and electronics based on ES

| Materials | Solvent | Polymer | Mechanism | Application | Ref. |
|---|---|---|---|---|---|
| $SnZnO_x$ | DMF | PVP | Heterojunction | Photodetector | 81 |
| $ZnSnO_3/In_2O_3$ | DMF | PAN | Heterojunction | Photodetector | 82 |
| Sr-$In_2O_3$ | DMF | PVP | Phase transition | Photodetector | 83 |
| Tri-cation perovskite | DMF/DMSO | PVP | Photomultiplication effect | Photodetector | 31 |
| Ag–ZnO | Ethanol/DI | PVP | P–N junction | Photodetector | 84 |
| InGdO | DMF | PVP | Oxygen vacancy | Synaptic device | 76 |
| ZnSnO | DMF | PVP | Synaptic plasticity | Synaptic device | 85 |
| ZnO | DMF | PVP | Tunable plasticity | Synaptic device | 35 |
| InSnMgO | DMF | PVP/PEO | Ionic migration | Synaptic device | 86 |
| PQT-12 | Chloroform/Chlorobenzene | PEO | Ionic migration | Synaptic device | 36 |
| InGdO | DMF | PVP | Oxidation-based | FET | 87 |
| InZnO | DMF | PVP | Element doping | FET | 88 |
| InZnHfO | DMF | PVP | Oxygen defects | FET | 89 |
| $SnO_2$ | DMF | PVP | Schottky barrier | FET | 90 |
| InGaZnO | DI water | PVA/CS | Aligned NF | FET | 91 |
| $SnO_2/SnS_2$ | DMF/Ethanol | PVP | Heterojunction | Gas sensor | 30 |
| $Au/SnO_2$ | Methanol | PVP | Plasmonic effect | Gas sensor | 92 |
| $MoS_2/SnO_2$ | DMF/ethanol | PVP | P-N heterojunction | Gas sensor | 93 |
| NaPt–$WO_3$ | DI | PVP | Synergistic effect | Gas sensor | 94 |
| DPA | DMF | PVDF | Piezotronics effect | Tactile sensor | 95 |
| PA11/ZnO | DMF/ethanol | PA11/polyester | Triboelectric effect | Triboelectric generators | 96 |
| PVDF-TrFE | DMF | PMMA | Electrostatic Polarization | Triboelectric generators | 97 |
| PVDF-HFP | DMF | PVDF-HFP | Microstructure-Triboelectrification | Triboelectric generators | 98 |
| PANI/ZnO | DMF | PVDF/PTFE | Piezo-tribo hybrid | Triboelectric generators | 99 |
| P3HT | Chloroform | P3HT | Acoustic carrier control | Triboelectric generators | 100 |

stretching. Excessively high concentrations increase viscosity and hinder the formation of a stable Taylor cone, whereas insufficient concentrations lead to fragmented jets and electrospraying.[102–104] These behaviors originate from the molecular level, where polymer coils overlap sufficiently to resist capillary breakup during elongation.

The choice of solvent further modulates solution behavior by influencing viscosity, surface tension, and dielectric constant. Solvents such as DMF (*N*,*N*-dimethylformamide), ethanol, water, THF (tetrahydrofuran), and acetone differ in volatility and solvation ability.[24,105–107] These properties determine the extent of polymer chain expansion and the rate of solvent removal once the jet is exposed to the electric field. A solvent with strong solvation capability promotes homogeneous dispersion, while high volatility supports rapid solidification. When polymer, solvent, and functional additives are combined, the precursor solution can exhibit a wide range of behaviors, especially if inorganic, carbon-based, or hybrid nanomaterials are introduced. The interactions between polymer chains and nanomaterials can alter the viscoelastic response of the solution, thereby influencing the uniformity of the fibers and their surface morphology. By incorporating semiconducting polymers, quantum dots, metal oxide or chalcogenide particles, and plasmonic components into the spinning solution, one can tailor light absorption, charge transport, and dielectric responses within the fibrous network.[108–111] Rational design of precursor systems, therefore, not only secures a stable ES process but also endows NFs with targeted functions required for electronic and optoelectronic devices.

In addition to intrinsic solution factors, external process parameters determine how the jet evolves after leaving the needle (Fig. 5). The applied voltage, solution flow rate, and the distance between the needle and the collector together determine the electric field distribution, the initiation of the Taylor cone, and the extent of jet stretching.[112–115] In practice, the applied voltage is typically adjusted between 10 and 25 kV, depending on the conductivity and surface tension of the precursor solution, as well as the setup geometry. A minimum threshold is required to overcome surface tension and generate a stable jet, while moderate electric fields promote continuous thinning of the charged filament and lead to uniform fibers.[116–118] When the voltage is set too high, the jet undergoes severe whipping and branching, leading to irregular morphologies and bead defects. The solution flow rate typically lies between 0.1 and 1.0 mL $h^{-1}$ and controls the volume of liquid delivered to the needle tip per unit time.[119] A too-low flow rate causes intermittent jetting and may break the continuity of the deposited fibers. In contrast, a too high rate leads to insufficient stretching and incomplete solvent evaporation, resulting in thick fibers or a bead-on-string structure. The needle-to-collector distance is usually set between 10 and 20 cm and influences both the field strength and the jet flight time.[120,121] A short distance increases the electric field but limits the jet's residence time, resulting in poor stretching and residual solvent. A long distance weakens the electric field and reduces deposition efficiency. These parameters act cooperatively rather than independently, so a high flow rate often needs to be compensated by a larger voltage or a longer distance to maintain a stable, well-stretched jet.[74,122,123]

Environmental conditions further modulate jet solidification and microstructure development.[124,125] Ambient temperature affects solvent viscosity and polymer chain mobility, while relative humidity controls the extent of vapor-induced phase separation, particularly in systems containing water or other hygroscopic solvents. At high humidity, condensed droplets and slow drying can result in porous or wrinkled fiber surfaces,

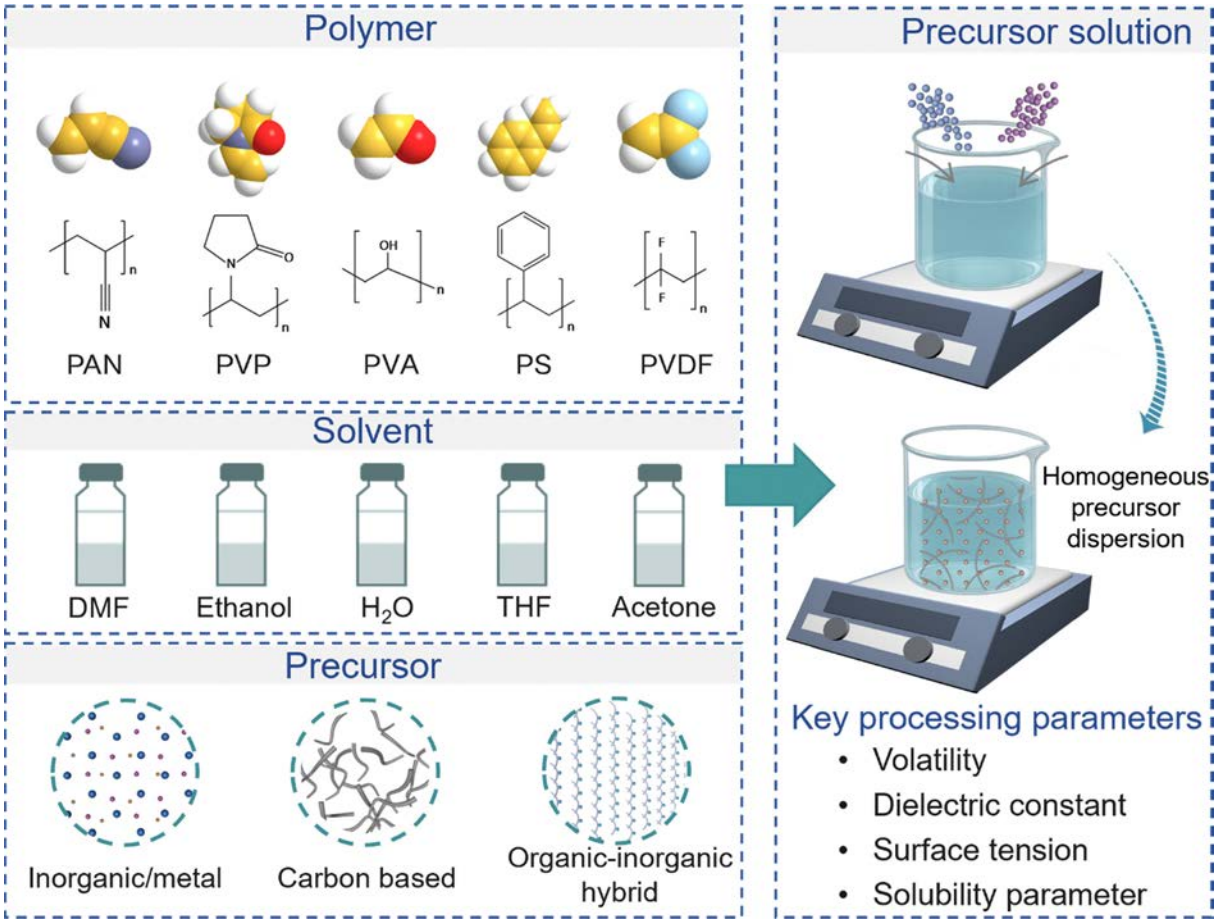


Fig. 4 Schematic illustration of the precursor design for ES.

whereas low humidity promotes rapid solvent evaporation, favoring smooth, dense fibers. The volatility and mixing ratio of solvents, such as DMF, ethanol, or water, determine both the jet's solidification rate during flight and the formation of internal features, including voids and skin-core structures. When semiconductor nanoparticles, quantum dots, or metal oxide precursors are present, the drying kinetics also influence their spatial distribution within the fiber cross-section. By coordinating applied voltage, flow rate, collector distance, and environmental conditions, it is possible to engineer NFs with controlled diameter, surface roughness, and porosity. These morphological features in turn govern light scattering, absorption length, and carrier transport pathways, which are crucial for optimizing the performance of electrospun NFs in electronic and other optoelectronic devices.

**2.2.2. Feeding configuration and receiving system.** The precursor formulation governs the intrinsic feasibility of fiber formation, while the feeding system configuration and collector design dictate the external organization of the NFs. Collectively, these elements determine the structural complexity, alignment, and spatial arrangement of the final fiber assembly. They regulate both the delivery, merging, and acceleration of the precursor solution under an electric field, as well as the guidance, stretching, and organization of the resulting jet during deposition.

As illustrated in Fig. 6a, a series of representative setups progressively increases in structural complexity, from single-needle spinning to advanced multi-channel and multimodal strategies. Single-needle ES remains the most widely used configuration due to its operational simplicity and stable jet formation.[86] A uniform NF jet is formed when a single precursor solution is extruded from the needle tip. Introducing a second syringe enables parallel spinning, in which two separate jets are ejected and deposited simultaneously. This configuration provides a convenient route for producing multicomponent fiber mats or blending different functionalities on the same substrate. When the two syringes are connected through a coaxial spinneret, the inner and outer solutions form a core–shell jet, resulting in fibers with a well-defined hierarchical internal structure.[78] The resulting NFs can incorporate a functional core, such as a semiconducting or photo-sensitive material, protected by a mechanically robust or dielectric outer sheath. In contrast, co-electrospinning involves multiple nozzles, enabling the simultaneous spinning of different jets.[126] This setup facilitates the fabrication of multi-component NF networks by interweaving fibers of different compositions. As a result, it provides an efficient pathway to construct spatially heterogeneous materials with complex architectures and synergistic functionalities.

 

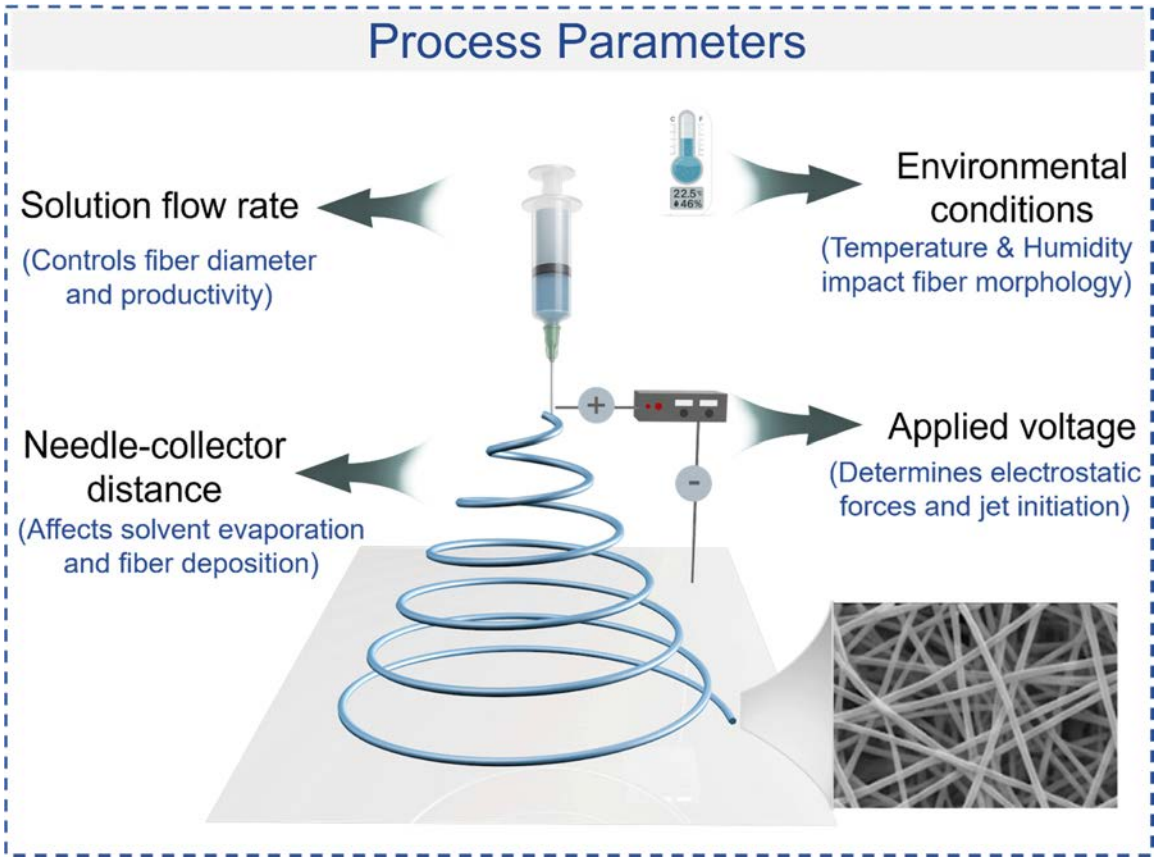


Fig. 5 Schematic illustration of key ES process parameters.

Fig. 6b highlights how collector design determines fiber alignment, packing density, and macroscopic arrangement. Deposition onto a stationary flat collector produces randomly oriented mats, suitable for filtration or sensing applications.[127] When the collector is a rotating cylindrical drum, the mechanical drawing force imposed by rotation aligns the jet along the tangential direction, producing oriented NF bundles once the rotation speed surpasses the alignment threshold.[79] Patterned collectors, such as substrates with trenches or insulating islands, guide fiber deposition along predefined pathways and enable ordered network formation.[75] In contrast, rotating disc collectors concentrate electric field lines toward the disc edge, allowing the jet to wrap and accumulate into continuous aligned coils.[128] These diverse collecting strategies regulate the interplay between electrostatic forces, mechanical stretching, and geometric confinement, allowing NFs to be organized from discrete strands into tailored architectures.

By appropriately selecting the feeding configuration and receiving system, the ES technique can serve as a versatile platform capable of fabricating large-scale nanofibers with controlled geometry, internal hierarchy, and macroscopic order.[129] The ability to tune these parameters is critical for designing NF systems for device applications, where fiber alignment, core–shell arrangement, and structural uniformity directly affect charge transport, optical coupling, and device stability.[23,38]

## 3. Property optimization of NFs

ES technology offers a straightforward, cost-effective, and efficient approach to fabricating NF-based (opto-)electronic materials. Its advantages lie in the precise control of the nanoscale and the ability to optimize photoelectric conversion efficiency, charge carrier transport, and interface stability through rational modulation of the material's microstructure, defect distribution, and interface engineering.[45,130–133] In this section, based on recent studies, we mainly discuss the modulation strategies for ES optoelectronic and electronic devices from three perspectives: grain size modulation, oxygen vacancy engineering, and heterostructure design.

### 3.1. Crystallinity and phase modulation

In ES materials, the crystallinity and phase structure are intrinsic to the material system and can be highly tuned through external processing conditions. Such modulation plays a pivotal role in governing carrier transport, optical absorption, and interfacial polarization.[25,80] Instead of merely enhancing crystallinity, recent studies have focused on guiding the crystallization pathway through mechanisms such as spatial confinement or electric-field-induced molecular alignment, aiming to achieve targeted functional states.[134]

Zhi *et al.* proposed a strategy for modulating both crystallinity and phase behavior in hybrid ES NFs by incorporating

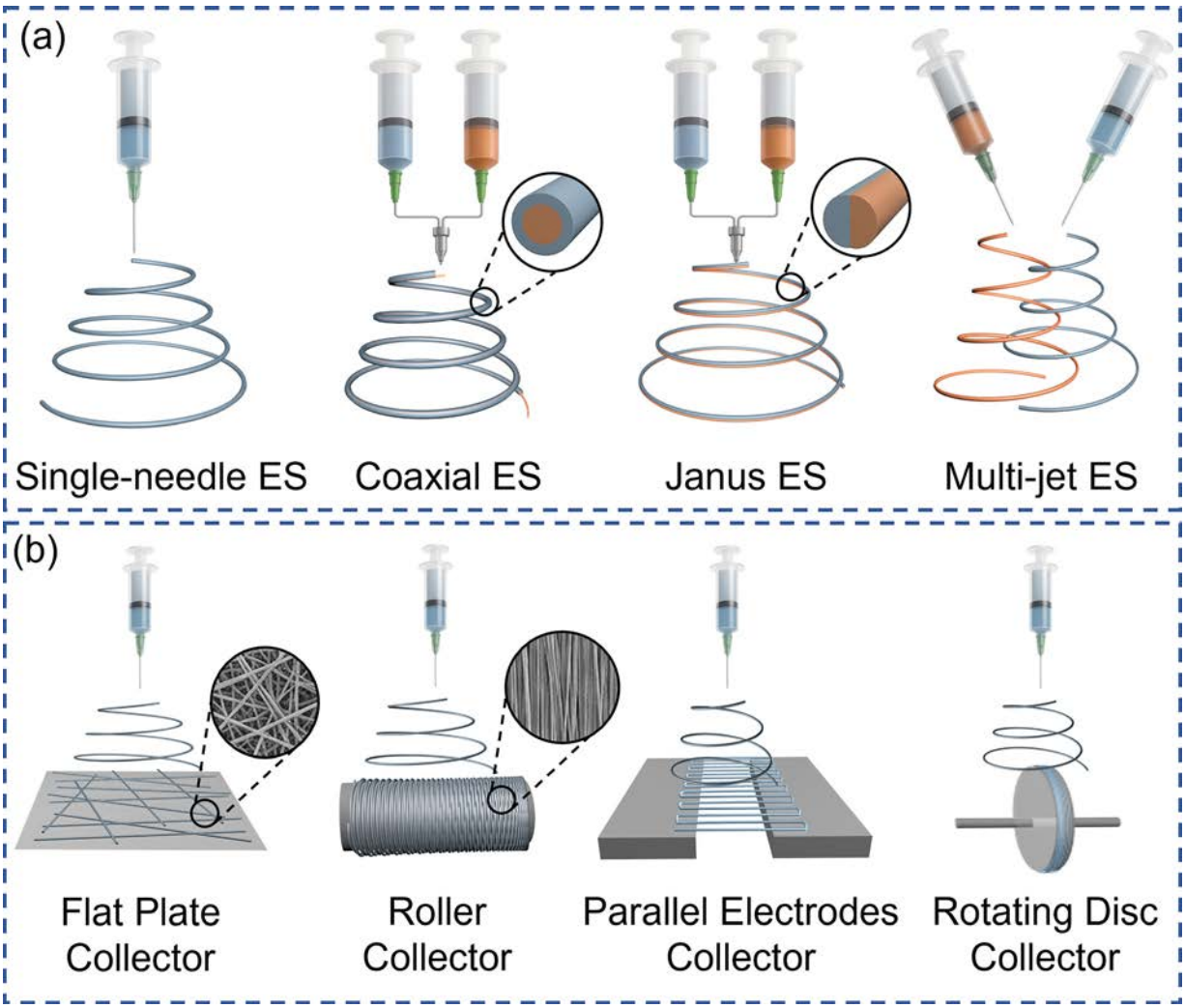


Fig. 6 Configurational design of electrospinning jets and collectors. (a) Schematic illustrations of different ES configurations, including single-needle, coaxial, Janus, and multi-jet setups. (b) Schematic illustrations of typical ES collector designs, such as flat plates, rotating drums, parallel electrodes, and rotating discs.

perovskite nanocrystals ($Cs_2InCl_5{\cdot}H_2O$) into a fluorinated polymer matrix. During ES, the applied high-voltage electric field stretches the polymer jet and exerts a directional force on the embedded nanocrystals. This alignment is synergistically enhanced by interfacial hydrogen bonding between the nanocrystals and the polymer chains, which induces anisotropic interfacial strain and local dipolar fields (Fig. 7a). Such coupled field–interface interactions initiate a non-equilibrium phase transition, wherein the system transforms from a disordered, amorphous-like network into a uniaxially aligned polar crystalline phase (Fig. 7b).[80] Unlike conventional thermally driven grain growth, this transformation is governed by a symmetry-breaking mechanism. Under the influence of the electric field, polarizable polymer segments align, and the intrinsically low-symmetry nanocrystals with soft lattice modes undergo directional reorganization. Importantly, this field-induced ordering enhances crystallinity and modulates the crystal phase, thereby inducing a symmetry switch and a reversal of polar orientation. The resulting aligned dipolar structure strengthens interfacial polarization and facilitates efficient charge redistribution, ultimately boosting piezoelectric and triboelectric performance. This demonstrates how ES, beyond morphological shaping, can serve as a powerful platform for *in situ* phase engineering, offering new pathways for the functional design of hybrid optoelectronic materials.

In contrast to the field-driven phase transition, Chen *et al.* employed a geometry-guided crystallinity modulation strategy, leveraging the control of ES needle diameter to tune the grain size of ITO (indium tin oxide) NFs. As the fiber diameter decreased, a corresponding grain size reduction was observed, leading to quantum confinement-induced bandgap widening (Fig. 7c).[25] As the fiber diameter decreased, the grain size decreased accordingly, widening the bandgap due to quantum confinement. Smaller grains suppressed unwanted free carrier generation and enhanced gate modulation, as evidenced by a significantly improved on/off ratio in field-effect transistors.

 

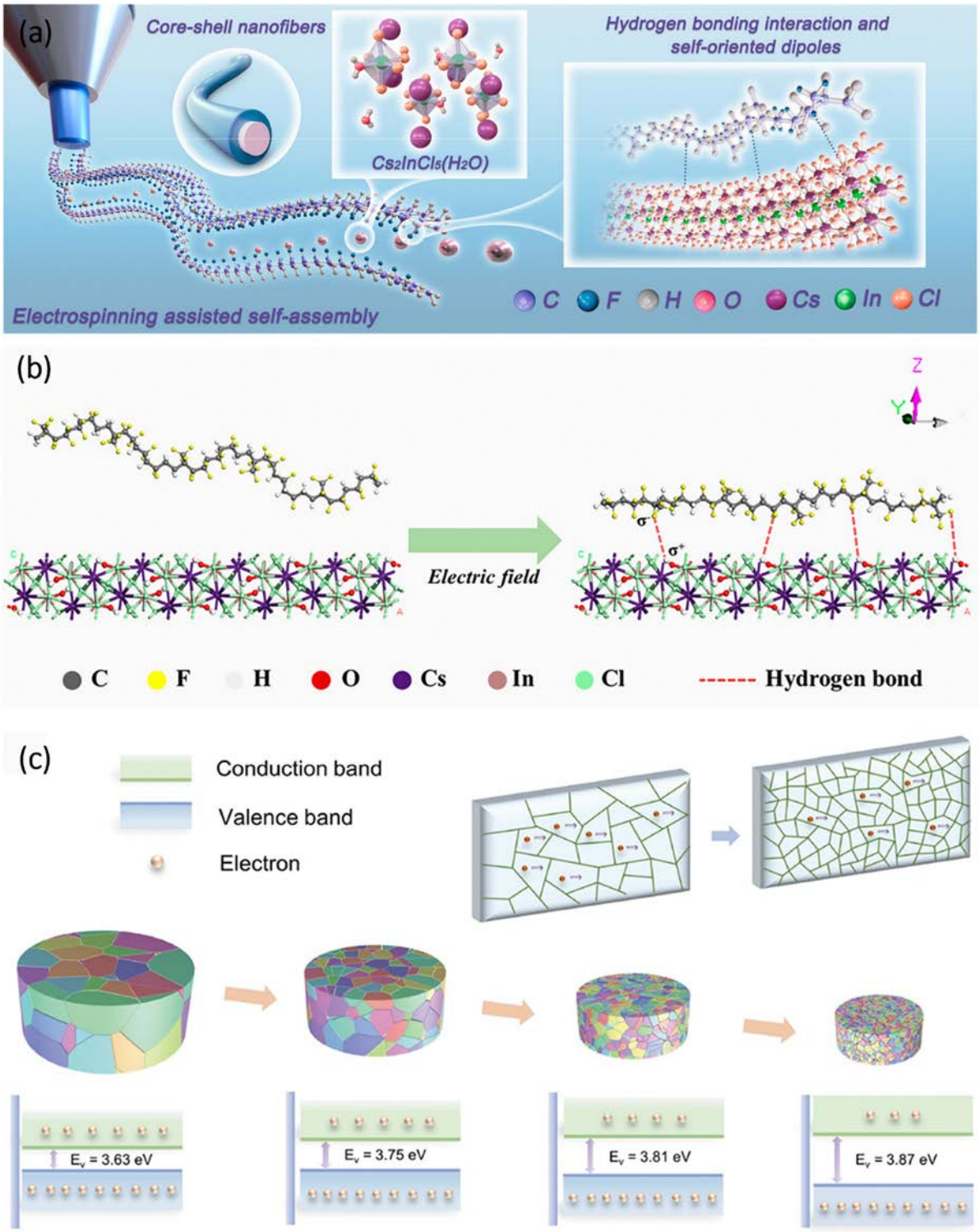


Fig. 7 Microstructural ordering and grain-size dependent electronic modulation. (a) Schematic mutual interaction and (b) proposed interaction mechanism between $Cs_2InCl_5(H_2O)$ and PVDF-HFP (hexafluoropropylene)chain.[80] Reproduced with permission from ref. 80. Copyright 2024, American Chemical Society. (c) The bandgap variation corresponding to various grain sizes of ITO NFs.[25] Reproduced with permission from ref. 25. Copyright 2023, Springer Nature.

However, the increase in grain boundaries also introduced potential carrier-scattering centers, highlighting a trade-off between mobility and confinement.

These two approaches, namely field-induced phase ordering and geometry-driven grain modulation, represent distinct yet complementary facets of crystallinity engineering in ES

systems. The first emphasizes the control of internal symmetry and molecular orientation to stabilize specific phases during fiber formation. The second relies on tuning grain size and boundary density to modulate the material's energy landscape and charge transport behavior. Together, these strategies underscore a broader principle: crystal evolution in ES materials is not solely determined by post-processing. Still, it is fundamentally shaped by the dynamic conditions inherent to the ES process itself.

### 3.2. Defect and doping engineering

Defect and doping engineering represent a widely applicable strategy to modulate the electronic properties of ES nanomaterials across diverse material systems. Whether in inorganic oxides, hybrid composites, or polymer-based semiconductors, manipulating vacancy concentrations and chemical dopants provides a robust handle for tuning carrier transport, interfacial energetics, and functional stability.[135,136]

A representative example is provided by Cong *et al.*, which systematically modulated the oxygen vacancy ($V_O$) concentration in InZnO NFs by altering the cationic ratio (Fig. 8a).[135] Their study revealed that increasing the Zn content reduces the $V_O$ concentration, lowering the free-carrier density and power consumption, as shown in Fig. 8b. Conversely, excessive In content results in a higher $V_O$ concentration, which may compromise the device's stability (Fig. 8c). In addition, the inset diagram of Fig. 8b schematically illustrates the microscopic origin of this phenomenon: the introduction of $Zn^{2+}$ ions promotes the formation of a cubic-to-rhombohedral phase transition in the $In_2O_3$ matrix. Compared to the cubic phase, the rhombohedral phase exhibits better packing of anion layers and enhanced electron mobility due to reduced porosity and an ordered lattice structure. However, the excessive presence of the rhombohedral phase may lead to higher conductivity and EPSC (excitatory postsynaptic current), ultimately increasing energy consumption. Therefore, a

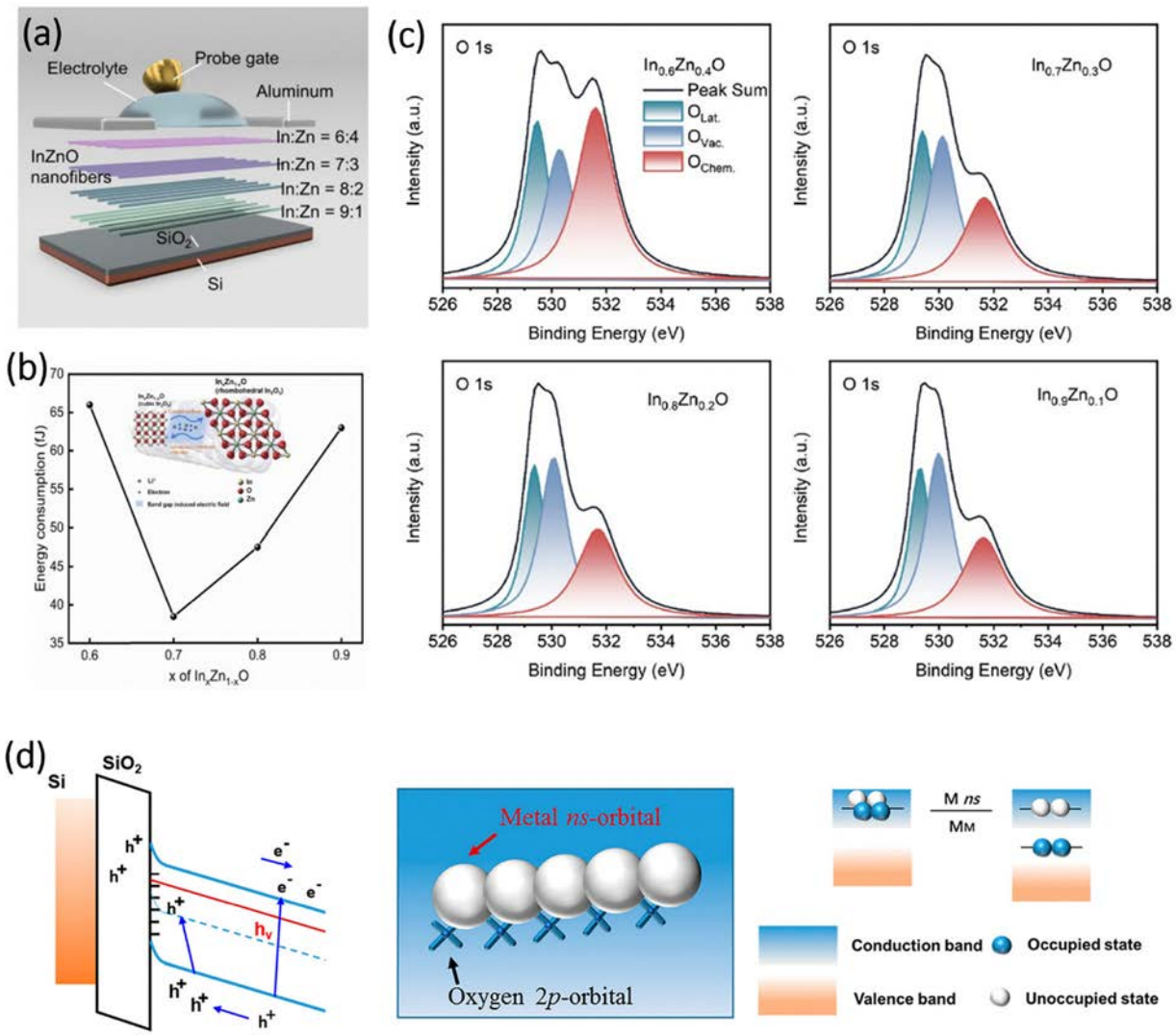


Fig. 8 Compositional defect control and orbital-level pathways. (a) Device structure, (b) energy consumption, and (c) chemical states of InZnO NF device with different In : Zn ratios.[135] Reproduced with permission from ref. 135. Copyright 2023, Springer Nature. (d) Energy band structure, orbital structure, and charge transport pathways of InZnO NFs.[137] Reproduced with permission from ref. 137. Copyright 2021, John Wiley and Sons.

moderate Zn content (*e.g.*, $In_{0.7}Zn_{0.3}O$) strikes a balance between minimizing $V_O$ and preventing phase-induced conductivity escalation, thereby achieving optimal device performance. This finding underscores a broader mechanism relevant not only to metal oxides but also to conjugated polymers or hybrid systems, where labile functional groups or dynamic moieties play analogous roles in defining trap states and local polarization.

Beyond oxygen vacancies, other defect types have also been widely exploited to regulate carrier dynamics and trap distributions in electrospun semiconductors. For instance, cation vacancies (*e.g.*, metal deficiencies in oxide lattices) can act as deep acceptor-like states, effectively suppressing excess free carriers and improving threshold voltage stability, which is particularly beneficial for low-power transistor operation.[138] In parallel, anion vacancies other than oxygen, such as sulfur, or selenium vacancies commonly encountered in chalcogenides and layered semiconductors, introduce localized states near the band edges that strongly influence photocarrier lifetime, recombination kinetics, and interfacial polarization. These non-oxygen vacancies often serve as controllable trap centers or charge donors/acceptors, enabling defect-mediated tuning of conductivity, responsivity, and memory behaviors. Such mechanisms have been widely reported in sulfides, selenides, and hybrid nanocomposites, underscoring that vacancy engineering is not limited to oxygen chemistry but is a general strategy across a broader class of ES-derived materials.

Further extending this concept, He *et al.* employed Al doping in InZnO fibers to introduce shallow donor levels while simultaneously improving morphological uniformity. As shown in the schematic band model (Fig. 8d), $Al^{3+}$ ions serve as electron donors and participate in orbital hybridization with oxygen atoms, effectively modulating the density of states near the conduction band minimum.[137] The resulting improvement in switching behavior and thermal stability highlights the potential of orbital-level doping design, which is equally relevant in π-conjugated organic frameworks or halide perovskite-based hybrids, where similar orbital interactions govern optoelectronic behavior.

Taken together, these studies highlight two complementary approaches: vacancy modulation to govern trap-assisted transport and memory behavior, and dopant engineering to reshape the electronic structure and stabilize functional performance. Both strategies offer generalizable principles applicable to a broad spectrum of ES materials, including oxide, organic, and hybrid systems, where defect states, interface chemistry, and local orbital alignment collectively determine device functionality.

### 3.3. Hybrid architectures for interface control

Beyond crystallinity and defect modulation, hybrid architectures engineering offers a powerful route to manipulate interfacial electronic properties in ES systems. Whether in inorganic semiconductors or at organic–inorganic interfaces, the critical behaviors of charge separation, transport, and retention, being essential for high-performance optoelectronics, can be effectively modulated by tailoring interactions across material boundaries.[18,96]

In the context of inorganic heterojunctions, He *et al.* introduced a coaxial $In_2O_3$@ZnO NF FET, in which a built-in radial band offset at the core–shell interface facilitates efficient separation of photogenerated carriers (Fig. 9a). Upon ultraviolet illumination, ionization of $V_O$ in ZnO releases free electrons, which accumulate at the $In_2O_3$ side due to the favorable conduction band alignment. This process forms a quasi-two-dimensional electron gas (2DEG) at the interface, drastically boosting electron mobility and reducing recombination losses. As shown in Fig. 9b, the resulting device achieves a remarkable carrier mobility of 202.3 $cm^2\ V^{-1}\ s^{-1}$ and excellent switching characteristics. Furthermore, the persistent photoconductivity observed after UV exposure (Fig. 9c) underscores the role of interface-trapped charges in sustaining high conductivity. This persistent photoresponse represents a photosynaptic behavior that aligns well with neuromorphic applications.[18]

Moving beyond inorganic semiconductors, Liang *et al.* demonstrated an alternative strategy using polyamide (PA) and polyester to construct an asymmetric, double-layered NF photodetector (Fig. 9d).[96] Here, the functional heterointerface arises not from semiconductor band offsets but from differential surface energies, work-function alignment, and dipole polarization between the two polymeric layers. The upper PA layer, with higher light absorption and polar groups, enhances surface potential variation under illumination. Meanwhile, the underlying polyester layer acts as an insulating buffer, reducing leakage current and stabilizing carrier transport pathways. This hybrid dielectric/semiconducting configuration improves photosensitivity and polarization-dependent responses, especially under low-intensity light. The device exhibits tunable photodetection behavior with angle- and direction-sensitive responsivity, enabling intelligent sensing functions that surpass those of traditional oxide-based photodetectors.

These two systems exemplify complementary paradigms of interface control. While the $In_2O_3$@ZnO heterojunction relies on band-engineered electron accumulation and vacancy modulation, the PA/polyester device leverages organic polarity and layer-specific functions to guide exciton dissociation and interfacial charge storage. Together, they illustrate that rational interface design, enabled by either lattice-matched semiconductor pairing or synergistic hybrid layering, can reconfigure local electric fields, modulate charge transfer kinetics, and thus enhance overall device functionality.[139–141]

## 4. Optoelectronics based on electrospinning

### 4.1. Photodetectors

Optical signals serve as indispensable carriers for information transmission in modern communication and sensing systems. As the core components, photodetectors are responsible for converting optical stimuli into electrical signals, enabling subsequent information processing, storage, and computation.[142,143] To meet the demands of diverse application scenarios, such as wearable electronics, optical imaging, and intelligent sensing, photodetectors

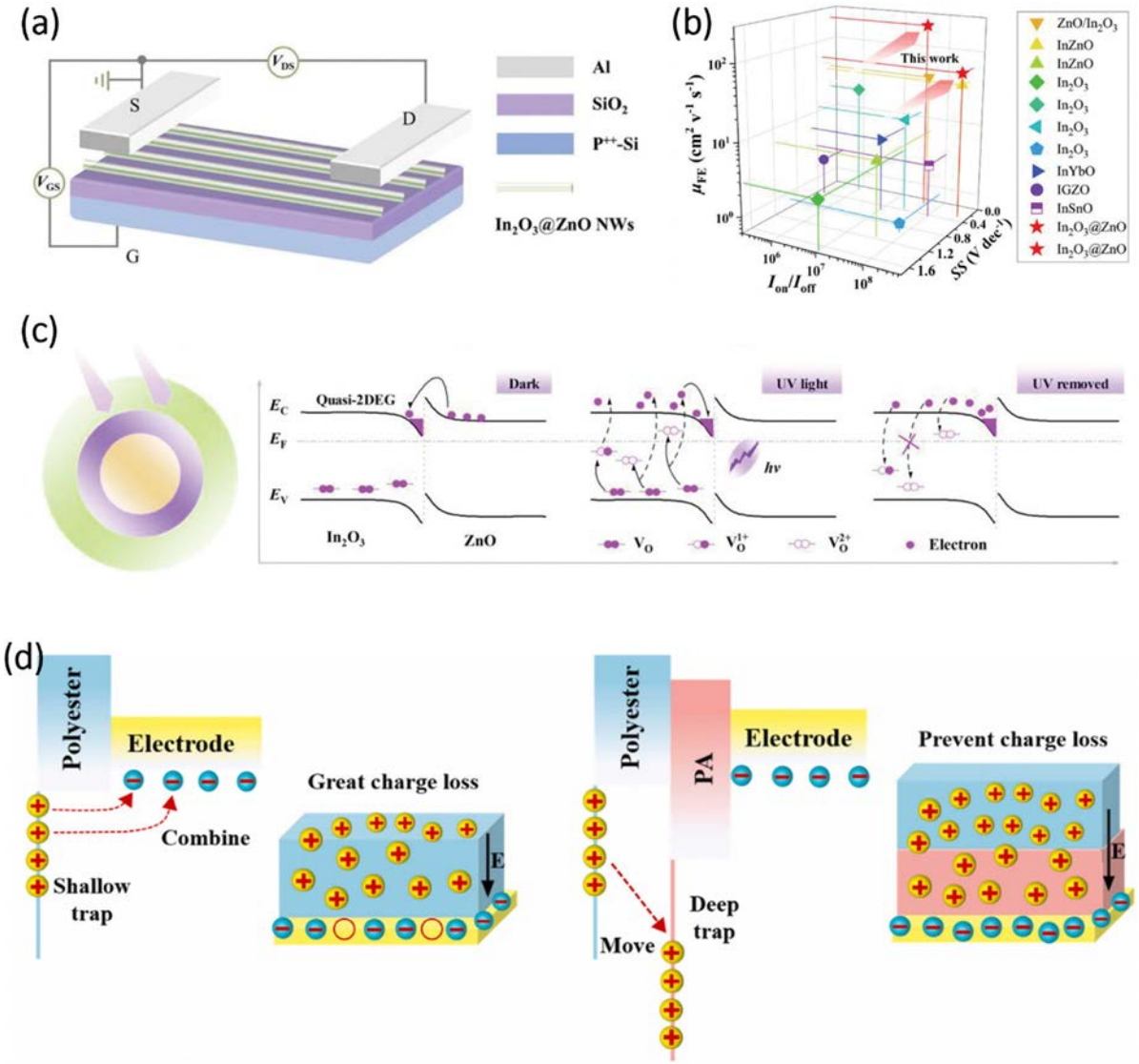


Fig. 9 Electronic structure mediated optimization of charge transport pathways. (a) Schematic diagram, (b) electrical performance comparison, and (c) energy band structure of the heterogeneous $In_2O_3$@ZnO NF device.[18] Reproduced with permission from ref. 18. Copyright 2024, John Wiley and Sons. (d) Charge transfer/trapping mechanism of the double-layered NF photodetector without and with the PA intermediate layer.[96] Reproduced with permission from ref. 96. Copyright 2022, Elsevier.

are expected to exhibit high responsivity, fast response speed, flexibility, optical transparency, and low energy consumption.[32,33,82] ES NFs, with their high specific surface area, abundant material selectivity, and solution-based processability, have emerged as promising channel materials in photodetectors. These unique advantages render ES NFs well-suited for the development of next-generation flexible and multifunctional optoelectronic devices.[77,81,83,136,142–144]

**4.1.1. Tunable photodetection.** Tunable photodetection is a key capability in optoelectronic systems that requires selective and adaptive photoresponses to external stimuli, such as wavelength, polarization, and illumination intensity.[32,77,136] Unlike traditional narrowband photodetectors with fixed response windows, tunable devices enable dynamic modulation of the sensing characteristics, thereby fulfilling diverse demands in intelligent perception, encrypted communication, and bio-integrated diagnostics. In ES-based architectures, the tunability arises not only from the intrinsic optoelectronic properties of the active materials but also from the anisotropic morphology, surface functionality, and hierarchical assembly of the NF networks.

One representative approach to wavelength-tunable detection was reported by He *et al.*, which integrated combustion synthesis and ES to construct InZnO NF photodetectors (Fig. 10a). The incorporation of indium into ZnO modulated the band structure by introducing shallow donor levels, while the ES 1D morphology (Fig. 10b) enhanced surface carrier collection and anisotropic charge transport. More importantly, the resulting device exhibited spectral-selective photoresponses in the UV region, and its photocurrent showed a distinct dependence on the excitation wavelength from 280 to 330 nm, as shown in Fig. 10c.[136] More

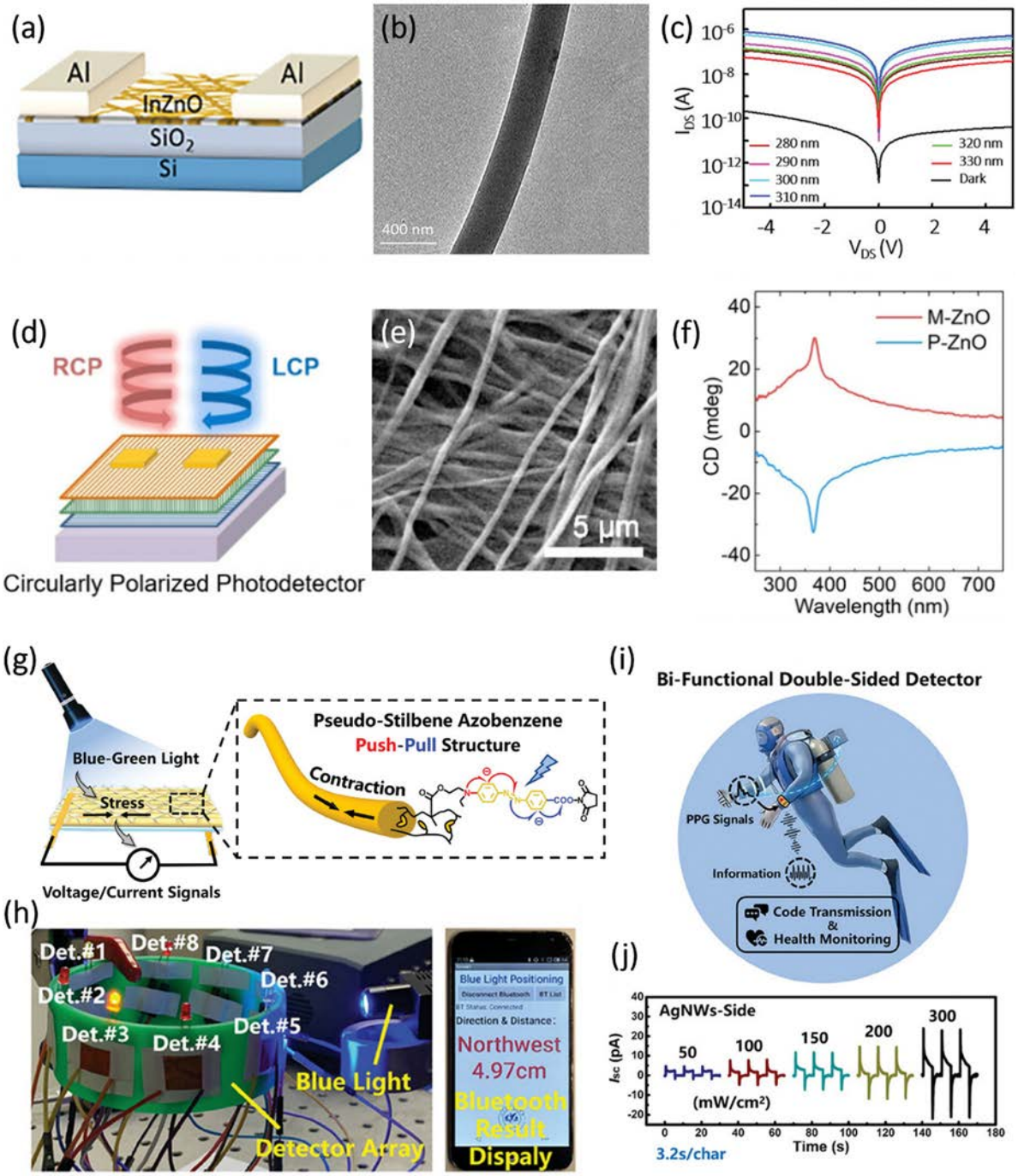


Fig. 10 Tunable and multimodal photodetection based on electrospun NFs. (a) Schematic diagram, (b) TEM image, and (c) wavelength-dependent UV photoresponse of InZnO NFs.[136] Reproduced with permission from ref. 136. Copyright 2021, John Wiley and Sons. (d) Schematic diagram, (e) SEM image, and (f) circular dichroism spectra of left/right-handed aligned ZnO NFs within stacked films.[77] Reproduced with permission from ref. 77. Copyright 2025, American Chemical Society. (g) Mechanism of photo-induced stress generation in azobenzene-containing polymer NFs. (h) Light positioning, (i) flexible device laminated on human skin, and (j) signal outputs under varying light intensities.[32] Reproduced with permission from ref. 32. Copyright 2025, John Wiley and Sons.

importantly, this behavior reflects how defect states and crystallinity jointly govern wavelength sensitivity in electrospun metal oxides, suggesting that post-treatment strategy can be as critical as compositional doping for spectral engineering. This wavelength sensitivity originated from the interplay between defect-assisted absorption and NF crystallinity, both of which were tunable *via* low-temperature annealing and deep-UV activation. The work demonstrates how compositional engineering and nanostructure control synergize to achieve spectral tunability, particularly in wide-bandgap metal oxide systems.

Moving beyond the spectral domain, Zhou *et al.* introduced chiral Moiré stacking of ES ZnO NFs to realize circular

polarization-resolved photodetection (Fig. 10d). Left and right-handed helical arrangements were formed by rotating the alignment direction of stacked fiber layers, enabling structural chirality in an otherwise achiral material. The SEM (scanning electron microscopy) image in Fig. 10e confirms the parallel alignment and uniform stacking of ZnO NFs, forming multi-layered chiral films. These superstructures exhibited significant circular dichroism (CD), attributed to interlayer optical coupling and anisotropic scattering, and enabled the device to discriminate directly between left and right-handed circularly polarized light. As shown in Fig. 10f, CD spectra displays distinct signals between M and P-type stacking, with peak values reaching ~30 mdeg. Rather than being merely a structural feature, this chiral arrangement establishes a new degree of freedom for manipulating light–matter interaction in fibrous systems, demonstrating that electrospinning can translate nanoscale ordering into macroscopic optical functionality. The emergence of handedness-selective photocurrent in such systems highlights how ES facilitates the generation of macroscopic chiroptical effects through ordered mesoscopic alignment, offering an elegant route to circularly polarized light (CPL) photodetectors without relying on external polarizers or birefringent components.[77]

In another direction, Liu *et al.* designed a double-sided photodetector composed of azobenzene-based liquid crystalline polymers blended with piezoelectric PVDF-TrFE and ES, incorporated into oriented NF fabrics. Here, the photoisomerization of the azobenzene mesogens under blue-green light induced internal mechanical stress, which is coupled with the piezoelectric matrix to generate a measurable electrical signal, as shown in Fig. 10g. The responsivity of this system was not only intensity-tunable over a wide range of illumination but also resilient to mechanical deformation, enabling real-time light positioning and physiological monitoring. As shown in Fig. 10h, the real-world application is a wearable array system that performs both light positioning and bluetooth signal transmission. Fig. 10i shows the device laminated to human skin, where a stable signal output is maintained during bending, stretching, and motion, demonstrating its resilience to deformation. Finally, Fig. 10j shows the voltage output as a function of illumination intensity, confirming the device's linear, tunable response under various blue light intensities.[32] This coupling between molecular photoisomerization and electromechanical transduction provides an alternative pathway for light sensing, which bypasses conventional semiconductor photophysics and expands the functional landscape of fiber-based photodetectors. The photodetection mechanism differed fundamentally from conventional semiconductor photogeneration: it relied on light-driven dipolar stress and electromechanical conversion. This work illustrates how ES enables the integration of functional polymers into stretchable, all-fiber devices with intrinsic intensity tunability and application-oriented adaptability.

Taken together, these examples demonstrate that tunable photodetection in ES systems can be achieved through multiple pathways: band-structure engineering (*e.g.*, In-doped ZnO), structural symmetry breaking (*e.g.*, chiral stacking), and hybrid stimulus-response coupling (*e.g.*, azobenzene–piezoelectric composite). ES not only provides a scalable platform for constructing such complex architectures but also introduces unique morphological features (*e.g.*, anisotropy, porosity, and orientation) that directly influence light absorption, carrier transport, and mechanical transduction. These insights open new opportunities for developing multifunctional optoelectronic devices where the photodetection window is not fixed but dynamically programmable by design. However, future studies should also address the trade-off between tunability and long-term stability, which remains insufficiently explored in current ES-based systems.

**4.1.2. Self-driven photodetectors.** To meet the growing demand for low-power, wearable optoelectronics, self-powered photodetectors have attracted significant interest due to their energy-autonomous operation and design flexibility. ES, enabling the fabrication of continuous 1D NFs with tunable surface and interface properties, provides a robust platform for constructing such devices.[82,84]

Notably, coaxial architecture and intrinsic piezoelectricity in certain ES materials offer unique opportunities for realizing high-performance self-driven UV photodetectors. A representative example is the $ZnSnO_3$@$In_2O_3$ core–shell NF-based photodetector, fabricated *via* coaxial ES followed by calcination at 650 °C, as shown in Fig. 11a. Furthermore, the SEM image of the sample with a distinct core-shell morphology after annealing is shown in Fig. 11b. The resulting heterojunction exhibits a coaxial n–n interface with an enhanced internal electric field and spontaneous polarization. Upon UV illumination, efficient charge separation occurs at the $ZnSnO_3$/$In_2O_3$ interface, resulting in a significant photocurrent even under zero bias (Fig. 11c). Importantly, the built-in potential and strain-induced piezoelectric modulation jointly modulate the Schottky barrier height, enabling dynamic tuning of the photocurrent. Under a compressive strain of less than 3.1%, the responsivity increases to 1.01 mA $W^{-1}$. This strain-dependent modulation highlights how mechanical degrees of freedom can be harnessed as an active tuning knob, rather than being treated merely as an environmental disturbance. Energy-band alignment analysis further supports piezo-phototronic regulation, revealing strain-sensitive barrier modulation within the non-centrosymmetric core–shell system.

Mechanical stability is a critical parameter for flexible electronics. The $ZnSnO_3$@$In_2O_3$ photodetector maintains its responsivity over 1000 bending cycles, demonstrating outstanding robustness (Fig. 11d). This combination of structural design, intrinsic piezoelectricity, and robust mechanical endurance affirms the potential of ES core–shell fibers in wearable UV sensing systems.[82]

Another elegant strategy utilizes crossed arrays of pure and Ag-doped ZnO NFs to construct homojunction-based self-powered photodetectors (Fig. 11e). Through a simple $Ag^+$ doping route during ES, p-type ZnO NFs are achieved with embedded Ag nanoparticles, as shown in the TEM image in Fig. 11f. These contribute to carrier modulation through localized Schottky barriers and enhance light absorption *via* plasmonic effects.

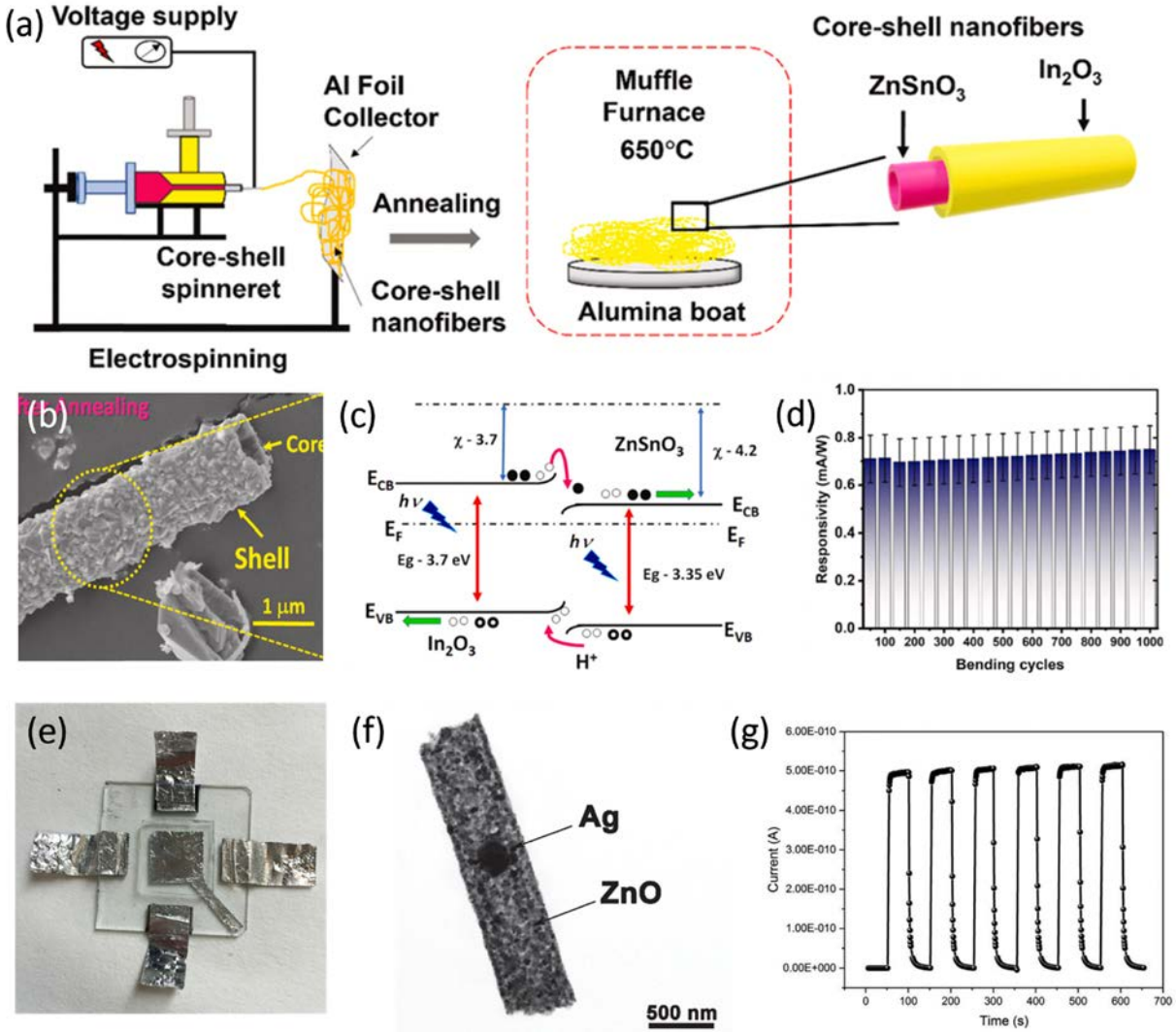


Fig. 11 Self-powered photodetection based on heterojunction NFs. (a) Fabrication process, (b) SEM image, (c) piezo-phototronic modulation mechanism, and (d) mechanical durability test of $ZnSnO_3$@$In_2O_3$ core–shell heterojunction NFs.[82] Reproduced with permission from ref. 82. Copyright 2022, Elsevier. (e) Device layout, (f) TEM image, and (g) time-resolved zero-bias photoresponse of Ag-doped ZnO NFs.[84] Reproduced with permission from ref. 84. Copyright 2018, John Wiley and Sons.

The perpendicular configuration of p–n NF arrays enables photovoltaic-type operation without an external bias, exhibiting an ultrahigh on/off ratio of $2.5 \times 10^4$ and short rise/decay times (Fig. 11g). These improvements arise from the cooperative effects of junction fields and plasmonic enhancement, illustrating that multi-physical coupling is often more effective than single-parameter optimization. Compared to conventional ZnO photodetectors, the combined effects of internal junction fields and plasmonic enhancement significantly improve both sensitivity and response speed.[84,145]

Collectively, these two representative strategies exemplify how rational NF design can successfully realize self-powered photodetection, whether through coaxial heterojunctions or homojunctions integrated with internal field modulation. However, the development of self-driven photodetectors based on ES is far from reaching its full potential. A key challenge lies in transforming stochastic nanofiber networks into predictable energy landscapes for charge transport, which requires tighter coupling between bottom-up fabrication and device modeling. Rather than viewing these systems merely as a structural novelty, a more profound scientific shift is required: from engineering discrete material interfaces to constructing dynamic, field-tunable nanointerfaces that adapt to external stimuli, such as light intensity, mechanical strain, and temperature fluctuations. Current ES systems primarily rely on built-in electric fields, piezoelectric effects, or Schottky barriers to drive charge separation. While effective, such mechanisms are typically static and unidirectional, limiting their adaptability and spectral versatility. Moreover, due to the random orientation, porosity, and stochastic junction formation inherent in traditional ES, precise control over interface uniformity, carrier transport pathways, and device reproducibility remains challenging. These issues underscore a key limitation: although ES offers morphological freedom, its integration into deterministic

device architectures still lacks the rigor of top-down microfabrication. Meanwhile, their future impact lies in transitioning from passive detection to adaptive, intelligent, and multifunctional photonic systems. With its unique capacity to merge materials chemistry, structural mechanics, and device physics, ES is well positioned to serve as a foundational platform for this transformation, whose stochastic nature can be harnessed to achieve programmable functionality.

**4.1.3. Broadband photodetectors.** Broadband photodetection lies at the heart of next-generation imaging, communication, and environmental monitoring systems, where seamless responsivity from UV to NIR enables richer signal acquisition and spectral discrimination.[31,33] Yet the pursuit of broadband performance is not merely a spectral expansion but a functional redefinition. The real challenge lies not in covering more wavelengths, but in orchestrating charge dynamics across vastly different photon energies, carrier mobilities, and interfacial environments. ES, with its ability to weave materials into highly tunable, low-dimensional networks, offers an unusual degree of freedom for addressing this challenge at both structural and electronic levels.

Another compelling illustration is that Kim *et al.* constructed an NF-based photodetector using tri-cation perovskite fibers (Fig. 12a). Unlike planar films, where carrier transport is largely diffusion-limited, the fibrous architecture here introduces a high density of shallow traps at the perovskite/HTM (hole transproting materials) interface. As illustrated in Fig. 12b, trapped electrons enable photogenerated holes to be

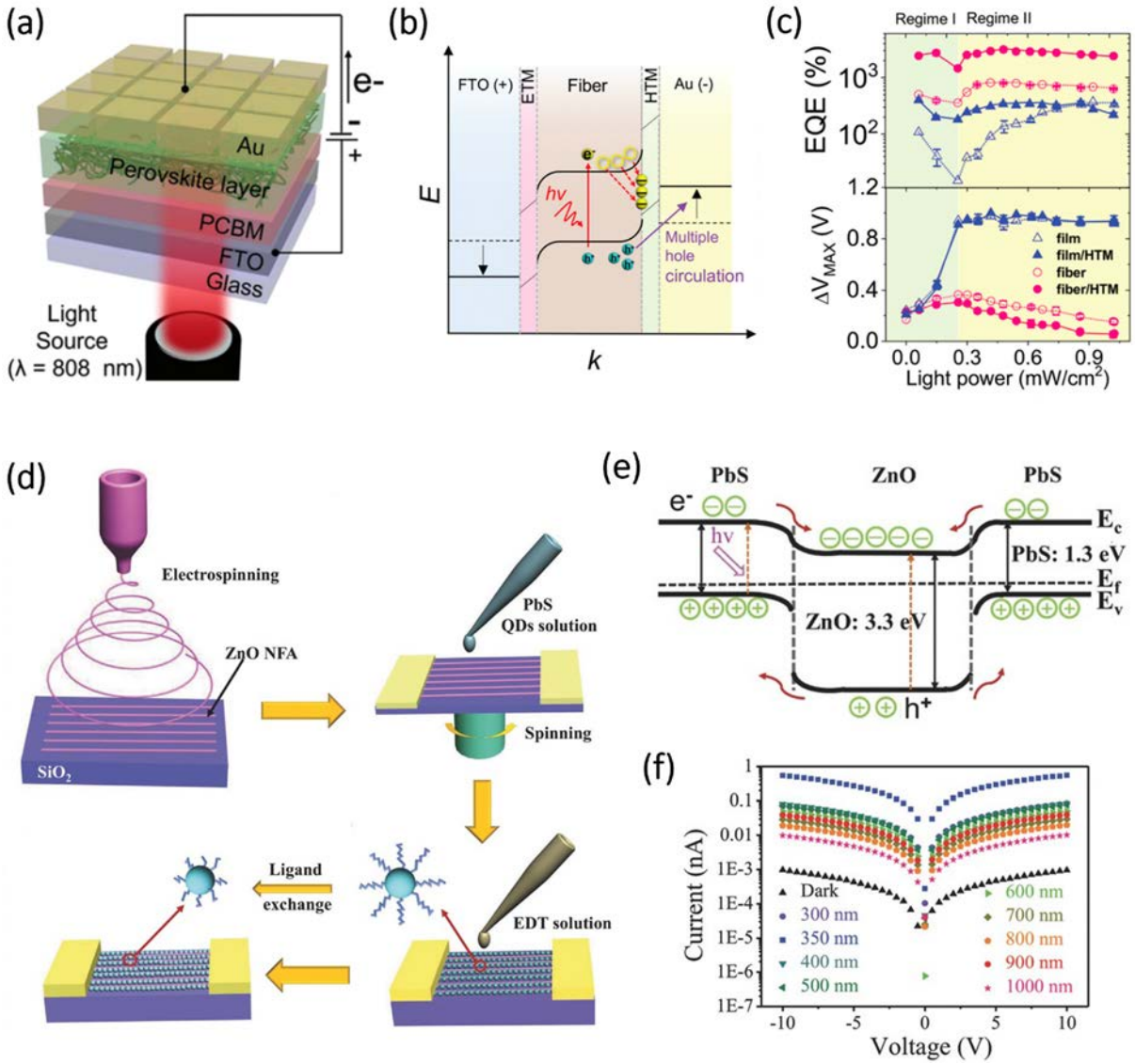


Fig. 12 Broadband photodetection enabled by trap assisted gain and heterojunction nanofibers. (a) Schematic illustration, (b) trap-assisted photomultiplication mechanism, and (c) external quantum efficiency of the NF-based photodetectors based on tri-cation perovskite fibers.[31] Reproduced with permission from ref. 31. Copyright 2022, John Wiley and Sons. (d) Schematic fabrication flow, (e) type-II band alignment, and (f) broadband photoresponse of aligned ZnO NFs decorated with PbS QDs.[33] Reproduced with permission from ref. 33. Copyright 2016, John Wiley and Sons.

repeatedly injected and collected, effectively multiplying the output signal per photon far beyond unity. The resulting external quantum efficiency (EQE) exceeds 3000%, as shown in Fig. 12c.[31] This photomultiplication mechanism illustrates how interfacial trapping, often regarded as detrimental, can be deliberately exploited to amplify weak optical signals in fibrous architectures. To achieve broadband detection across UV, visible, and NIR domains, Zheng *et al.* offer a different strategy: compositional heterojunction design. By ES ZnO NF arrays and integrating PbS quantum dots *via* ligand-exchange engineering, they formed a type-II heterostructure with spatially resolved electron-hole separation, as illustrated in Fig. 12d. The resulting structure forms a type-II heterojunction, where the conduction and valence bands are staggered to favor spatial separation of carriers (Fig. 12e). This band alignment, together with the expanded depletion region at the ZnO/PbS interface, creates a built-in field that efficiently drives electrons into the ZnO core and holes toward the QD shell, hindering electron–hole recombination and enabling broadband photocurrent generation. This design underscores the importance of spatial carrier separation in suppressing recombination losses across wide spectral ranges. Spectrally, the device responds impressively across UV, visible, and near-infrared domains, with distinct wavelength-selective features and fast switching behavior (Fig. 12f). Remarkably, this broad responsivity is retained even under extreme mechanical deformation, highlighting the spectral adaptability and structural resilience of the ES framework.[33]

Achieving broadband photodetection spanning ultraviolet to near-infrared wavelengths requires more than simply extending the absorption range. It involves designing how photoexcited carriers are generated, separated, and transported across diverse material domains. The two systems discussed here adopt different approaches: one enhances infrared sensitivity through trap-assisted photomultiplication, while the other combines materials with complementary band gaps to broaden the spectral response. Despite these differences, both rely on precise nanoscale structural control, where ES offers distinct advantages. This technique enables the formation of continuous, high-surface-area NF networks with controllable composition and morphology. It supports the integration of multiple functional components, facilitates tailored interfaces, and accommodates strain or deformation without sacrificing performance. By offering such structural and material flexibility, ES serves not only as a fabrication method but also as a conceptual framework for designing broadband photonic systems with controllable carrier dynamics.

### 4.2. Photonic synaptic devices

To overcome the limitations imposed by the Von Neumann architecture, artificial synaptic devices have emerged as a promising approach for enabling efficient, brain-inspired computing.[146–150] By emulating the essential functionalities of biological synapses, such as plasticity and adaptive learning, these devices offer a pathway to transcend the scaling limits of Moore's law at the device level.[35,151–153] ES NFs, with their high specific surface area, mechanical flexibility, and morphological resemblance to axonal structures, are desirable candidates for the construction of such devices. Moreover, their porous and interconnected architectures are well-suited for facilitating ion transport and interfacial coupling, both of which are critical for mimicking synaptic behaviors.[154,155] In this section, synaptic devices that have photonic and multi-mode functions will be introduced, as they share similar working principles.

**4.2.1. Tunable synaptic plasticity.** As an artificial synaptic device, mimicking various biological functions is crucial. The network structure of NF devices is similar to that of the biological synapse, which consists of the presynaptic membrane, synaptic cleft, and postsynaptic membrane. When an external stimulus stimulates the presynaptic membrane, it releases neurotransmitters into the synaptic gap, which then act immediately on the postsynaptic membrane, ultimately sending signals to the brain to generate the corresponding impulses. The strength of the connection between the presynaptic and postsynaptic is called synaptic weight. In general, the external stimuli of synaptic devices are typically driven by two main types of driving methods: electric and photonic fields, corresponding to electrical and optical synapses, respectively. Current measurements commonly assess synaptic function during external stimulation, thereby reflecting synaptic weight magnitude. As a fundamental test parameter, the postsynaptic current (PSC) changes with the strength of external stimulation. Based on the comparison of the relative magnitude of current values before and after stimulation, PSC can be divided into EPSC and inhibitory post-synaptic currents (IPSCs). Fig. 13a and b show that the PSC decays to a lower level after external stimulation is removed. Due to its decay time, the device exhibits characteristics of synaptic plasticity, which can be divided into short-term plasticity (STP) and long-term plasticity (LTP). For instance, paired-pulse facilitation (PPF) is the typical form of STP, which is induced by two identical continuous pulse signals, as illustrated in Fig. 13c and d. When the second spike pulse is larger than the first, it demonstrates that the device exhibits a memory effect under the first stimulus (Fig. 13c). In contrast, it is known as paired-pulse depression (PPD), as shown in Fig. 13d. The following equation can extract the PPF or PPD index:[156–158]

$$\text{PPF (or PPD) index} = (A_2/A_1) \times 100\% \quad (1)$$

Fig. 13e illustrates the PPF index as a function of the applied pulse interval, indicating that it decays exponentially with increasing intervals. The exponential decay relationship is described by eqn (2) as follows:[156]

$$\text{PPF (or PPD) decay} = C_1 \exp\left(-\frac{\Delta t}{\tau_1}\right) + C_2 \exp\left(-\frac{\Delta t}{\tau_2}\right) \quad (2)$$

where $\tau_1$ and $\tau_2$ represent the relaxation time, $C_1$ and $C_2$ are constants, and $\Delta t$ is the spike interval time. Moreover, the value of $\tau_2$ is usually an order of magnitude larger than $\tau_1$ in biological synapses. PPF, a common manifestation of STP, is crucial for the nervous system to process temporally sequenced information such as images and sound. In addition to short-term synaptic dynamics, biological synapses exhibit long-term changes in synaptic strength through spike-timing-dependent

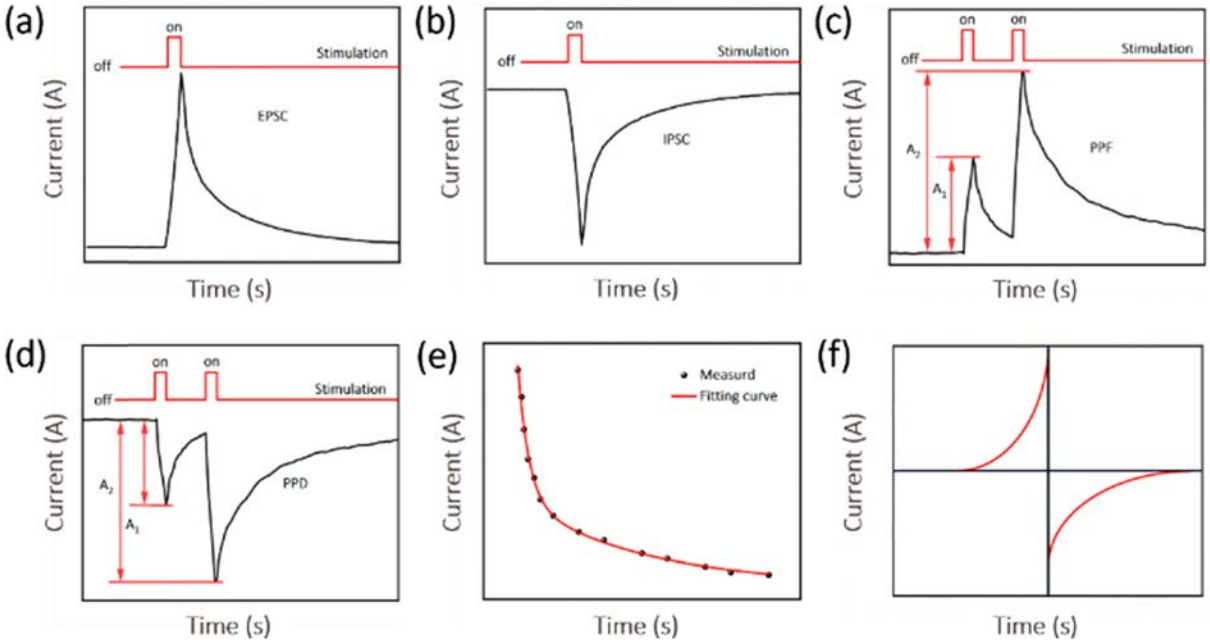


Fig. 13 Typical synaptic plasticity behaviors mimicking biological functions, including (a) EPSC curves, (b) IPSC curves, (c) PPF curves, (d) PPD curves, (e) PPF (PPD) index curves, and (f) STDP curves.

plasticity (STDP), which was proposed by Hebbian in the 1990s.[159] STDP describes how synaptic weight adjustments depend precisely on the relative timing between pre- and post-synaptic spikes: positive timing differences (pre-before-post) induce synaptic potentiation, while negative differences (post-before-pre) lead to depression, resulting in the characteristic asymmetric STDP curve (as shown in Fig. 13f). STP and STDP enable synapses to encode temporal information across multiple timescales efficiently. For artificial systems, reproducing these behaviors requires not only suitable materials but also carefully engineered defect states and interface kinetics.[160–162]

In biological neural systems, synaptic plasticity is central to memory formation and cognitive learning, as the ability of synaptic weights to change in response to stimuli.[163–165] This plasticity encompasses a dynamic transformation between short-term memory (STM) and long-term memory (LTM), as conceptualized in classical psychological models. External stimulation drives the brain to encode information into STM. Through repeated rehearsal, this information is consolidated into LTM, a process that is accompanied by information decay over time.[164] Translating this paradigm into neuromorphic electronics requires synaptic devices that can temporally modulate signal retention and gradually reinforce memory states.

Unlike photodetectors that prioritize ultrafast response, artificial synapses emphasize memory retention and functional plasticity.[166–170] ES NFs, with their high surface-to-volume ratio and porous structure, offer abundant surface states and confined pathways for carrier modulation.[35,75] These features are inherently advantageous for prolonging EPSC decay, a hallmark of LTM-like behavior.

In one strategy, Meng *et al.* developed a quasi-2DEG system based on $InGaO_3(ZnO)_3$ superlattice NFs to emulate optoelectronic synaptic functions. As shown in Fig. 14a–c, with increasing light-spike duration, intensity, or repetition rate, the EPSC decay time is significantly prolonged, reflecting a gradual transition from STP to LTP, consistent with Hebbian learning principles. Mechanistically, photo-generated carriers induce oxygen desorption from the NF surface, releasing trapped electrons and increasing channel conductance. Meanwhile, the superlattice core confines these carriers *via* quantum well structures, preventing rapid recombination and facilitating persistent current retention (Fig. 14d).[171] These synergistic effects enable a sub-femtojoule energy consumption per synaptic event and a responsivity of $1.05 \times 10^6$ A $W^{-1}$, surpassing most of the reported devices.

To further enhance synaptic tunability, Zheng *et al.* constructed ES artificial synapses using indium–zinc–tin oxide (IZTO) NFs with controlled In : Zn : Sn ratios. By adjusting the $In^{3+}$ concentration, the authors introduced a homojunction between cubic (c-$In_2O_3$) and rhombohedral (rh-$In_2O_3$) phases, forming an internal electric field that promoted directional charge separation under UV irradiation (Fig. 14e). Notably, the IZTO-9 device (In : Zn : Sn = 9 : 1 : 2) exhibited prolonged EPSC decay (Fig. 14f), attributed to inhibited electron–hole recombination across the phase interface (Fig. 14g). Under constant illumination, ~50% of the peak EPSC persisted after 3 hours, indicating a high degree of memory retention suitable for image recognition and neuromorphic integration.[154]

Together, these strategies illustrate how light-programmable synaptic behavior can be engineered *via* NF composition, hetero-interface design, and quantum confinement. The dynamic modulation between STM and LTM states mimics brain-like adaptability and opens new pathways for multi-bit optical memory, logic gating, and spatiotemporal data encoding in ES neuromorphic systems.[172]

 

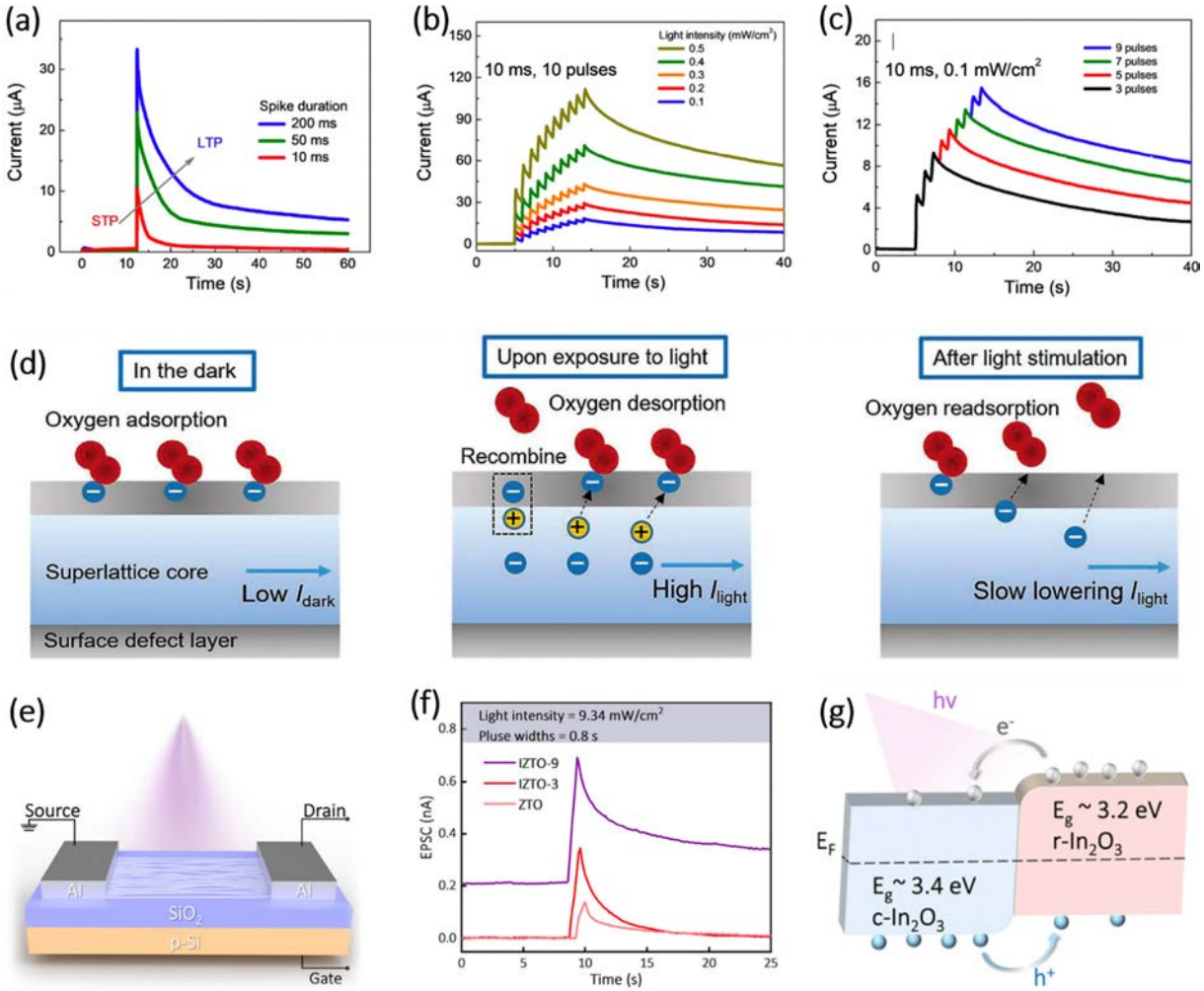


Fig. 14 Oxide NF synapses with optically tunable plasticity and charge trapping dynamics. (a) EPSC curves, (b) light intensity-dependent plasticity, and (c) pulse number-dependent plasticity of $InGaO_3(ZnO)_3$ NF-based photonic synaptic devices. (d) Schematics of oxygen adsorption-induced charge trapping and subsequent optically induced charge release on $InGaO_3(ZnO)_3$ NFs.[171] Reproduced with permission from ref. 171. Copyright 2022, distributed under a Creative Commons Attribution NonCommercial License 4.0 (CCBY-NC). (e) Schematic of IZTO NF-based photonic synaptic transistors under UV light illumination. (f) EPSC curves and (g) energy band diagram of IZTO NF-based photonic synaptic devices.[154] Reproduced with permission from ref. 154. Copyright 2023, Royal Society of Chemistry.

**4.2.2. Energy-efficient operations.** Minimizing the energy consumption per synaptic event is a fundamental requirement for the practical deployment of neuromorphic systems, particularly for large-scale, densely connected networks. In conventional Von Neumann architectures, memory and processing units are physically separated, so running neural networks requires incessant data shuttling between the two units. As network depth and parameter count increase, memory access and data movement become the dominant factors in the total energy budget, resulting in high power consumption and significant thermal management issues. In contrast, the human brain executes massive numbers of synaptic operations while consuming only ~20 W, benefiting from highly parallel, in-memory processing where information storage and computation are inherently co-localized. This motivates the development of artificial synaptic devices that emulate biological synapses and integrate nonvolatile weight storage with local signal processing at the device level. By suppressing data movement and performing synaptic updates *in situ*, such neuromorphic hardware offers a promising route toward low-power computation suitable for dense on-chip integration and energy-constrained edge or wearable systems.

To accurately assess energy efficiency, distinct calculation methods are adopted for electrical and optoelectronic synaptic devices, reflecting their respective input modalities. For electrical synapses, the energy consumption per event is typically estimated by:[173]

$$E_1 = I_{peak} \times V \times \Delta t \quad (3)$$

where $I_{peak}$ is the transient peak current during the stimulation pulse, $V$ is the applied voltage, and $\Delta t$ is the pulse duration. This formulation implies that energy reduction can be achieved by suppressing either the driving voltage, the current response, or shortening the stimulation time window. Many recent

studies have demonstrated sub-nanojoule consumption through material engineering or device structure optimization. For instance, employing low-dimensional semiconductors with high carrier mobility and narrow-bandgap oxides to facilitate charge transport under minimal excitation. In contrast, optical synapses, which emulate the photonic sensitivity of biological visual systems, typically adopt one of two evaluation schemes:[174,175]

$$E_2 = P \times S \times \Delta t \quad (4)$$

$$E_3 = I_{peak} \times V \times \Delta t + P \times S \times \Delta t \quad (5)$$

eqn (4) only considers the optical excitation energy, where $P$ is the optical power density, $S$ is the effective illumination area, and $\Delta t$ is the light pulse duration.[176] This model is suitable when the photonic stimulus alone triggers the synaptic response. However, both light and bias voltage are involved in photoelectric co-stimulation scenarios. Eqn (5) is adopted to reflect total energy input, summing both electrical and photonic contributions. It is noteworthy that while optical devices offer advantages such as contactless stimulation and wavelength selectivity, their energy efficiency heavily depends on the light absorption cross-section and the quantum efficiency of the active material. Hybrid perovskites, transition-metal dichalcogenides (TMDs), and low-dimensional metal oxides have been investigated to enhance the photoresponse at ultra-low power densities, yet achieving sub-pJ energy per event remains challenging.[177–179]

Recent progress has shown that interfacial band engineering can directly suppress the stimulation energy required for photonic synapses by enabling charge trapping and transport at vanishing electrical bias. Zheng *et al.* constructed a two-terminal ZnO/GO (Graphene oxide) heterostructure in which ZnO nanofibers serve as the photosensitive oxide, and GO provides deep electron-accepting states (Fig. 15a).[180] The nearly flat Fermi level alignment at the interface, with an energy offset of approximately 0.07 eV, allows minority carriers to be captured without a built-in barrier. Oxygen vacancy defects in ZnO act as shallow traps that sustain persistent photoconductivity. Under weak 365 nm illumination and an electrical bias of only 1 mV, the device produces clear excitatory postsynaptic spikes (Fig. 15b). It maintains a long decay tail due to defect-assisted retention. As a result, the per-spike energy can be suppressed to 23 fJ at 1 mV, representing the lowest reported value among optoelectronic synapses and well below the sub-picojoule level shown in the comparison plot (Fig. 15c). The schematic energy diagrams in Fig. 15d visualize the carrier motion from ZnO into GO under illumination, the accumulation of trapped electrons, and the slow recombination process that enables long-lived potentiation without external electrical drive.

After this demonstration of an oxide-carbon junction, Yang *et al.* turned to a full-oxide heterojunction to further lower photonic operating costs and remove organic variability.[181] Their planar ITO/ZnAlSn (ZATO)/SnO/ITO configuration (Fig. 15e) combines an n-type amorphous ZATO channel with a p-type SnO absorber and operates entirely under visible wavelengths. The synaptic readout voltage is only 0.1 V, and LTP can be induced by light at 635 nm. The calculated event level energy is 0.75 pJ for a 0.1 s visible stimulus according to the expression $I_{DS} \times V_{DS} \times \Delta t$. Optical responses recorded at different wavelengths (Fig. 15f) exhibit strong excitatory behavior under red illumination. At the same time, green and blue triggers elicit inhibitory responses that support LTD or a rapid RESET. The relaxation curves in Fig. 15g confirm that synaptic depression is controlled by photon energy rather than electrical amplitude.

The transport picture in Fig. 15h explains this operation mechanism. SnO acts as a p-type semiconductor with a shallow valence-band edge and strong visible absorption. ZATO behaves as an n-type layer with donor states that originate from oxygen vacancies. Under illumination, SnO injects holes into ZATO, and ZATO defects can be ionized to form $V_O^{2+}$ (oxygen vacancy) centers and free electrons. These processes enable charge storage without high electrical bias. Viewed together, the two studies reflect a gradual evolution in low-power photonic synapse design. The ZnO/GO interface demonstrates that a flat band condition and defect storage enable femtojoule-level activation under millivolt bias. The ZATO/SnO full-oxide junction extends this concept to visible-light-controlled potentiation and depression with sub-picojoule energy, while maintaining compatibility with microelectronic processing. This progression suggests that material selection, band alignment, and controlled defect ionization can replace electrical drive, guiding photonic neuromorphic hardware toward brain-level energy efficiency.

In summary, optimizing the energy consumption of synaptic devices requires more than simply adjusting basic parameters such as voltage or pulse duration. A system-level approach is essential in integrating material properties, device architecture, and stimulation strategies.[182–184] For instance, the energy band structure and interface states of the active material significantly affect charge transport efficiency; structural configurations (*e.g.*, heterojunctions or core–shell architectures) determine photocarrier pathways; and the mode of stimulation (electrical, optical, or hybrid) dictates how energy is introduced into the system.[9,185,186] A summary of the energy consumption of representative recent synaptic devices is provided in Table 2 for a clearer comparison of their power performance. Future research should therefore emphasize the co-design of materials and device structures, alongside the establishment of standardized protocols for energy measurement. This would enable meaningful comparisons across studies and ensure that improvements in energy efficiency are not achieved at the expense of other critical metrics, such as device stability or integration capability. Only by meeting these multiple requirements in tandem can artificial synaptic devices advance toward practical deployment.

**4.2.3. Multimodal neuromorphic functions.** For real-world interaction, neuromorphic hardware should not only modulate synaptic weights and reduce energy consumption, but also sense and fuse different physical cues in a unified platform. Multimodal synaptic devices address this need by encoding thermal, mechanical, or optical stimuli into common electrical variables and feeding them directly into computing blocks. Such architectures are attractive for "in-sensor" and "in-skin" computing, where perception and learning occur locally rather than in remote processors.[192]

 

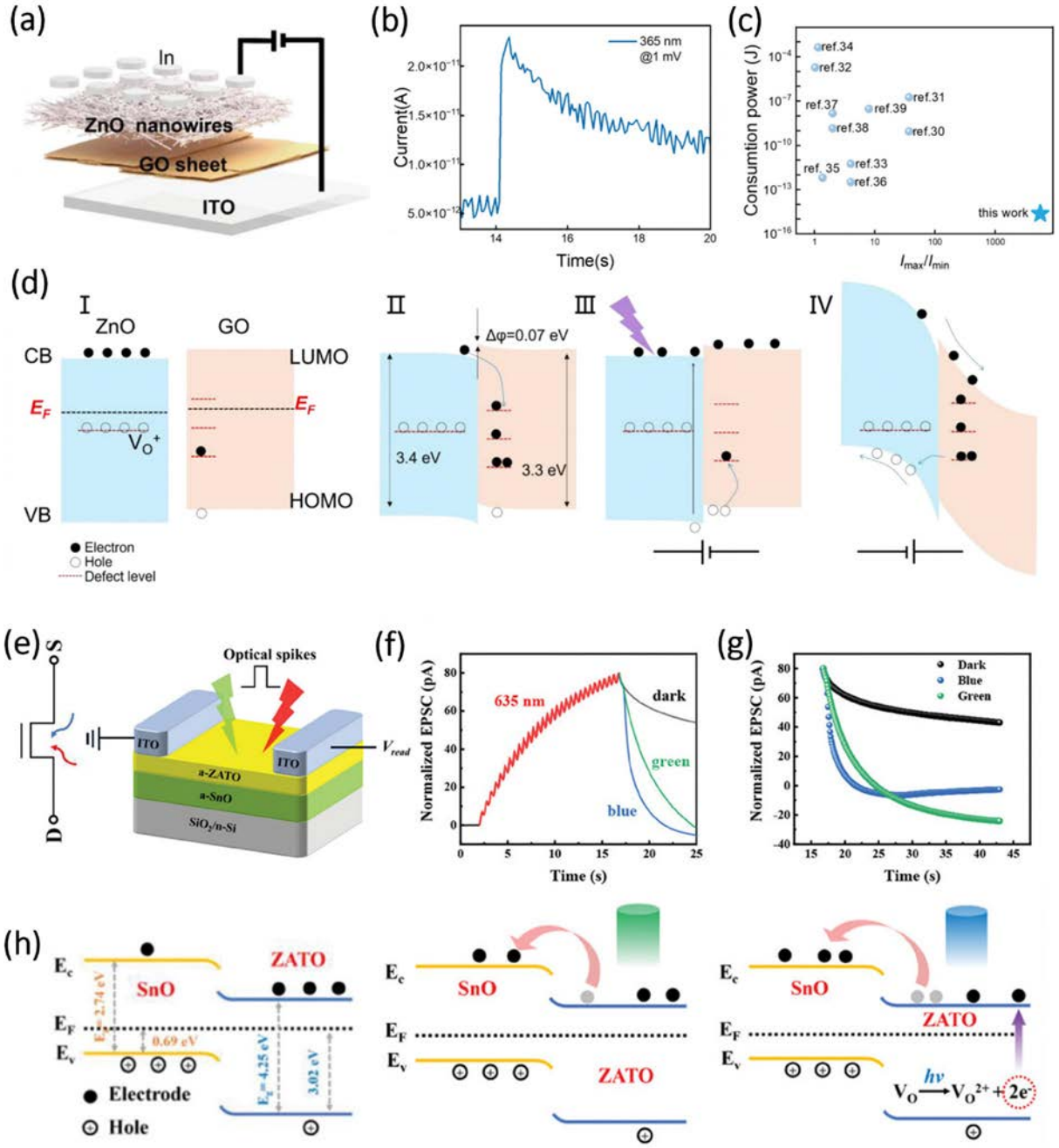


Fig. 15 Heterostructure engineered ultralow-power photonic synapses. (a) Schematic of an optoelectronic synaptic device. (b) Typical UV light-stimulated postsynaptic current response, (c) energy consumption comparison, and (d) corresponding band-alignment mechanisms.[180] Reproduced with permission from ref. 180. Copyright 2025, under the terms of the Creative Commons CC BY license. (e) Device structure of a full-oxide optical synapse using the ZATO/SnO heterojunction. (f) Wavelength-dependent excitatory synaptic responses, (g) light colour-dependent optical LTP/D, and (h) schematic carrier-transport mechanisms.[181] Reproduced with permission from ref. 181. Copyright 2023, John Wiley and Sons.

Kim *et al.* proposed an interleaving multimodal skin receptor based on a memristive NF network. Fig. 16a compares three information-flow schemes, highlighting the conceptual shift that occurs. Conventional multimodal systems rely on separate sensors and readout circuits for each modality, which increases wiring complexity and limits areal resolution. In contrast, biological neurons interleave different spike trains in a single axon before the signals reach the somatosensory cortex. The memristive interleaving architecture follows this neural strategy. Fig. 16b shows the device core, consisting of a stretchable Ag@$Cu_2O$ core–shell NF network laminated onto a soft substrate. The Ag core forms a mechanosensitive conductive pathway, while the $Cu_2O$ shell provides a thermosensitive, high-resistance channel. By programming the memristive state, the network switches between a thermally dominated T mode and a mechanically dominated M mode. Distinct network geometries

Table 2 Comparison of the energy consumption of recently reported ES-based synaptic devices

| Materials | Synaptic type | Calculated formula | Energy consumption | Ref. |
|---|---|---|---|---|
| InMgO NFs | Ionic synapse | Eqn (3) | 418 fJ | 187 |
| ZnO NFs | Electrical synapse | Eqn (3) | 63.168 fJ | 188 |
| InSnMgO NFs | Ionic synapse | Eqn (3) | 1.25 pJ | 86 |
| Ion-gel PVDF NFs | Ionic synapse | Eqn (3) | 6 fJ | 189 |
| InGaZnO NFs | Optical synapse | Eqn (4) | 15 fJ | 190 |
| PEDOT:PSS/PAAm NFs | Ionic synapse | Eqn (3) | 113 fJ | 191 |
| InAlZnO NFs | Ionic synapse | Eqn (3) | 75 fJ | 155 |
| InZnO NFs | Ionic synapse | Eqn (3) | 38.45 fJ | 135 |
| PQT-12:PEO NF | Ionic synapse | Eqn (3) | 3.9 fJ | 36 |

in these two modes result in different dependencies on modulus and thermal conductivity, allowing a single resistance trace to encode interleaved thermomechanical information. This design illustrates a fundamental principle for multimodal synaptic systems: heterogeneous physical cues can be condensed into a single scalar state variable over time, which relaxes interconnect constraints while preserving material specificity. Fig. 16c emphasizes the analogy to biological interleaving. In the neural case, receptors for signals A and B project onto a single neuron, where action potentials are temporally interleaved and later decoded in the brain. In the memristive receptor, switching between T and M modes interleaves thermo- and mechano-signals in an NF network, and a downstream neural network decodes the sequence to identify unknown objects.[193] Compared with traditional stacked multimodal sensors, this approach trades spatial separation for temporal coding. It points to a broader design rule: multimodal "synapses" can serve as compact front-ends that pre-encode rich physical descriptors into time-series signals, which are naturally suited for neuromorphic processing.

Reservoir computing offers a hardware-efficient approach to processing time-encoded signals. Zhang *et al.* developed flexible tunable-plasticity synaptic transistors (TSTs) based on IGZO channels and hybrid PI/$Al_2O_3$ dielectrics, and used them as physical reservoirs. In these devices, carriers can be weakly coupled to polar groups or deeply trapped at PI/$Al_2O_3$ interfaces. As stimulus amplitude changes, the response evolves from STM to LTM, resulting in a mixed fast–slow conductance dynamics. Fig. 16d illustrates the reservoir computing pipeline. Time-dependent input pulse trains are encoded and applied to a TST array.[194] The resulting EPSC transients span a high-dimensional state space in the reservoir layer. Different pulse sequences travel along distinct trajectories, so even a small array can separate 16 different 4-bit pulse patterns using a simple linear readout. Importantly, this reservoir operates without explicit recurrent wiring, and the intrinsic device memory provides the required fading dynamics. From a design perspective, such TST reservoirs are a good match to interleaved multimodal receptors. Both generate rich, history-dependent temporal signals and exploit device-level physics rather than complex circuit topologies.

Beyond temporal coding, multimodal neuromorphic systems also perform static pattern recognition with high accuracy. Kwon *et al.* reported IGZO synaptic transistors with an $Al_2O_3/HfO_2$ dielectric stack that show frequency-dependent competition between ferroelectric polarization and trap-assisted switching. By tuning the pulse frequency at fixed amplitude, the dominant mechanism switches between polarization-driven and trapping-driven conductance modulation. This dual-mode operation enables almost linear potentiation and depression, single-polarity weight updates, and a recognition accuracy of about 97% for handwritten digits in an artificial neural network (ANN). Fig. 16e sketches a typical ANN inference flow, in which a 28 × 28-pixel digit is flattened into the input layer, synaptic devices store trainable weights as conductance states, and repeated pulsing gradually shapes the weight map until the network classifies digits with high fidelity.[195] In the context of multimodal systems, the frequency-selective plasticity is particularly attractive. It provides a simple way to assign different learning rules or update speeds to different temporal patterns or sensory channels without changing the circuit topology.

Taken together, Fig. 16 outlines a coherent path from multimodal sensation to neuromorphic computation. Memristive NF networks function as compact "skin synapses", compressing thermal and mechanical cues into interleaved resistance trajectories with high spatial and temporal resolution. Flexible tunable-plasticity synaptic transistors transform these time-series inputs into separable reservoir states, enabling hardware-efficient temporal coding. Dual-mode ferroelectric–trap synaptic transistors and related arrays offer linear and programmable weight updates that support high-accuracy digit recognition, even in relatively small networks. Beyond summarizing these individual demonstrations, the combined message is that multimodal neuromorphic hardware should be co-designed across three levels: materials encode multiple stimuli, devices provide nonlinear yet controllable dynamics, and system architectures exploit temporal coding and selective plasticity. Looking forward, integrating these functionalities into a single electrospun or flexible platform could lead to "intelligent skins" that sense, encode, and interpret multimodal information directly at the edge.[196] Such systems would reduce data traffic and energy consumption by performing feature extraction and partial inference locally, while central processors handle only higher-level tasks. Key challenges include stabilizing memristive networks under long-term mechanical deformation, matching the dynamic range of reservoirs to realistic sensory signals, and developing on-device training schemes that can adapt to changing environments without external supervision. Addressing these issues will be crucial for transitioning from proof-of-concept multimodal synaptic devices to scalable neuromorphic systems for robotics, wearable healthcare, and human–machine interfaces.

## 5. Electronics based on electrospinning

In addition to enabling versatile optoelectronic functionalities, ES technology has demonstrated remarkable potential in advanced electronics. Due to its inherent advantages (such as high surface-to-volume ratio, tunable dimensionality, and

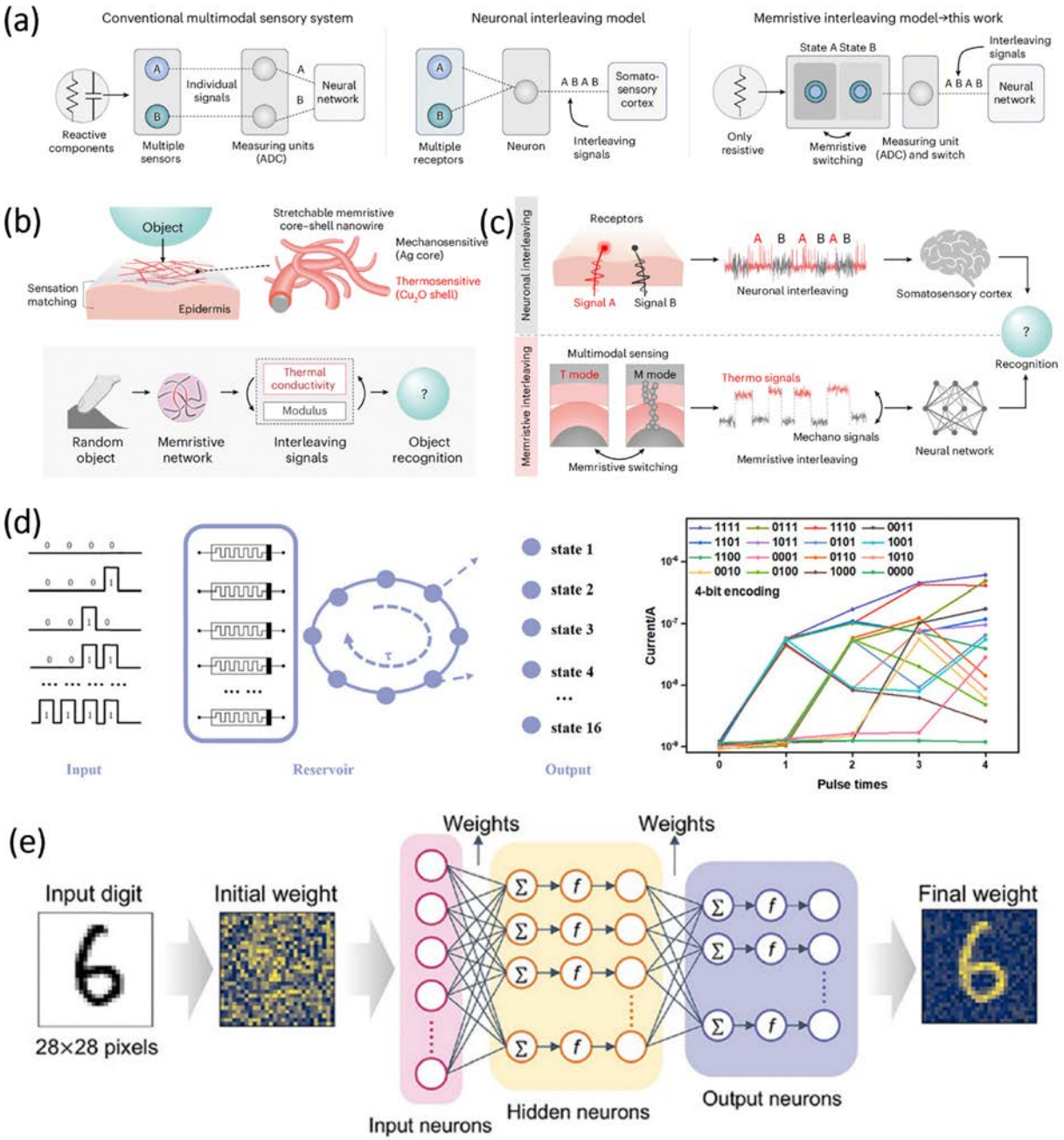


Fig. 16 Neuromorphic networks for multimodal sensing and reservoir computing. (a) Comparison of different architectures, including the conventional multimodal system, neural interleaving model, and memristive interleaving system. (b) Schematic of the interleaving memristive NF network sensor. (c) Memristive switching interleaves thermal signals and mechanical signals.[193] Reproduced with permission from ref. 193. Copyright 2025, Springer Nature. (d) Schematic diagram of the reservoir computing, including input, reservoir, and output layers.[194] Reproduced with permission from ref. 194. Copyright 2025, John Wiley and Sons. (e) Artificial neural-network architecture used for handwritten-digit classification tasks.[195] Reproduced with permission from ref. 195. Copyright 2025, John Wiley and Sons.

compatibility with flexible substrates), electrospun NFs offer a fertile platform for building next-generation electronic devices that demand mechanical adaptability, structural miniaturization, and multifunctional integration.[197]

This chapter discusses three major electronic device categories empowered by ES: FETs, gas sensors, and triboelectric nanogenerators (TENGs). Each section highlights how NF design and interfacial engineering can be leveraged to enhance device performance and broaden the functional scope.[93,100,198] For instance, by constructing NF-based semiconducting channels, ES FETs achieve desirable electrical modulation and exhibit excellent mechanical flexibility. In gas sensors, NF scaffolds facilitate rapid molecular diffusion and increase reactive surface area, thereby enabling high sensitivity and selectivity. Meanwhile, integrating NF networks into TENG architectures enables efficient mechanical-to-electrical energy

conversion, supporting the development of self-powered electronic systems.

By systematically summarizing the device architectures, material strategies, and operating mechanisms within each category, this chapter aims to elucidate the distinctive role of ES in shaping the landscape of intelligent electronics. Through the lens of fiber-enabled control over charge transport, surface interactions, and energy transduction, we underscore the potential of this scalable technique for wearable, stretchable, and self-sustained electronic systems.

### 5.1. Field effect transistors

ES has emerged as a versatile method for creating high-performance NFs of metal-oxide semiconductors, offering precise control over diameter, composition, and microstructure. This tunability enables researchers to optimize FET performance for diverse applications ranging from logic circuits to biosensing.[199–201]

**5.1.1. Solid-state transistors.** ES NFs offer unique structural and compositional tunability, enabling channel engineering from dopant coordination to morphological confinement at multiple levels. Research by He *et al.* exemplifies how precise dopant control within oxide NFs can unlock synergistic electrical characteristics. As illustrated in Fig. 17a, the authors adopted a bottom-gate top-contact architecture. They varied the Zn doping concentration in the $In_2O_3$ precursor solution to modulate the NF crystallinity and carrier dynamics. By systematically modulating the Zn content in $In_2O_3$, they identified a critical composition (In : Zn = 1 : 1) where the transition toward an amorphous phase suppresses grain boundary scattering while preserving high carrier concentration. Their findings revealed that a 50 mol% Zn doping ratio yields the optimal trade-off between amorphization and conductivity (Fig. 17b and c). At this optimized composition, Zn incorporation induces partial amorphization, suppressing grain-boundary scattering while preserving a sufficient carrier density. This balance

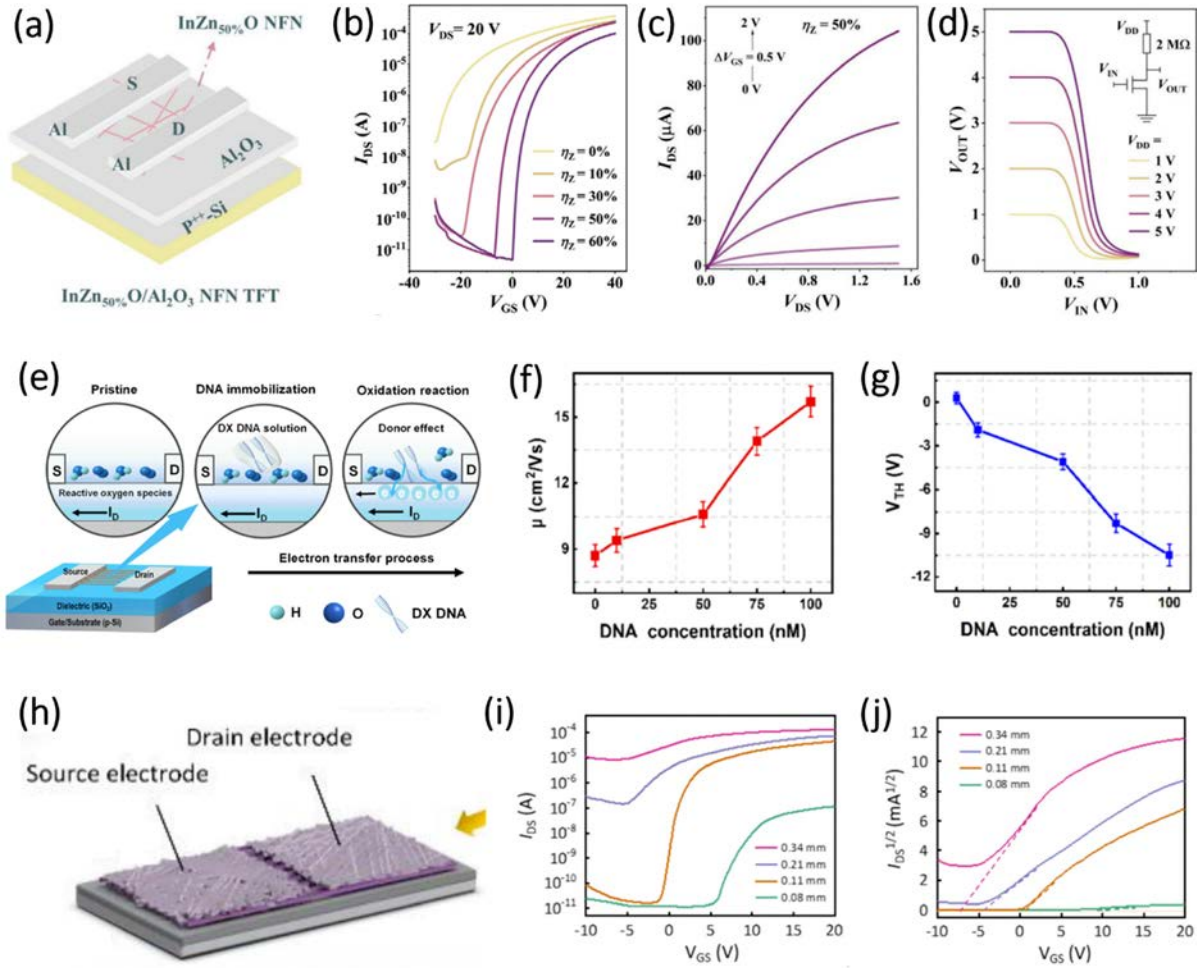


Fig. 17 Electrospun oxide NF transistors for solid-state logic and biosensing. (a) Schematic diagram of InZnO NF-based FETs. (b) Transfer characteristics, (c) output characteristics, and (d) voltage transfer curves based on the InZnO NF device.[88] Reproduced with permission from ref. 88. Copyright 2023, John Wiley and Sons. (e) Schematic diagram of DNA detection based on the Gd-doped $In_2O_3$ NF device. (f) Variation of $\mu$ and (g) $V_{th}$ with DNA concentration of the Gd-doped $In_2O_3$ NF device.[87] Reproduced with permission from ref. 87. Copyright 2023, American Chemical Society. (h) Schematic diagram, (i) transfer characteristics, and (j) corresponding $(I_{DS})^{1/2}$–$(V_{GS})$ curves based on the all NF-based ITO transistor.[25] Reproduced with permission from ref. 25. Copyright 2023, Springer Nature.

between structural disorder and electrical conduction highlights how electrospinning-enabled compositional tuning can regulate charge transport pathways at the nanoscale. Notably, the successful implementation of inverter operation confirms that electrospun oxide nanofibers are not limited to single-device demonstrations but are compatible with logic-level circuit integration, which is critical for scalable electronics (Fig. 17d).[88] This study highlights the interlinkage between material, process, and performance, and affirms ES as a scalable method for optimizing the amorphous phase.

Expanding from electronic performance to functional responsiveness, Zhang *et al.* took advantage of aligned, Gd-doped $In_2O_3$ NFs to create a FET capable of detecting deoxyribonucleic acid (DNA). In Fig. 17e, the enlarged schematic shows how reactive oxygen species (*i.e.*, $O_2^-$, $O^-$, $O_2^{2-}$) form on the NF surface when exposed to air. Once the device is introduced into a DNA environment, guanine reacts with $O_2^-$, releasing extra electrons into the conduction band and raising the channel's carrier concentration. Consequently, both the mobility ($\mu$) and threshold voltage ($V_{th}$) exhibit significant shifts in response to varying DNA concentrations, as shown in Fig. 17f–g.[87] This effect demonstrates high DNA sensitivity at room temperature, marking a key advancement in biosensing applications. This approach suggests that ES oxide NFs can serve as both signal transducers and selective recognition interfaces, particularly when spatial orientation and doping chemistry are co-engineered.

Beyond channel engineering, Chen *et al.* used ES to fabricate an all-NF FET in which both the channel and the electrodes are composed of indium tin oxide (ITO). As depicted in Fig. 17h, the researchers leveraged the tunable properties of ITO NFs, which can transition between conductor-like and semiconductor-like behavior by adjusting the ES needle diameter. The transfer curves (Fig. 17i) confirm n-type conduction across different diameters, while the threshold voltage systematically shifts from −7 to +9 V with decreasing needle diameter (Fig. 17j).[25] This shift indicates a transformation from depletion mode to enhancement mode, underlining the versatility of ES ITO FETs for integrated electrode-channel designs.

Collectively, these studies highlight how ES is more than a morphology-shaping technique. It is a powerful platform for deterministic control over charge transport, phase states, surface interactions, and even the implementation of logic functions. Whether through dopant chemistry, aligned architecture, or scalable integration, ES NFs are redefining how we build, sense, and operate thin-film transistors within a multifunctional, intelligent electronics landscape.

**5.1.2. Ionic-gated transistors.** The integration of ion-gel dielectrics with ES NF channels represents a significant paradigm shift in FET design, especially for applications demanding either mechanical adaptability or ultra-low voltage operation. Unlike conventional solid-state gate dielectrics, ion gels exhibit high capacitance, enabling effective carrier accumulation even lower gate biases. When combined with the structural advantages of ES NFs, this approach opens new opportunities for flexible electronics, neuromorphic computing, and low-power sensor arrays. From a device physics perspective, ionic gating introduces electrostatic control by forming electric double layers (EDLs), which localize charge at the semiconductor–dielectric interface. This mechanism is fundamentally distinct from traditional capacitive gating and is particularly advantageous for modulating nanostructured or high-defect-density semiconductors. Moreover, ionic-fated transistors (*e.g.*, ion-gel/organic NF or ion-gel/oxide NF) provide additional mechanical resilience or interfacial conformability, which is critical for stretchable and wearable electronics.[107,198]

On the one hand, Shin *et al.* demonstrated a fully stretchable FET comprising ES P3HT NFs, SBS (Styrene–Butadiene–Styrene) fiber mat substrate, and ion-gel gating. As shown in Fig. 18a, the entire device is constructed from mechanically compliant components. As illustrated in Fig. 18b, the SEM image of the actual device shows the P3HT fibers bridging the Au S/D electrodes embedded in the ion-gel region. The inset shows a top-view image of an arrayed device configuration. The interpenetrating network between the gel and the fibrous substrate not only preserved electrical integrity under large strain but also stabilized transistor operation over 1500 stretching cycles (Fig. 18c).[198] The interpenetrating fiber–gel network effectively redistributes mechanical stress while preserving electrostatic integrity, suggesting that mechanical compliance in electrospun systems can be engineered at the network level rather than solely at the material level.

On the other hand, Kim *et al.* developed high-mobility dual-gate FETs using ES crystalline Ga-doped $In_2O_3$ NFs as the channel and a top ion-gel layer for enhanced gating efficiency. Fig. 18d illustrates the stepwise fabrication process of the dual-gate device: starting from ES of Ga-doped $In_2O_3$ precursors onto $Si/SiO_2$ substrates, followed by thermal calcination to convert polymeric fibers into crystalline NWs. Subsequently, source/drain electrodes are formed, yielding a single-gate FET. An ion-gel top gate is then patterned to complete the dual-gate configuration (with $V_{G1}$ as the bottom gate and $V_{G2}$ as the ion-gel top gate). The transfer characteristic of an ion-gel-gated $IGO_3$ NF FET shows typical n-type behavior with a sharp turn-on and high on/off ratio, as shown in Fig. 18e. Fig. 18f–h present a comprehensive evaluation of the electrical performance of ion-gel-gated $IGO_3$ NF FETs fabricated *via* ES.[107] The statistical uniformity across multiple devices indicates that electrospinning can produce crystalline oxide nanofibers with reproducible doping and defect control, addressing a common concern regarding batch variability in fiber-based electronics. The dual-gate configuration enabled tunable threshold voltage and mobility enhancement (up to 35.1 $cm^2\ V^{-1}\ s^{-1}$), surpassing those of single-gate oxide NW FETs. Notably, the study demonstrated that ES can fabricate crystalline, defect-minimized oxide NFs with controllable doping and microstructure. Together, these advances point to a broader vision where ionic gating and ES nanostructures function not just compatibly, but with intrinsic synergy. ES provides the freedom to pattern or align functional channels across diverse substrates spatially. At the same time, ion gels bridge the gap between electrostatics and electrochemistry, enabling voltage-scalable and mechanically adaptive gating schemes.

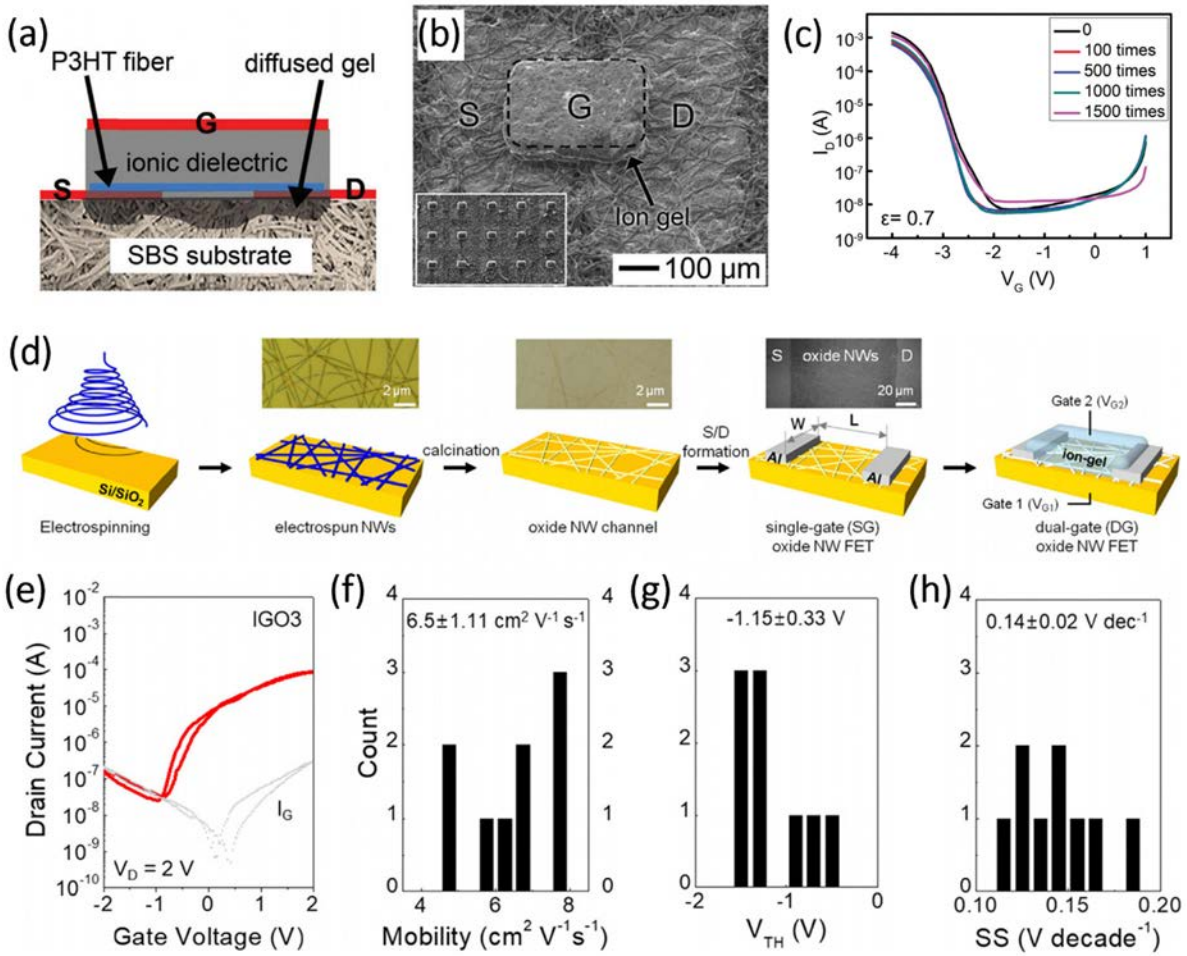


Fig. 18 Ion-gel gated NF transistors for enhanced switching performance. (a) Schematic diagram, (b) SEM image, and (c) transfer curves of the ion-gel gated P3HT NF FETs.[198] Reproduced with permission from ref. 198. Copyright 2014, John Wiley and Sons. (d) Fabrication process flow of dual-gate oxide NF FET. (e) Transfer characteristics and statistical distribution of (f) mobility, (g) $V_{th}$, and (h) SS of ion-gel-gated $IGO_3$ NF FETs.[107] Reproduced with permission from ref. 107. Copyright 2020, Elsevier.

Nevertheless, ion-gel FETs often suffer from limited switching speed due to ionic migration, and their long-term stability under ambient conditions has yet to match that of conventional dielectrics. Furthermore, precise patterning of ion-gels at the sub-micrometer scale and their compatibility with high-resolution lithography are active areas of exploration. For NF-based FETs, issues such as fiber–to–fiber contact uniformity, batch-to-batch reproducibility, and integration with scalable logic architectures remain to be addressed. Looking ahead, the convergence of ionic gating and ES NF technology is expected to enable new device paradigms, including artificial synapses with dynamic reconfigurability, conformable logic systems, and multiplexed biochemical interfaces. Future efforts may benefit from integrating bio-derived ion gels, multi-gate logic schemes, or hybrid ionic–electronic coupling mechanisms that leverage the nanoscale geometry of ES networks.

### 5.2. Gas sensors

Among the various applications of ES optoelectronic devices, gas sensing has emerged as a particularly promising domain due to its critical role in environmental monitoring, health diagnostics, and intelligent human–machine interfaces.[202–204] ES offers a unique material platform for gas sensors, enabling the fabrication of nanofibrous networks with ultrahigh surface-to-volume ratios, hierarchical porosity, and tunable surface chemistry. These structural features facilitate gas diffusion, adsorption, and charge interaction, forming the basis for rapid and sensitive analyte detection. Beyond morphology, the performance of ES gas sensors is increasingly governed by nanoscale interfacial engineering. In particular, the rational design of electronic junctions, including metal–semiconductor (MS) contacts and semiconductor–semiconductor (SS) heterojunctions, is crucial for achieving optimal performance. It enables precise modulation of charge carrier dynamics and surface reactions in response to gas exposure.[93–95,205] These interfacial architectures act as built-in signal amplifiers, enhancing sensitivity, selectivity, and environmental robustness. In the following sections, we highlight recent advances in ES-enabled gas sensors, focusing on how MS and SS interfaces have been harnessed to optimize sensing performance. By comparing their respective design

 

logics, working principles, and integration strategies, we aim to provide a comprehensive understanding of interface-driven sensing mechanisms within ES architectures.

**5.2.1. Metal-semiconductor heterojunctions.** MS heterojunctions have emerged as a powerful strategy for gas sensing due to their ability to modulate charge-carrier transport, facilitate catalytic reactions, and amplify sensor responses. When noble metal nanoparticles are interfaced with semiconducting NFs, Schottky barriers can form at the junction, creating electron-depleted or -accumulated regions susceptible to gas adsorption-induced surface charge changes. This interfacial architecture enables both high sensitivity and improved selectivity, particularly when integrated with nanostructured designs and multifunctional interfaces. In a representative example, Lim *et al.* developed a transparent $NO_2$ sensor composed of patterned Au–$SnO_2$ NFs fabricated *via* near-field ES (NFES), as illustrated in Fig. 19a. The NFES process enables precise deposition of polymer/precursor fibers (a1–a4), followed by

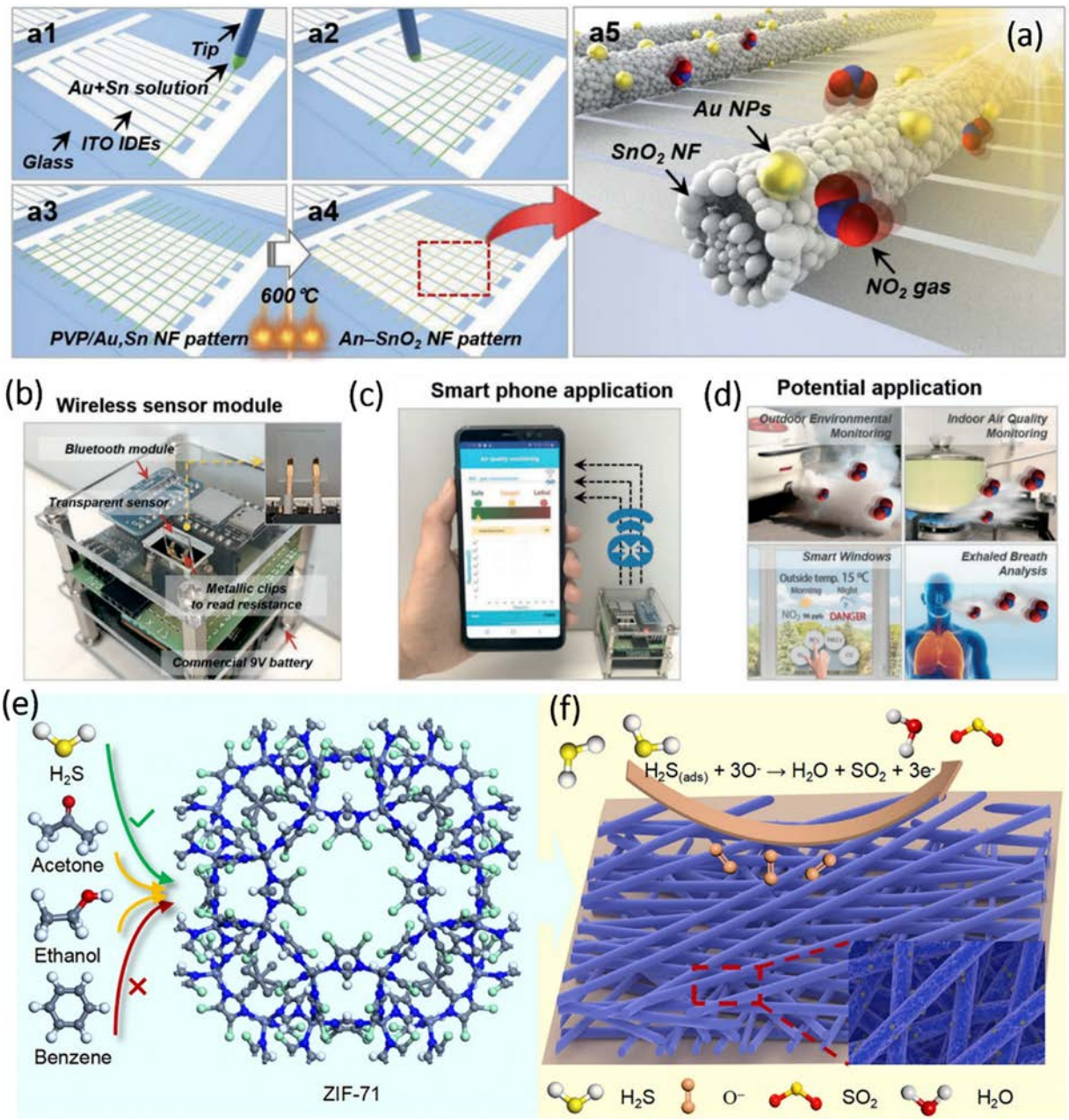


Fig. 19 Metal-semiconductor heterojunction NFs for selective gas sensing. (a) Fabrication process of Au–$SnO_2$ NF sensors *via* direct-write near-field ES on ITO/glass substrates. (b) Photograph, (c) real-time air quality monitoring, and (d) other potential applications of a wireless gas sensing module using transparent Au–$SnO_2$ NFs.[92] Reproduced with permission from ref. 92. Copyright 2021, John Wiley and Sons. (e) Molecular sieving effect of the ZIF-71 membrane, selectively allowing $H_2S$ molecules (~3.6 Å) to pass while excluding larger interferents. (f) Schematic of the $H_2S$ sensing mechanism in Ru–CuO@ZIF-71 NFs, including gas adsorption, oxidation on Ru sites, and Schottky barrier modulation.[205] Reproduced with permission from ref. 205. Copyright 2024, Springer Nature.

thermal annealing to obtain crystalline Au-decorated $SnO_2$ NFs. The resultant structure exhibits high optical transparency due to its ultralow surface coverage ($\sim$0.3%) and aligned fiber geometry. At the microscopic level, Au nanoparticles form MS junctions with the $SnO_2$ backbone, where the localized surface plasmon resonance (LSPR) effect under visible light enhances photoactivation and catalyzes $NO_2$ adsorption. This synergistic interaction between plasmonics, catalysis, and electronic modulation allows the device to achieve ppb-level $NO_2$ detection at room temperature with excellent selectivity and reproducibility. Crucially, the sensor was optimized at the material level and integrated into a practical, user-oriented system. Fig. 19b shows a wireless sensing module that incorporates the transparent NF sensor, a Bluetooth-enabled readout unit, and a commercial battery, demonstrating low-power, autonomous operation. The data are transmitted in real time to a mobile interface (Fig. 19c), where users can monitor $NO_2$ concentrations *via* a dedicated smartphone app. As illustrated in Fig. 19d, the sensor's transparent and room-temperature operable nature enables a wide range of applications, including environmental monitoring (both outdoor and indoor), smart windows, and even exhaled breath analysis. It enhances the adaptability of MS-based sensors for IoT-oriented platforms.[92]

Complementing this strategy, another study utilized Ru–CuO NFs coated with a ZIF-71 membrane for selective $H_2S$ detection (Fig. 19e and f).[205] The Ru–CuO interface forms a typical Schottky junction, wherein Ru serves as a catalytic site for $H_2S$ oxidation, while the interface modulates charge transport across the p-type CuO NF. The ZIF-71 layer acts as a molecular sieve, selectively permitting small gas molecules, such as $H_2S$ (kinetic diameter $\sim$3.6 Å), while excluding larger VOCs, such as benzene or acetone. This dual-functional architecture, which combines interfacial electronic modulation and physical sieving, yields enhanced sensitivity (down to 100 ppb), excellent gas selectivity, and stable operation under varying humidity conditions.

Together, these two examples underscore the versatility and effectiveness of MS junction engineering in gas sensor design. Whether by harnessing LSPR-assisted photoactivation or Schottky barrier modulation, metal–semiconductor interfaces provide a foundational mechanism for amplifying gas–solid interactions. When further integrated with structural patterning, wireless modules, and functional membranes, they enable the creation of next-generation sensors that are not only sensitive and selective but also portable, transparent, and IoT-compatible.

**5.2.2. Semiconductor–semiconductor heterojunctions.** While MS interfaces have demonstrated remarkable performance in gas sensing through Schottky barrier modulation and plasmonic activation, their reliance on noble metals may limit their long-term stability, cost efficiency, and selectivity in complex environments. As a complementary strategy, SS heterojunctions, particularly those formed between two metal oxides or chalcogenides, have attracted increasing attention for their tunable band alignments, flexibility in defect engineering, and all-inorganic compatibility. By creating a built-in electric field at the heterointerface, SS junctions facilitate directional charge transfer, promote efficient carrier separation, and modulate surface adsorption energetics in response to gas exposure.

A representative implementation of this concept is illustrated in Fig. 20a and b, where Zhan *et al.* developed a self-powered, moisture-triggered gas sensing system based on ES lignin-ZnO NFs doped with $CaCl_2$.[34] The fabrication strategy leverages ES to generate a porous ZnO fiber network incorporating $Ca^{2+}$ ions, which forms an *in situ* SS heterojunction under ambient moisture *via* ion migration and phase separation. This hybrid generator–sensor system converts humidity gradients into voltage signals, enabling the real-time detection of breathing patterns and motion-induced air perturbations without external power. As shown in Fig. 20b, the device effectively distinguishes between resting, exercise, and breathing states, showcasing its potential for wearable respiratory diagnostics. The SS interface between ZnO and $CaCl_2$-induced subphases (*e.g.*, $Zn(OH)_2$ or hydrated $Zn^{2+}$ complexes) is crucial for modulating ionic–electronic coupling, enabling moisture-resolved voltage readouts.

Further extending the SS strategy to flexible, high-temperature gas sensing, Liu *et al.* constructed an all-inorganic, self-supporting $SnO_2$–$SnS_2$–$SiO_2$ NF membrane *via* a layer-by-layer ES approach (Fig. 20c). The membrane consists of a $SiO_2$ NF scaffold onto which $SnO_2$–$SnS_2$ heteroNFs are sequentially deposited, forming extensive p–n heterojunction networks. Digital photographs of the all-inorganic $SnO_2$–$SnS_2$–$SiO_2$ membrane under various bending states (Fig. 20d), illustrating its excellent mechanical flexibility and self-supporting capability.

In addition to structural breathability and mechanical compliance, the device exhibits high and tunable responses to low-concentration $NO_2$ (as low as 100 ppb), with optimal performance at 400 °C, as shown in Fig. 20e. Notably, the sensor maintains its response across various bending states, indicating robust structural-electronic coupling under deformation (Fig. 20f). The heterojunction improves the sensor's intrinsic response and imparts mechanical resilience and operational stability under wearable or complex environmental conditions.[206]

Collectively, these two case studies demonstrate how SS heterojunctions offer a powerful design avenue distinct from MS interfaces. Without relying on noble metals, SS-based NFs allow precise band engineering, abundant junction formation, and tunable interfacial states *via* thermal or ionic modulation. When embedded into flexible, breathable, or moisture-responsive architectures, these heterostructures enable next-generation gas sensors that are energy-efficient, deformable, and environmentally interactive. This not only broadens the material design landscape beyond traditional MS platforms but also sets the stage for multifunctional sensing systems integrating energy harvesting, physiological monitoring, and spatial selectivity, thereby logically bridging the discussion toward multifunctional electronic systems in the next section.

### 5.3. Triboelectric generators

TENGs have become a pivotal component in advancing self-powered electronic systems, particularly for wearable and bio-integrated devices. However, conventional TENG fabrication

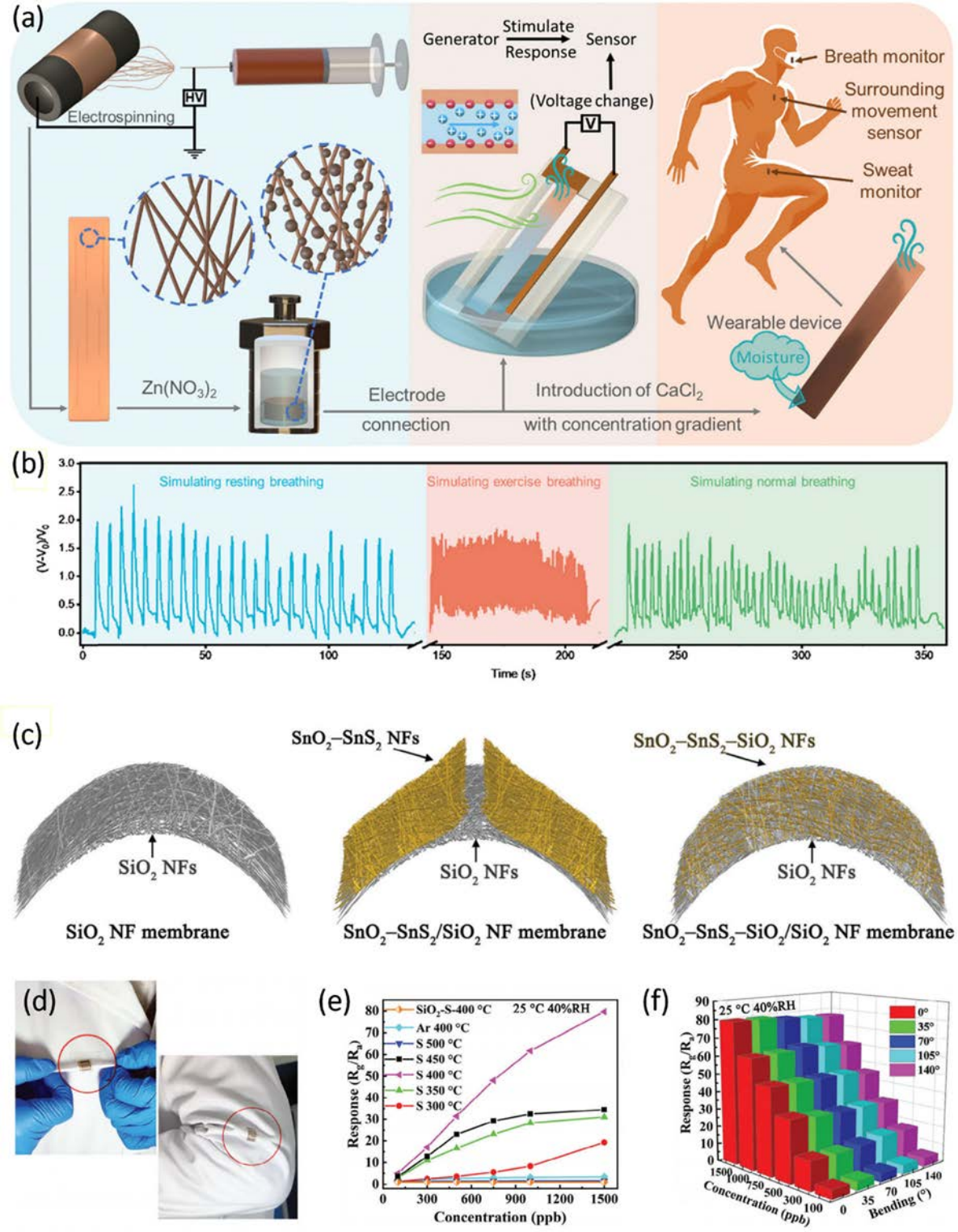


Fig. 20 Semiconductor-semiconductor heterojunction NFs for self-powered moisture and gas sensing. (a) Fabrication process and self-powered sensing mechanism of the LP–ZnO–$CaCl_2$ fiber-based moisture-responsive device. (b) Real-time respiratory monitoring *via* the LP–ZnO–$CaCl_2$ device under different breathing states.[34] Reproduced with permission from ref. 34. Copyright 2025, John Wiley and Sons. (c) Schematic depiction, (d) photographs, (e) dynamic $NO_2$ sensing, and (f) bending tests of multi-layered $SnO_2$–$SnS_2$–$SiO_2$ heteroNF membrane devices.[206] Reproduced with permission from ref. 206. Copyright 2024, John Wiley and Sons.

methods often face trade-offs among mechanical flexibility, energy conversion efficiency, and structural scalability.[207–209] In this regard, ES has emerged as a uniquely powerful technique, offering nanoscale control over fiber morphology, material composition, and device architecture. By engineering NF mats with enhanced surface area, optimized dielectric properties, and hierarchical porosity, ES enables friction layers with significantly improved charge generation and harvesting efficiency. Furthermore, the intrinsic breathability, conformability, and integrability of ES NF membranes make them ideally suited for textile-based, skin-interfaced, and deformable TENG platforms.[210,211] This section highlights recent advances in ES-based TENGs, with a particular focus on all-organic architectures, functional composite strategies, and integrated systems that bridge energy harvesting and real-time sensing.

**5.3.1. Hybrid TENGs.** One of the persistent challenges in developing wearable TENGs lies in reconciling high electrical output with mechanical durability and user comfort. Organic–inorganic hybrid strategies based on the ES have emerged as a powerful means to bridge this gap, enabling the simultaneous optimization of triboelectric performance, structural order, and mechanical robustness.

In a representative example (Fig. 21a), Zhi *et al.* engineered a core–shell NF structure by incorporating lead-free perovskite nanocrystals $Cs_2InCl_5(H_2O)$ into PVDF-HFP *via* a one-step ES-assisted self-assembly strategy. The resulting $Cs_2InCl_5(H_2O)$@PVDF-HFP (CIC@HFP) NFs exhibited aligned dipolar configurations and enriched β-phase content. These ordered dipoles, oriented along the fiber axis, facilitated efficient charge separation and retention during triboelectrification, substantially enhancing output performance. The enhanced output originates from cooperative dipole alignment and interfacial polarization induced by the perovskite–polymer hybrid structure, suggesting that electrospinning can simultaneously control molecular orientation and nanoscale polarization centers. The mechanism underlying this enhancement is illustrated in Fig. 21b. During cyclic contact and release with a positively charged nylon-6,6 layer, the well-polarized CIC@HFP NFs generated pronounced surface potential differences and electron flow, enabling continuous AC output. As shown in Fig. 21c, KPFM analysis further confirmed that the highest surface potential occurred at the optimal perovskite loading of 1.5 wt%, directly correlating with a maximum electroactive β-phase fraction of 81.25%.[80] This finding highlights the importance of fine-tuning the hybrid composition to optimize dipolar polarization and triboelectric charge density.

In another strategy that combines functionality and wearability, Chen *et al.* developed a multiscale three-layer hybrid yarn structure using ES-PA11/ZnO NFs as an intermediate layer and polyester fibers as the outer sheath (Fig. 21d).[96] This nano-microstructured yarn not only enhanced charge capture by leveraging ZnO-induced deep trap states but also demonstrated exceptional abrasion resistance, water repellency, and air permeability. These mechanical and comfort-related properties are critical for real-world deployment in textiles and on-skin electronics. In both systems, the ES process played a pivotal role by enabling uniaxial molecular alignment and phase control, which are essential for enhancing the electroactive performance of PVDF-based materials. The synergistic interface engineering between organic polymers and functional inorganic fillers provides a robust pathway for performance optimization, whether through hydrogen bonding, charge trapping, or energy-level alignment.

Overall, organic–inorganic hybridization *via* ES not only enhances triboelectric output through molecular and interfacial polarization mechanisms but also offers the structural tunability needed for wearable, biocompatible, and mechanically stable devices. These advances represent a significant step toward scalable, high-performance TENGs that are suitable for integration into next-generation self-powered wearable systems.

**5.3.2. All-organic TENGs.** As flexible electronics advance toward fully integrated, sustainable, and body-compatible systems, TENGs have emerged as a core technology for self-powered wearable sensing. In particular, all-organic TENGs fabricated *via* ES avoid rigid inorganic electrodes and brittle dielectric layers, enabling intrinsic mechanical softness, air permeability, and skin conformity. Beyond material compatibility, the structural tunability of electrospun fibrous mats plays a decisive role in charge generation and mechanical-to-electrical energy conversion, where fiber diameter (hundreds of nanometers), porosity, and surface polarization jointly determine the achievable surface charge density and output stability.

In a representative textile-integrated system reported by Qi *et al.*, a permeable all-organic TENG (pTENG) was constructed using a liquid-metal-embedded PVDF-TrFE electrospun fiber mat as the negative triboelectric layer and Ni-coated fabric as the counter electrode (Fig. 22a).[212] The incorporation of uniformly dispersed liquid–metal nanoparticles effectively increases the dielectric constant of the fibrous membrane, thereby strengthening interfacial charge storage and suppressing charge dissipation during repeated contact–separation processes. As a result, the device exhibits enhanced electrical output, including a high normalized open-circuit voltage and efficient charge transfer capability. More importantly, this dielectric modulation strategy demonstrates that nanoscale filler engineering can be utilized to regulate polarization behavior in electrospun polymer networks.

Beyond electrical performance, the hierarchical porous structure of the fiber mat provides high air and moisture permeability, ensuring mechanical softness and long-term wear comfort comparable to that of commercial textiles. When integrated with an energy management module, the pTENG enables efficient energy storage and delivery, allowing stable operation of wireless sensing systems under human motion, as illustrated in Fig. 22b. These results indicate that rational coupling of dielectric enhancement and breathable fibrous architectures is essential for realizing practical, self-powered wearable platforms.

Complementarily, Deng *et al.* developed a fully organic contact–separation TENG based on electrospun PVDF-TrFE/PMMA blended NFs and duplicating paper as the triboelectric pair (Fig. 22c). By introducing 15 wt% PMMA into the PVDF-TrFE matrix, hydrogen bonding interactions promote β-phase formation and simultaneously reinforce the mechanical integrity of the fibrous membrane. This molecular-level regulation

 

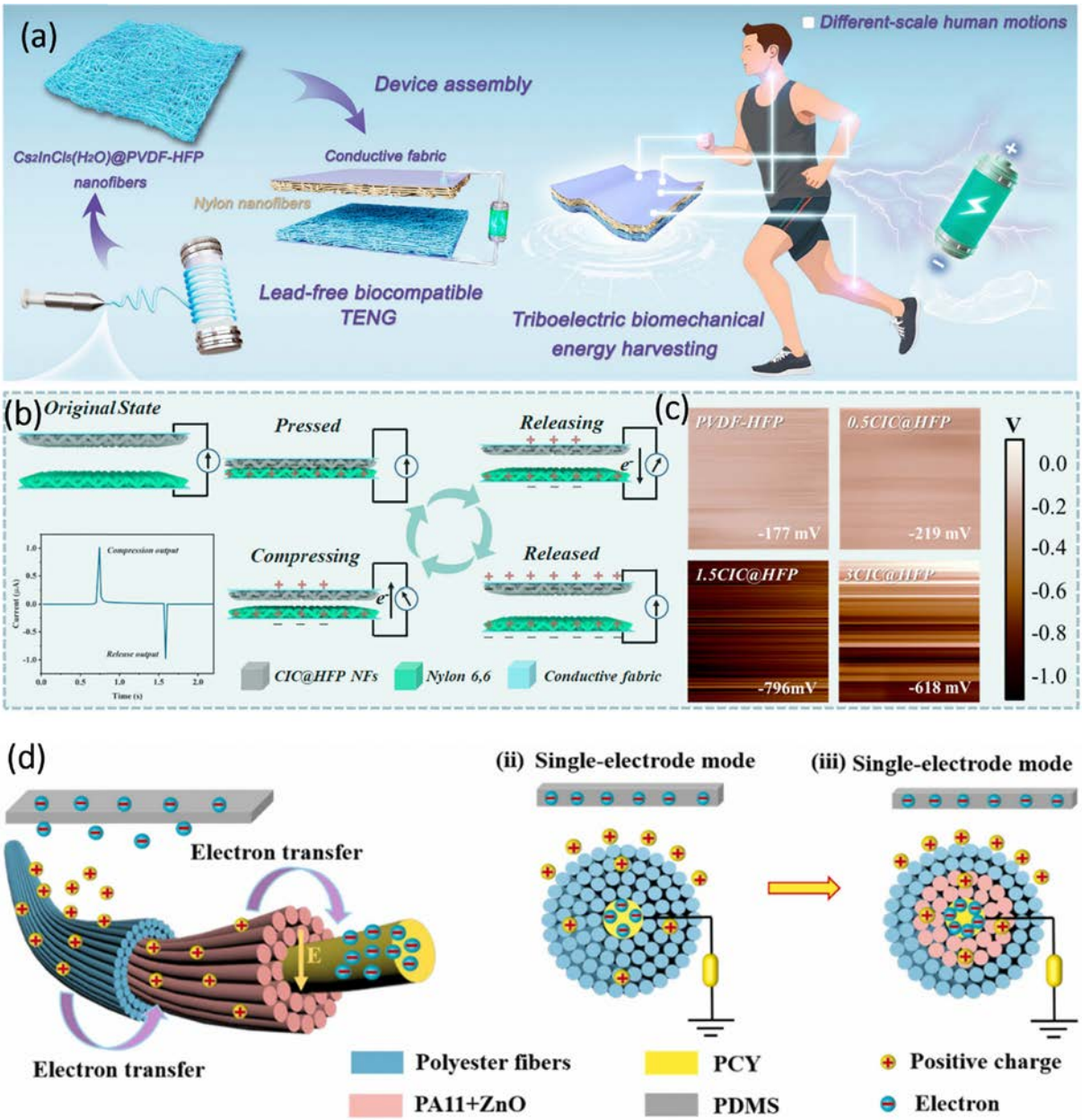


Fig. 21 Hybrid triboelectric NFs-based nanogenerators with engineered charge transport. (a) Schematic of a CIC@HFP-based TENG constructed from ES $Cs_2InCl_5(H_2O)$@PVDF-HFP core–shell NFs and nylon-6,6 NFs. (b) Working principle of the CIC@HFP TENG under periodic contact-separation cycles, supported by (c) surface potential mappings measured *via* KPFM.[80] Reproduced with permission from ref. 80. Copyright 2024, American Chemical Society. (d) Charge transport mechanism of ZnO/PA11-polyer yarn-based TENGs.[96] Reproduced with permission from ref. 96. Copyright 2022, Elsevier.

enhances dipolar polarization and mechanical durability, resulting in improved, stable electrical output under cyclic deformation.

Under optimized working conditions, the all-organic TA-TENG exhibits reliable voltage generation and current output, as shown in Fig. 22d, together with excellent operational stability over extended cycling.[97] The multilayer porous microfiber network not only increased the effective contact area but also enabled efficient moisture exchange, which is essential for skin-contact operation. From a structural–functional perspective, these results clearly indicate that electrospun all-organic TENGs can simultaneously achieve high voltage output ($>30$ V cm$^{-2}$), breathable textile-level permeability, and long-term cyclic stability ($>10^4$–$10^5$ cycles). The combination of high β-phase polarization in PVDF-based fibers, dielectric enhancement *via* polymer blending, or nanoparticle incorporation, and hierarchical porous fibrous architectures provides a robust material–structure–performance platform for overcoming the traditionally low power density of textile-based TENGs.

Overall, electrospun all-organic TENGs enable a unique integration of mechanically adaptive deformation, efficient low-frequency energy harvesting, and wireless sensing functionality within a single breathable platform. Their intrinsic

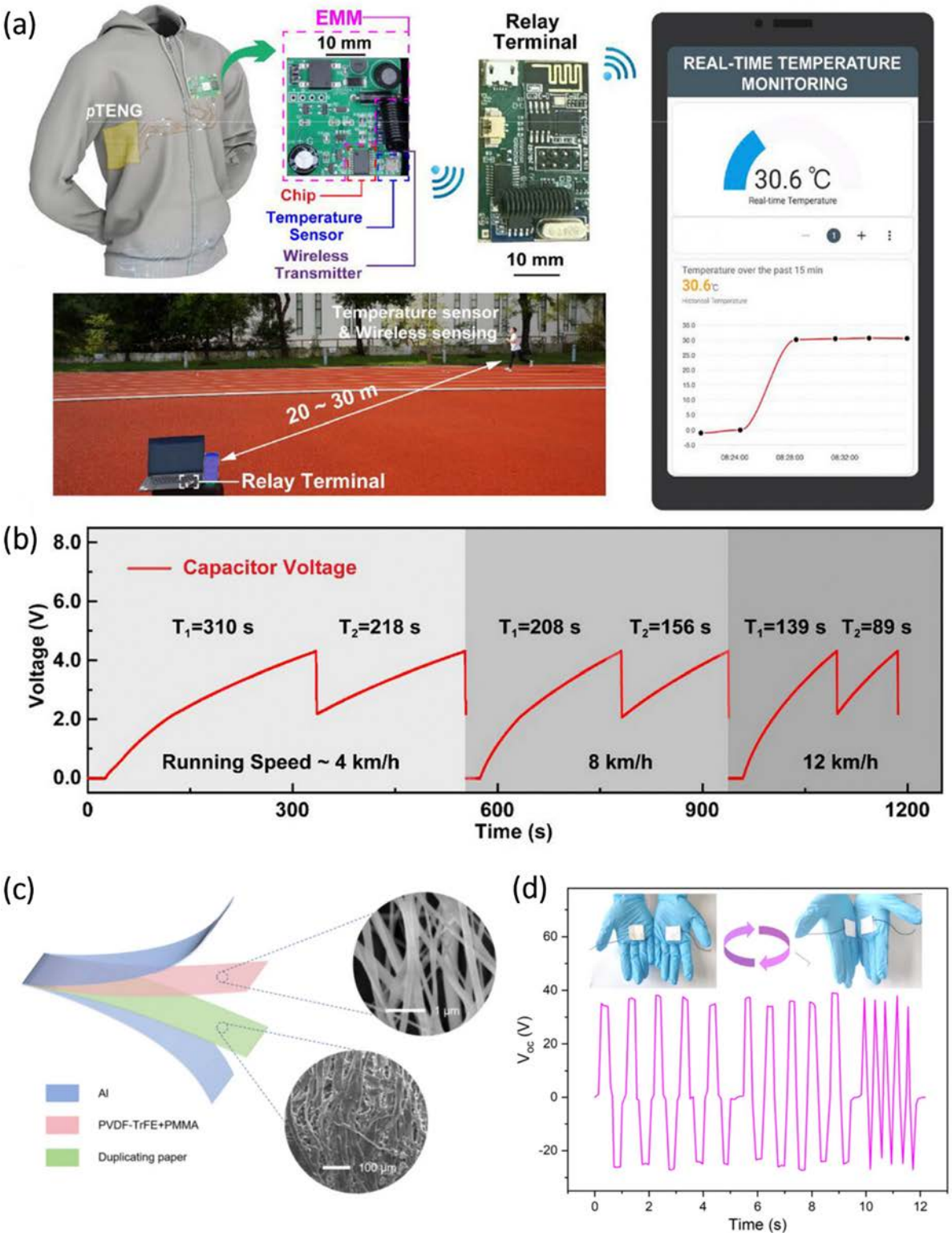


Fig. 22 All-organic triboelectric NFs-based nanogenerators. (a) Schematic and photograph of a wearable self-powered temperature sensing system based on an ES TENG. (b) Capacitor voltage generated by the ES-based TENG while running at different speeds.[212] Reproduced with permission from ref. 212. Copyright 2025, John Wiley and Sons. (c) Structural diagram with SEM images, and (d) output voltage signals of an organic TENG composed of PVDF-TrFE-PMMA NFs layered between duplicating paper and Al electrodes.[97] Reproduced with permission from ref. 97. Copyright 2024, Springer Nature.

softness, lightweight nature, and scalable manufacturability position them as key building blocks for next-generation textile electronics, continuous health monitoring, sports analytics, and body area networks, bridging the gap between triboelectric energy harvesting and multifunctional intelligent wearable systems.

# 6. Conclusion and outlook

ES has proven to be a powerful and adaptable platform for fabricating 1D nanomaterials tailored for next-generation optoelectronic and electronic applications.[17,213,214] Through rational design of solution composition, process parameters, and collector configuration, ES enables precise control over NF morphology, composition, and spatial arrangement across multiple length scales. These capabilities underpin the successful integration of ES NFs into a broad range of high-performance devices, including photodetectors, field-effect transistors, triboelectric nanogenerators, gas sensors, and neuromorphic systems.

The application scenarios discussed in this review demonstrate how ES can transcend its traditional role as a fabrication method and evolve into a design strategy for hierarchical device engineering. Microscale heterostructures, such as core–shell fibers, and macroscale architectures, including network arrays or parallel fiber arrangements, offer unprecedented opportunities to tailor interfacial charge transport, light–matter interactions, and environmental responsiveness. In particular, the capacity to combine diverse material systems (organic/inorganic, dielectric/conductive, and semiconducting/triboelectric) within a unified ES framework enables cross-functional integration and novel hybrid functionalities.

Despite remarkable progress in developing ES NFs for electronic and optoelectronic applications, several promising directions remain to be explored to bridge the gap between material innovation and practical application, as outlined in the following.

### 6.1. Advancing low-temperature ES for broader application scenarios

Traditional ES processes often require post-treatment at elevated temperatures to remove polymer templates or to induce crystallinity in inorganic components. However, such high-temperature steps limit substrate selection and compatibility with flexible, temperature-sensitive platforms. The development of low-temperature ES strategies, including those that utilize UV photoactivation, plasma treatment, or solution-based crystallization, has great potential to broaden the applicability of ES fibers. This is particularly important for integration with plastic electronics, soft robotics, and biological interfaces. Future research should focus on optimizing solvent systems, polymer composites, crosslinking chemistries, and low-temperature post-treatment processes to enable ultralow-thermal-budget fabrication of NFs.

### 6.2. Toward scalable integration of ES NF devices

While individual ES fibers have demonstrated attractive performance at the proof-of-concept stage, the transition to large-scale integration remains a significant bottleneck. Challenges include the alignment, density control, and patterning of NFs over wafer-scale substrates. Emerging approaches such as near-field ES, mask-guided deposition, and programmable 3D collectors offer promising tools for addressing these issues. Moreover, integrating multi-material fibers into device arrays with consistent performance is critical for real-world applications such as sensor networks and neuromorphic circuits. Future research should prioritize the co-development of fiber processing techniques and microfabrication-compatible architectures to enable wafer-level manufacturability.

### 6.3. Merging ES NFs with stretchable and wearable electronics

The inherent flexibility and high aspect ratio of ES NFs make them ideal candidates for stretchable and wearable electronics. However, further efforts are needed to achieve mechanical resilience under repeated deformation while maintaining stable electrical and optical performance. Strategies such as embedding fibers into elastomeric matrices, engineering serpentine or mesh layouts, and introducing self-healing functionalities could significantly enhance device longevity. Moreover, combining ES NFs with emerging materials, such as liquid metals, conductive hydrogels, and textile-based platforms, may enable next-generation wearables with conformal and multimodal sensing capabilities. Exploring these interdisciplinary opportunities will be vital to expanding ES's role in the Internet of Things and personalized healthcare.

### 6.4. Developing biodegradable and environmentally friendly fiber systems

With growing concerns over electronic waste and environmental sustainability, the design of biodegradable ES fibers has become an urgent and promising direction. Natural polymers such as cellulose, chitosan, silk fibroin, and polylactic acid (PLA) offer attractive options for eco-friendly fiber fabrication. These materials reduce environmental burden and open new possibilities for transient electronics, implantable devices, and bioresorbable sensors. However, achieving performance parity with synthetic counterparts remains a challenge. Future efforts should aim to balance degradability, mechanical strength, and functional stability through composite design, crosslinking strategies, and the use of bio-derived additives.

In summary, ES technology is poised for a transformative phase where functionality should be matched by integrability, scalability, and sustainability. By shifting from single-fiber performance metrics to system-level thinking, the ES community can unlock its full potential in shaping the next generation of intelligent, flexible, and eco-conscious electronics.

# Author contributions

Shuwen Xin led the literature survey, organized the review's structure, integrated figures and tables, and drafted and revised the manuscript. You Meng conceptualized the review scope,

supervised the overall framework, and revised the manuscript. Li Ni performed reference organization, assisted in organizing representative studies, and contributed to figure preparation. Aolin Wang assisted in section writing and helped refine discussions. Jinwei Pu assisted in summarizing device applications and contributed to section writing. Siyuan Wu contributed to data summarization and assisted in manuscript polishing. Xin Peng contributed to section writing and cross-checking technical descriptions. Yujin Liu assisted with sorting device metrics, verified citation accuracy, and contributed to writing. Kun Tang supported manuscript organization and contributed to refining the language. Zhengxun Lai assisted with survey work, validated technological classifications, and contributed to figure preparation. He Shao supervised the conceptual direction, guided manuscript organization, and wrote the manuscript. Johnny C. Ho provided guidance, ensured academic coherence, evaluated all sections, and finalized the manuscript. All authors discussed the content and approved the final version of the manuscript.

## Conflicts of interest

There are no conflicts to declare.

## Data availability

No primary research results, software or code have been included, and no new data were generated or analyzed as part of this review.

## Acknowledgements

This work was supported by the Open Fund of State Key Laboratory of Infrared Physics (Grant No. SITP-SKLIP-ZD-2025-08), the National Natural Science Foundation of China (Grant No. 62574077 and 62504079), the "111 Center" (B25033), and the Research Grant Councils of the Hong Kong SAR (CityU 11208923).

## References

1 S. T. Ha, Q. T. Li, J. K. W. Yang, H. V. Demir, M. L. Brongersma and A. I. Kuznetsov, *Science*, 2024, **386**, eadm7442.
2 K. Mahato, T. Saha, S. C. Ding, S. S. Sandhu, A. Y. Chang and J. S. Wang, *Nat. Electron.*, 2024, **7**, 735–750.
3 X. Q. Cui, F. Nigmatulin, L. Wang, I. Reduto, A. C. Liapis, M. D. Du, M. G. Uddin, S. A. Mayeen, F. Ahmed, Y. Zhang, H. H. Yoon, H. Lipsanen, S. Honkanen, T. Aalto, Z. Y. Yang, T. Hasan, W. W. Cai and Z. P. Sun, *Sci. Adv.*, 2025, **11**, eado6886.
4 H. Kim, D. Kim, J. Kim, Y. Lee, M. Shin, J. Kim, F. M. Bossuyt, G. H. Lee, B. Lee, W. R. Taylor and J. Lee, *Npj Flexible Electron.*, 2025, **9**, 84.
5 Y. M. Zhang, E. Rytkin, L. S. Zeng, J. U. Kim, L. C. Tang, H. H. Zhang, A. Mikhailov, K. Y. Zhao, Y. Wang, L. Ding, X. Y. Lu, A. Lantsova, E. Aprea, G. M. Jiang, S. P. Li, S. G. Seo, T. Wang, J. Wang, J. Y. Liu, J. Y. Gu, F. Liu, K. Bailey, Y. F. L. Li, A. Burrell, A. Pfenniger, A. Ardashev, T. Y. Yang, N. J. Liu, Z. Y. Lv, N. S. Purwanto, Y. Ying, Y. S. Lu, C. Hoepfner, A. Melisova, J. R. Gong, J. Jeong, J. Choi, A. L. Hou, R. Nolander, W. B. Bai, S. H. Jin, Z. Q. Ma, J. M. Torkelson, Y. G. Huang, W. Ouyang, R. K. Arora, I. R. Efimov and J. A. Rogers, *Nature*, 2025, **640**, 77–86.
6 Z. Z. Wu, D. Adekoya, X. Huang, M. J. Kiefel, J. Xie, W. Xu, Q. C. Zhang, D. B. Zhu and S. Q. Zhang, *ACS Nano*, 2020, **14**, 12016–12026.
7 S. H. Yu, X. Y. Liu, H. L. Dong, X. H. Wang and L. X. Li, *Ceram. Int.*, 2021, **47**, 20379–20386.
8 M. Ding, D. Ji and W. Hu, *FlexMat*, 2025, **2**, 510–532.
9 W. K. Shen, P. Wang, G. D. Wei, S. Yuan, M. Chen, Y. Su, B. S. Xu and G. Q. Li, *Small*, 2024, **20**, 2400458.
10 J. Song, X. Y. Cui, P. Liu, Y. H. Shi, X. J. Wang, M. Li, Y. Y. Zhou, J. Yang, H. R. Liu, Y. Yan, C. X. Xia and R. P. Qin, *Chem. Eng. J.*, 2024, **486**, 150378.
11 B. B. Wei, B. Q. Zou, J. X. Liu, W. H. Wang, W. Q. Wang, Z. Y. Cao, T. Han, F. Li, W. Luo, L. Shan and M. S. Long, *Adv. Funct. Mater.*, 2024, **34**, 2315194.
12 J. M. Yang, L. Chang, X. Q. Zhang, Z. Q. Cao and L. Jiang, *Nano-Micro Lett.*, 2024, **16**, 140.
13 M. Long, G. M. Wu, F. H. Tao, S. Ma, X. Y. Dong and H. B. Deng, *Int. J. Biol. Macromol.*, 2024, **278**, 134372.
14 Y. Jang, S. Roh, Y. Cho, Y. Jung, K. Lee, N. Choi, J. Yoo and H. Seong, *Adv. Fiber Mater.*, 2024, **6**, 1583–1595.
15 E. Abdelhakeem, S. Monir, M. H. M. Teaima, K. O. Rashwan and M. El-Nabarawi, *AAPS PharmSciTech*, 2023, **24**, 246.
16 F. Fadil, N. D. N. Affandi, M. I. Misnon, N. N. Bonnia, A. M. Harun and M. K. Alam, *Polymers*, 2021, **13**, 2087.
17 F. Guo, Z. Ren, S. C. Wang, Y. Xie, J. L. Pan, J. Y. Huang, T. X. Zhu, S. Cheng and Y. K. Lai, *Nano-Micro Lett.*, 2025, **17**, 302.
18 B. He, G. He, C. Fu, S. S. Jiang, E. Fortunato, R. Martins and S. G. Wang, *Adv. Funct. Mater.*, 2024, **34**, 2316375.
19 L. Veeramuthu, C. J. Cho, M. Venkatesan, G. R. Kumar, H. Y. Hsu, B. X. Zhuo, L. J. Kau, M. A. Chung, W. Y. Lee and C. C. Kuo, *Nano Energy*, 2022, **101**, 107592.
20 Z. Y. Zhou, W. R. Tang, T. R. Xu, W. Y. Zhao, J. J. Zhang and C. W. Bai, *Sensors*, 2024, **24**, 4793.
21 X. F. Lu, C. Wang and Y. Wei, *Small*, 2009, **5**, 2349–2370.
22 H. S. Wang, G. D. Fu and X. S. Li, *Recent Pat. Nanotechnol*, 2009, **3**, 21–31.
23 D. Ji, Y. Lin, X. Guo, B. Ramasubramanian, R. Wang, N. Radacsi, R. Jose, X. Qin and S. Ramakrishna, *Nat. Rev. Methods Primers*, 2024, **4**, 1.
24 Y. Wang, T. Yokota and T. Someya, *NPG Asia Mater.*, 2021, **13**, 22.
25 G. Chen, H. Cong, Y. Chang, Y. Zhang, R. Zhou, Y. Wang, Y. Qin, X. Liu and F. Wang, *Sci. China Mater.*, 2023, **66**, 4445–4452.
26 H. Maleki, R. S. Rahbar, S. Azimi, T. Schneiders, C. Emonts and T. Gries, *Fiber. Polym.*, 2025, **26**, 607–619.
27 R. Shekarian, D. Semnani, S. N. Khorasani and M. Atai, *Polym. Adv. Technol.*, 2025, **36**, e70122.

 

28 S. Taokaew and T. Chuenkaek, *Fibers*, 2024, **12**, 26.
29 G. Park, M. Choi, H. J. Choi, Y. S. Shim, S. J. Kim, J. O. Lee and D. Cho, *ACS Appl. Nano Mater.*, 2025, **8**, 10704–10716.
30 J. Liu, J. Zhang, Q. Yu, Y. Liu, X. Zhang, G. Zhu, Y. Jia, H. Lu, J. Gao, H. Wang and B. Zhu, *Adv. Funct. Mater.*, 2024, **35**, 2410833.
31 M. W. Kim, Y. Yuan, S. Jeong, J. Chong, H. Mølnås, A. Alaei, I. J. Cleveland, N. Liu, Y. Ma, S. Strauf, E. S. Aydil, A. Sahu, D. M. Kalyon and S. S. Lee, *Adv. Funct. Mater.*, 2022, **32**, 2207326.
32 Z. F. Liu, R. Wang, J. N. Han, T. H. Chen, Z. C. Deng, Y. L. Sun, Y. B. Zhao and A. H. Chen, *Adv. Funct. Mater.*, 2025, **35**, 2424645.
33 Z. Zheng, L. Gan, J. B. Zhang, F. W. Zhuge and T. Y. Zhai, *Adv. Sci.*, 2017, **4**, 1976–1987.
34 Y. F. Zhan, J. Poisson, X. T. Meng, Z. B. Wang, L. Z. Chen, T. H. Wu, R. Koehler and K. Zhang, *Adv. Mater.*, 2025, **37**, 2502211.
35 Y. Guo, F. Wu, G. H. Dun, T. Cui, Y. Liu, X. Tan, Y. Qiao, M. Lanza, H. Tian, Y. Yang and T. L. Ren, *Adv. Funct. Mater.*, 2022, **33**, 2208055.
36 D. Liu, Q. Shi, S. Dai and J. Huang, *Small*, 2020, **16**, e1907472.
37 K. A. Rokade, D. D. Kumbhar, S. L. Patil, S. S. Sutar, K. V. More, P. B. Dandge, R. K. Kamat and T. D. Dongale, *Adv. Mater.*, 2024, **36**, e2312484.
38 J. Xue, T. Wu, Y. Dai and Y. Xia, *Chem. Rev.*, 2019, **119**, 5298–5415.
39 L. Georgescu, *Stud. Hist. Philos. Sci. A*, 2014, **47**, 18–25.
40 C. V. Boys, *Proc. Phys. Soc., London*, 1887, **9**, 8.
41 J. F. Cooley, *US Pat.*, 692.631, United States Patent and Trademark Office, 1902.
42 J. Zeleny, *Phys. Rev.*, 1914, **3**, 69–91.
43 J. Zeleny, *Phys. Rev.*, 1917, **10**, 1–6.
44 N. Tucker, J. J. Stanger, M. P. Staiger, H. Razzaq and K. Hofman, *J. Eng. Fibers Fabr.*, 2012, **7**, 63–73.
45 Q. Gao, S. Agarwal, A. Greiner and T. Zhang, *Prog. Mater. Sci.*, 2023, **137**, 101139.
46 R. Jaeger, M. M. Bergshoef, C. M. I. Batlle, H. Schonherr and G. J. Vancso, *Macromol. Symp.*, 1998, **127**, 141–150.
47 D. LeCorre-Bordes, N. Tucker, T. Huber, N. Buunk and M. P. Staiger, *J. Mater. Sci.*, 2016, **51**, 6686–6696.
48 W. Q. Wang, W. L. Li and R. F. Zhang, *J. Polym. Mater.*, 2010, **27**, 293–302.
49 Y. Aykut, C. D. Saquing, B. Pourdeyhimi, G. N. Parsons and S. A. Khan, *ACS Appl. Mater. Interfaces*, 2012, **4**, 3837–3845.
50 J. X. Chen, Y. R. Wang, Y. F. Liu, Y. Tan, J. Zhang, P. B. Liu and J. Kong, *Carbon*, 2023, **208**, 82–91.
51 W. B. Deng, Y. Liu, C. He, X. Z. Xiong, R. Zhang, T. F. Yan, S. C. Shi, D. G. Yu and H. S. Yang, *Chem. Eng. J.*, 2025, **506**, 160117.
52 X. Y. He, J. T. Gu, Y. N. Hao, M. R. Zheng, L. M. Wang, J. Y. Yu and X. H. Qin, *Chem. Eng. J.*, 2022, **450**, 137937.
53 Y. Huang, C. F. Xiao, Q. L. Huang, H. L. Liu and J. Zhao, *Chem. Eng. J.*, 2021, **403**, 126295.
54 B. Pant, M. Park and S. J. Park, *Pharmaceutics*, 2019, **11**, 305.
55 H. Yin, D. Y. Han, X. X. Yu, M. L. Cao, Z. H. Hou, C. Li and M. Q. Zhu, *ACS Appl. Energy Mater.*, 2023, **6**, 1155–1175.
56 R. Abdulhussain, A. Adebisi, B. R. Conway and K. Asare-Addo, *J. Drug Delivery Sci. Technol.*, 2023, **90**, 105156.
57 D. Han and A. J. Steckl, *ChemPlusChem*, 2019, **84**, 1453–1497.
58 J. Avossa, G. Herwig, C. Toncelli, F. Itel and R. M. Rossi, *Green Chem.*, 2022, **24**, 2347–2375.
59 Y. J. Chen, X. T. Dong, M. Shafiq, G. Myles, N. Radacsi and X. M. Mo, *Adv. Fiber Mater.*, 2022, **4**, 959–986.
60 Y. B. Dou, W. J. Zhang and A. Kaiser, *Adv. Sci.*, 2020, **7**, 1902590.
61 I. Jun, H. S. Han, J. R. Edwards and H. Jeon, *Int. J. Mol. Sci.*, 2018, **19**, 745.
62 T. T. Min, L. P. Zhou, X. L. Sun, H. Y. Du, Z. Zhu and Y. Q. Wen, *Food Chem.*, 2022, **391**, 133239.
63 A. Nadaf, A. Gupta, N. Hasan, Fauziya, S. Ahmad, P. Kesharwani and F. J. Ahmad, *RSC Adv.*, 2022, **12**, 23808–23828.
64 J. Chen, Z. S. Shao, C. H. Ru and Z. Yang, *Presented in part at the International Conference on Manipulation, Manufacturing and Measurement on the Nanoscale (3M-Nano)*, Suzhou, People's Republic of China, 2013.
65 H. Wang, Y. L. Bao, X. D. Yang, X. Z. Lan, J. Guo, Y. L. Pan, W. M. Huang, L. J. Tang, Z. F. Luo, B. Zhou, J. S. Yao and X. Chen, *Polymers*, 2022, **14**, 3294.
66 T. Z. Zhou, *Scalable Manufacture of Nanofibers via Near-Field Electrospinning*, 2018.
67 R. Sugimoto, J. H. Lee, J. H. Lee, H. E. Jin, S. Y. Yoo and S. W. Lee, *RSC Adv.*, 2019, **9**, 39111–39118.
68 H. Cho, S. Y. Min and T. W. Lee, *Macromol. Mater. Eng.*, 2013, **298**, 475–486.
69 C. Drew, X. Wang, K. Senecal, H. Schreuder-Gibson and L. Samuelson, *Presented in part at the Antec: Society of Plastics Engineers Technical Papers, Conference Proceedings, VOLS I-III*, Orlando, Florida, 2000.
70 J. L. Skinner, J. M. Andriolo, J. D. Beisel, B. M. Ross, L. M. Purkett, J. P. Murphy, J. Kyerematen, M. J. Franson, E. A. Kooistra-Manning, B. E. Hill and B. R. Loyola, *Presented in part at the Low-Dimensional Materials and Devices*, San Diego, California, 2015.
71 J. W. Yang, H. H. Wei, B. He, S. S. Jiang, B. Y. Wang, C. Fu and G. He, *ACS Appl. Electron. Mater.*, 2025, **7**, 7184–7194.
72 J. Xue, J. Xie, W. Liu and Y. Xia, *Acc. Chem. Res.*, 2017, **50**, 1976–1987.
73 H. R. Pant, B. Pant, P. Pokharel, H. J. Kim, L. D. Tijing, C. H. Park, D. S. Lee, H. Y. Kim and C. S. Kim, *J. Membr. Sci.*, 2013, **429**, 225–234.
74 D. H. Reneker and A. L. Yarin, *Polymer*, 2008, **49**, 2387–2425.
75 Y. Chang, H. Cong, R. Zhou, W. Zhang, Y. Qin, X. Liu and F. Wang, *ACS Appl. Electron. Mater.*, 2022, **4**, 2570–2579.
76 J. Li, W. Fu, Y. Lei, L. Li, W. Zhu and J. Zhang, *ACS Appl. Mater. Interfaces*, 2022, **14**, 8587–8597.
77 K. H. Zhou, X. Y. Hu, G. Y. Chen, D. D. Xu and X. X. Xu, *ACS Appl. Nano Mater.*, 2024, **8**, 376–383.
78 S. Dong, B. M. Maciejewska, R. M. Schofield, N. Hawkins, C. R. Siviour and N. Grobert, *ACS Nano*, 2024, **18**, 13538–13550.

79 Q. Kang, Z. Zhuang, Y. Liu, Z. Liu, Y. Li, B. Sun, F. Pei, H. Zhu, H. Li, P. Li, Y. Lin, K. Shi, Y. Zhu, J. Chen, C. Shi, Y. Zhao, P. Jiang, Y. Xia, D. Wang and X. Huang, *Adv. Mater.*, 2023, **35**, e2303460.
80 C. W. Zhi, S. Zhang, H. B. Wu, Y. Ming, S. Shi, W. F. Io, S. Meng, Y. F. Si, B. Fei, J. H. Hao and J. L. Hu, *ACS Nano*, 2024, **18**, 9365–9377.
81 W. Zhang, H. Li, H. Cong, R. Zhou, Y. Qin, P. Xu, X. Liu and F. Wang, *Curr. Appl. Phys.*, 2023, **48**, 34–41.
82 S. Veeralingam and S. Badhulika, *Nano Energy*, 2022, **98**, 107354.
83 L. Song, K. Dou, R. Wang, P. Leng, L. Luo, Y. Xi, C.-C. Kaun, N. Han, F. Wang and Y. Chen, *ACS Appl. Mater. Interfaces*, 2019, **12**, 1270–1279.
84 Y. Ning, Z. Zhang, F. Teng and X. Fang, *Small*, 2018, **14**, 1703754.
85 Y. Zhu, B. Shin, G. Liu and F. Shan, *IEEE Electron Device Lett.*, 2019, **40**, 1776–1779.
86 J. Li, S.-K. Wen, D.-L. Jiang, L.-K. Li and J.-H. Zhang, *IEEE Electron Device Lett.*, 2022, **43**, 1653–1656.
87 L. Li, J. Li, Z. Zhang, Z. Wang, S. Wen, Q. Yang and J. Zhang, *ACS Appl. Nano Mater.*, 2023, **6**, 7510–7518.
88 B. He, G. He, Q. Hu, S. Jiang, Q. Gao, E. Fortunato and R. Martins, *Adv. Electron. Mater.*, 2023, **9**, 2300032.
89 B. He, G. He, C. Fu, Q. Hu, P. Chen and S. Wang, *IEEE Trans. Electron Devices*, 2024, **71**, 1308–1312.
90 H. Zu, Y. Chang, H. Li, J. He, J. Li, X. Zhu, J. Zhang and F. Wang, *IEEE Electron Device Lett.*, 2021, **42**, 855–858.
91 B. He, G. He, L. Zhu, J. Cui, E. Fortunato and R. Martins, *Adv. Funct. Mater.*, 2023, **34**, 2310264.
92 K. Lim, Y. M. Jo, J. W. Yoon, J. S. Kim, D. J. Lee, Y. K. Moon, J. W. Yoon, J. H. Kim, H. J. Choi and J. H. Lee, *Small*, 2021, **17**, e2100438.
93 X. Bai, H. Lv, Z. Liu, J. Chen, J. Wang, B. Sun, Y. Zhang, R. Wang and K. Shi, *J. Hazard. Mater.*, 2021, **416**, 125830.
94 H. Shin, D. H. Kim, W. Jung, J. S. Jang, Y. H. Kim, Y. Lee, K. Chang, J. Lee, J. Park, K. Namkoong and I. D. Kim, *ACS Nano*, 2021, **15**, 14207–14217.
95 A. Yin, J. Wang, S. Hu, M. Sun, B. Sun, M. Dong, T. Zhang, Z. Feng, H. Zhang, B. Shi, C. Zhang and H. Liu, *Nano Energy*, 2023, **106**, 108034.
96 W. Chen, W. Fan, Q. Wang, X. Yu, Y. Luo, W. Wang, R. Lei and Y. Li, *Nano Energy*, 2022, **103**, 107769.
97 X. Deng, Z. Wu, X. Yu, M. Wang, D. Zang, Y. Long, N. Guo, L. Weng, Y. Liu and J. Gao, *Adv. Compos. Hybrid Mater.*, 2024, **8**, 19.
98 H. Hu, J. Song, Y. Zhong, J. Cao, L. Han, Z. Zhang, G. Cheng and J. Ding, *ACS Sens.*, 2024, **9**, 2907–2914.
99 H. Zhang, X. Zhang, C. Qiu, P. Jia, F. An, L. Zhou, L. Zhu and D. Zhang, *Chem. Eng. J.*, 2024, **496**, 154226.
100 F. Mokhtari, K. A. S. Usman, J. Zhang, R. Komljenovic, Z. Simon, B. Dharmasiri, A. Rezk, P. C. Sherrell, L. C. Henderson, R. J. Varley and J. M. Razal, *ACS Appl. Mater. Interfaces*, 2025, **17**, 3214–3228.
101 Y. Cho, J. W. Baek, M. Sagong, S. Ahn, J. S. Nam and I. D. Kim, *Adv. Mater.*, 2025, **37**, 2500162.
102 E. Ewaldz, J. Randrup and B. Brettmann, *ACS Polym. Au*, 2022, **2**, 108–117.
103 R. Stepanyan, A. V. Subbotin, L. Cuperus, P. Boonen, M. Dorschu, F. Oosterlinck and M. J. H. Bulters, *Polymer*, 2016, **97**, 428–439.
104 Y. N. Filatov, I. Y. Filatov and M. A. Smul'skaya, *Fibre Chem.*, 2017, **49**, 151–160.
105 L. Vargas-Campos, J. d D. Figueroa-Cárdenas, D. Tochihuitl-Vázquez, R. Ramírez-Bon, J. M. Yáñez-Limón and J. F. Pérez-Robles, *Food Hydrocoll.*, 2023, **139**, 108498.
106 J.-Y. Yin, C. Boaretti, A. Lorenzetti, A. Martucci, M. Roso and M. Modesti, *Nanomaterials*, 2022, **12**, 962.
107 J. Kim, W. Lee, S. Choi, K. T. Kim, J. S. Heo, S. K. Park and Y. H. Kim, *Appl. Surf. Sci.*, 2020, **515**, 145988.
108 A. Laforgue and L. Robitaille, *Synth. Met.*, 2008, **158**, 577–584.
109 D. Z. Chen, L. Zhang, P. Ning, H. Z. Yuan, Y. Zhang, M. Zhang, T. Fu and X. H. He, *Nano Res.*, 2021, **14**, 4885–4893.
110 V. Platonov, A. Nasriddinov and M. Rumyantseva, *Polymers*, 2022, **14**, 3481.
111 C. Y. Zhu, Q. Wang, G. R. Sun, S. Zhao, Y. Wang, T. H. Li, X. L. Hao, M. Artemyev and J. G. Tang, *Nanomaterials*, 2022, **12**, 2288.
112 G. Cadafalch Gazquez, V. Smulders, S. A. Veldhuis, P. Wieringa, L. Moroni, B. A. Boukamp and J. E. Ten Elshof, *Nanomaterials*, 2017, **7**, 16.
113 J. Chen, Z. Yu, C. Li, Y. Lv, S. Hong, P. Hu and Y. Liu, *Macromol. Mater. Eng.*, 2022, **307**, 2200057.
114 S. De Vrieze, T. Van Camp, A. Nelvig, B. Hagström, P. Westbroek and K. De Clerck, *J. Mater. Sci.*, 2009, **44**, 1357–1362.
115 S. Zahmatkesh, S. M. Zebarjad, M. E. Bahrololoom, E. Dabiri and S. M. Arab, *Ceram. Int.*, 2019, **45**, 2530–2541.
116 A. Asiri, R. H. Al-Ashwal, M. H. Sani and S. Saidin, *J. Phys.:Conf. Ser.*, 2019, **1372**, 012035.
117 S. I. Goreninskii, E. Y. Melnik, E. V. Plotnikov, D. D. Eskova, A. V. Zvyagin, E. N. Bolbasov and S. I. Tverdokhlebov, *Polymer*, 2024, **311**, 127549.
118 L. Safriani, M. I. Ardiansyah and F. Faizal, *J. Phys.:Conf. Ser.*, 2022, **2376**, 012014.
119 J. H. He, Y. Q. Wan and J. Y. Yu, *Polymer*, 2005, **46**, 2799–2801.
120 S. Basu, M. Jassal and A. K. Agrawal, *J. Text. Inst.*, 2013, **104**, 158–163.
121 C. Wang, W. Zhang, Z. H. Huang, E. Y. Yan and Y. H. Su, *Pigm. Resin Technol*, 2006, **35**, 278–283.
122 A. Haider, S. Haider and I. K. Kang, *Arabian J. Chem.*, 2018, **11**, 1165–1188.
123 J. M. Deitzel, J. Kleinmeyer, D. Harris and N. C. B. Tan, *Polymer*, 2001, **42**, 261–272.
124 J. Pelipenko, J. Kristl, B. Janković, S. Baumgartner and P. Kocbek, *Int. J. Pharm.*, 2013, **456**, 125–134.
125 D. Mailley, A. Hébraud and G. Schlatter, *Macromol. Mater. Eng.*, 2021, **306**, 2100115.
126 E. M. Çanga and F. C. Dudak, *Carbohydr. Polym.*, 2021, **264**, 117990.

 

127 M. I. Taborda, K. N. Catalan, N. Orellana, D. Bezjak, J. Enrione, C. A. Acevedo and T. P. Corrales, *ACS Omega*, 2023, **8**, 47883–47896.
128 M. Oroujzadeh, E. Mosaffa and S. Mehdipour-Ataei, *Surf. Interfaces*, 2024, **49**, 104386.
129 S. Sheikhi, A. Ghassemi, S. M. Sajadi and M. Hashemian, *Heliyon*, 2024, **10**, e23841.
130 J. Chang, Y. Liu, K. Heo, B. Y. Lee, S.-W. Lee and L. Lin, *Small*, 2014, **10**, 1920–1925.
131 Y. Guo, Y. Qiao, T. Cui, F. Wu, S. Ji, Y. Yang, H. Tian and T. Ren, *Appl. Sci.*, 2022, **12**, 4370.
132 M. Y. Lee, J. Hong, E. K. Lee, H. Yu, H. Kim, J. U. Lee, W. Lee and J. H. Oh, *Adv. Funct. Mater.*, 2016, **26**, 1445–1453.
133 F. Wang, J.-H. Zhang, S. Ke, J. Li, F. Huang, W. Cheng, Y. Shi and L. Pan, *Chem. Eng. J.*, 2025, **510**, 161620.
134 P. Samanta, V. Thangapandian, S. Singh, R. Srivastava, B. Nandan, C.-L. Liu and H.-L. Chen, *Soft Matter*, 2016, **12**, 5110–5120.
135 H. Cong, Y. Chang, R. Zhou, W. Zhang, G. Sun, P. Xu, Y. Qin, S. Ramakrishna, X. Liu and F. Wang, *Sci. China Mater.*, 2023, **66**, 3251–3260.
136 J. Y. He, P. L. Xu, R. F. Zhou, H. Li, H. L. Zu, J. Zhang, Y. B. Qin, X. H. Liu and F. Y. Wang, *Adv. Electron. Mater.*, 2022, **8**, 2100997.
137 J. Y. He, X. H. Liu, L. F. Song, H. Li, H. L. Zu, J. Y. Li, H. W. Zhang, J. Zhang, Y. B. Qin and F. Y. Wang, *J. Phys. Chem. Lett.*, 2021, **12**, 1339–1345.
138 A. Janotti and C. G. Van de Walle, *Phys. Rev. B: Condens. Matter Mater. Phys.*, 2007, **76**, 165202.
139 J. D. Hu, B. R. Li, X. Li, T. Y. Yang, X. G. Yang, J. F. Qu, Y. H. Cai, H. B. Yang and Z. Q. Lin, *Adv. Mater.*, 2024, **36**, 2412070.
140 C. Q. Li, Y. H. Cai, P. F. Hu, T. Liu, L. Zhu, R. Zeng, F. Han, M. Zhang, M. Zhang, J. K. Lv, Y. X. Ma, D. X. Han, M. Zhang, Q. J. Lin, J. W. Xu, N. Yu, J. W. Qiao, J. R. Wang, X. Zhang, J. L. Xia, Z. Tang, L. Ye, X. Y. Li, Z. H. Xu, X. T. Hao, Q. Peng, F. Liu, L. Guo and H. Huang, *Nat. Mater.*, 2025, **24**, 1626–1634.
141 D. W. S. Shi, X. Lv, Y. Yang, X. H. Zhang, Z. T. Tao, C. Xu and X. H. Rui, *Small*, 2024, **20**, 2402206.
142 L. Su, T. T. Yan, X. Y. Liu, F. Cao and X. S. Fang, *Adv. Funct. Mater.*, 2023, **33**, 2214533.
143 Y. Xue, T. Yang, E. H. Wang, H. Y. Wang, L. P. Zhu, S. Cao, X. M. Hou and K. C. Chou, *Nano Energy*, 2024, **125**, 109491.
144 N. K. Das, O. P. Nanda and S. Badhulika, *J. Power Sources*, 2024, **602**, 234303.
145 R. Cai, C. Liang, Y. Duan, Z. Zhao, X. Zhang, P. He, J. Yang, W.-Y. Lai, J. Wei and L. Tian, *FlexMat*, 2025, **2**, 225–283.
146 G. Li, *Light Sci. Appl.*, 2023, **12**, 24.
147 R. Shen, Y.-A. Li, W. Zhang, Y. Du, Y. Guo, Z. Zou, X. Liang, Q. Li, Y. Zhu, Y.-M. Zhang and S. X.-A. Zhang, *Chem. Eng. J.*, 2025, **511**, 161819.
148 K. Zhou, Z. Jia, X.-Q. Ma, W. Niu, Y. Zhou, N. Huang, G. Ding, Y. Yan, S.-T. Han, V. A. L. Roy and Y. Zhou, *Int. J. Extreme Manuf.*, 2023, **5**, 042006.
149 X. Chen, B. Chen, B. Jiang, T. Gao, G. Shang, S.-T. Han, C.-C. Kuo, V. A. L. Roy and Y. Zhou, *Adv. Funct. Mater.*, 2023, **33**, 2208807.
150 C. Zhu, H. Liu, W. Wang, L. Xiang, J. Jiang, Q. Shuai, X. Yang, T. Zhang, B. Zheng, H. Wang, D. Li and A. Pan, *Light Sci. Appl.*, 2022, **11**, 337.
151 S. Wen, Y. Liu, Y. Li, L. Xie, J. Li and J. Zhang, *Int. J. Extreme Manuf.*, 2024, **7**, 025506.
152 L. Zheng, Z. Liu, S. Xin, Q. Chen, J. Ming, L. Wu, J. Xu, P. Xu, K. Liu, R. Seeram and F. Wang, *Appl. Mater. Today*, 2024, **41**, 102424.
153 Y. Zhang, J. Xu, M. Wei, L. Wu, D. Ge, F. Xu, J. Ming, Y. Qin, S. Ramakrishna and F. Wang, *ACS Appl. Nano Mater.*, 2025, **8**, 5677–5684.
154 L. Zheng, R. Zhou, S. Xin, H. Cong, Y. Qin, P. Xu, X. Liu and F. Wang, *J. Mater. Chem. C*, 2023, **11**, 7098–7105.
155 W. Xiao, Y. Dong, R. Ci, G. Liu and F. Shan, *IEEE Trans. Electron Devices*, 2024, **71**, 6430–6434.
156 S. C. Ding, Z. Y. Lyu, H. Zhong, D. Liu, E. Sarnello, L. Z. Fang, M. J. Xu, M. H. Engelhard, H. Y. Tian, T. Li, X. Q. Pan, S. P. Beckman, S. Feng, D. Du, J. C. Li, M. H. Shao and Y. H. Lin, *Small*, 2021, **17**, 2004454.
157 H. H. Jin, X. Zhao, L. Liang, P. X. Ji, B. S. Liu, C. X. Hu, D. He and S. Mu, *Small*, 2021, **17**, 2101001.
158 L. Ding, L. Pei, S. H. Xuan, X. W. Fan, X. F. Cao, Y. Wang and X. L. Gong, *Adv. Electron. Mater.*, 2020, **6**, 1900653.
159 N. Ilyas, J. Y. Wang, C. M. Li, D. Y. Li, H. Fu, D. E. Gu, X. D. Jiang, F. C. Liu, Y. D. Jiang and W. Li, *Adv. Funct. Mater.*, 2022, **32**, 2110976.
160 H. Z. Shouval, S. S. H. Wang and G. M. Wittenberg, *Front. Comput. Neurosci.*, 2010, **4**, 19.
161 R. C. Froemke and Y. Dan, *Nature*, 2002, **416**, 433–438.
162 R. K. Mishra, S. Kim, S. J. Guzman and P. Jonas, *Nat. Commun.*, 2016, **7**, 11552.
163 J. Y. Wang, Z. Y. Wu, L. Pan, R. J. Gao, B. B. Zhang, L. J. Yang, H. Y. Guo, R. J. Liao and Z. L. Wang, *ACS Nano*, 2019, **13**, 2587–2598.
164 Y. Zhou, C. J. Wan, Y. S. Yang, H. Yang, S. C. Wang, Z. D. Dai, K. J. Ji, H. Jiang, X. D. Chen and Y. Long, *Adv. Funct. Mater.*, 2019, **29**, 1806220.
165 J. X. Nan, X. Guo, J. Xiao, X. Li, W. H. Chen, W. J. Wu, H. Liu, Y. Wang, M. H. Wu and G. X. Wang, *Small*, 2021, **17**, 1902085.
166 Y. Zhang, D. Chen, Y. Xia, M. Guo, K. Chao, S. Li, S. Ma and X. Wang, *Nano Energy*, 2025, **133**, 110486.
167 J. Qin, B. Sun, S. Mao, Y. Yang, M. Liu, Z. Rao, W. Lin, Y. Yang and Y. Zhao, *Mater. Today Chem.*, 2024, **37**, 101999.
168 F. H. Guo, W. Z. Yu, M. C. Zhang, B. Zhang, B. Hu, S. S. Li, J. Y. Jiang, A. K. Sun, Y. J. Liu and L. Z. Hao, *Small Methods*, 2025, **9**, 2402151.
169 J.-L. Meng, T.-Y. Wang, L. Chen, Q.-Q. Sun, H. Zhu, L. Ji, S.-J. Ding, W.-Z. Bao, P. Zhou and D. W. Zhang, *Nano Energy*, 2021, **83**, 105815.
170 X. Ren, X. He, Z. Duan, X. An, Y. Li, F. Gao, J. Zhang and P. Hu, *ACS Photonics*, 2024, **11**, 4990–4999.
171 Y. Meng, F. Z. Li, C. Y. Lan, X. M. Bu, X. L. Kang, R. J. Wei, S. Yip, D. P. Li, F. Wang, T. Takahashi, T. Hosomi,

K. Nagashima, T. Yanagida and J. C. Ho, *Sci. Adv.*, 2020, **6**, eabc6389.
172 L. R. Wu, S. W. Xin, R. J. Li, X. D. Zhang, M. Y. Wei, F. Y. Xu, J. Q. Xu, P. L. Xu, L. Liu, Y. B. Qin and F. Y. Wang, *Appl. Phys. Lett*, 2025, **127**, 203305.
173 Y. Wang, Z. Y. Lv, J. R. Chen, Z. P. Wang, Y. Zhou, L. Zhou, X. L. Chen and S. T. Han, *Adv. Mater.*, 2018, **30**, 1802883.
174 Z. Y. Nia, Y. Wang, L. X. Liu, S. Y. Zhao, Y. Xu, X. D. Pi and D. R. Yang, *Presented in part at the IEEE International Electron Devices Meeting (IEDM)*, San Francisco, California, 2018.
175 S. Y. Wang, C. S. Chen, Z. H. Yu, Y. L. He, X. Y. Chen, Q. Wan, Y. Shi, D. W. Zhang, H. Zhou, X. R. Wang and P. Zhou, *Adv. Mater.*, 2019, **31**, 1806227.
176 L. Yin, C. Han, Q. T. Zhang, Z. Y. Ni, S. Y. Zhao, K. Wang, D. S. Li, M. S. Xu, H. Q. Wu, X. D. Pi and D. R. Yang, *Nano Energy*, 2019, **63**, 103859.
177 M. Hellenbrand, *ECS Meeting Abstracts*, 2021, MA2021-01, 1014.
178 G. Abbas, M. Hassan, Q. Khan, H. Wang, G. Zhou, M. Zubair, X. Xu and Z. Peng, *Adv. Electron. Mater.*, 2022, **8**, 2101412.
179 S. Aftab, M. Zahir Iqbal, S. Hussain, H. H. Hegazy, F. Kabir, S. Hassan Abbas Jaffery and G. Koyyada, *Chem. Eng. J.*, 2023, **469**, 144039.
180 Z. Zheng, B. Qiao, Z. Han, J. Qiu, Y. Yao, C. Shu, Y. Liu, H. Hu, Y. Xu, B. Yu, D. Wang, M. Wang and Z. Li, *InfoMat*, 2025, **8**, e70089.
181 R. Yang, Y. Wang, S. Li, D. Hu, Q. Chen, F. Zhuge, Z. Ye, X. Pi and J. Lu, *Adv. Funct. Mater.*, 2023, **34**, 2312444.
182 M. T. Sharbati, Y. Du, J. Torres, N. D. Ardolino, M. Yun and F. Xiong, *Adv. Mater.*, 2018, **30**, 1802353.
183 W.-J. Lee, S.-H. Sohn and I.-K. Park, *Adv. Opt. Mater.*, 2025, **13**, 2402636.
184 K. Chen, Q. Dai, Y. Tian, W. Chen, C. Ai, Y. Cao, X. Yuan, Q. Wang, Y. Shi and Y. Li, *Adv. Funct. Mater.*, 2025, **35**, 2508673.
185 M. Zhou, Y. Zhao, X. Gu, Q. Zhang, J. Zhang, M. Jiang and S. Lu, *APL Photonics*, 2023, **8**, 076107.
186 Z.-X. Yin, H. Chen, S.-F. Yin, D. Zhang, X.-G. Tang, V. A. L. Roy and Q.-J. Sun, *Small*, 2025, **21**, 2412851.
187 S. K. Wen, L. H. Chen, J. Li and J. H. Zhang, *IEEE Trans. Electron Devices*, 2023, **70**, 6644–6650.
188 Y. Guo, F. Wu, G. H. Dun, T. Cui, Y. Liu, X. Tan, Y. Qiao, M. Lanza, H. Tian, Y. Yang and T. L. Ren, *Adv. Funct. Mater.*, 2023, **33**, 2208055.
189 Y. Chen, J. Xia, Y. Qu, H. Zhang, T. Mei, X. Zhu, G. Xu, D. Li, L. Wang, Q. Liu and K. Xiao, *Adv. Mater.*, 2025, **37**, 2419013.
190 Y. Zhu, B. Peng, L. Zhu, C. Chen, X. Wang, H. Mao, Y. Zhu, C. Fu, S. Ke, C. Wan and Q. Wan, *Appl. Phys. Lett*, 2022, **121**, 133502.
191 S.-K. Lee, Y. W. Cho, J.-S. Lee, Y.-R. Jung, S.-H. Oh, J.-Y. Sun, S. Kim and Y.-C. Joo, *Adv. Sci.*, 2021, **8**, 2001544.
192 W. Liu, C. Xu, W. Xie, J. Ye, Z. Zhu, Z. Lin and H. Chen, *FlexMat*, 2025, **2**, 153–164.
193 K. K. Kim, J. Bang, M. Kim, J. Jeong, I. Ha and S. H. Ko, *Nat. Mater.*, 2025, **25**, 463–471.
194 S. Zhang, J. Zhu, R. Qiu, D. Liu, Q. Ren and M. Zhang, *Adv. Mater.*, 2025, **37**, 18418.
195 O. Kwon, D. H. Lee, S. Oh, J. Yoon, H. B. Kim, J. H. Ahn, W. Park, H. S. Kim and B. Cho, *Adv. Funct. Mater.*, 2025, **36**, e13449.
196 Y. Xu, B. Wu, C. Hou, Y. Li, H. Wang and Q. Zhang, *FlexMat*, 2024, **1**, 248–257.
197 Y. Guo, Y. Qiao, T. Cui, F. Wu, S. Ji, Y. Yang, H. Tian and T. Ren, *Appl. Sci.*, 2022, **12**, 4370.
198 M. Shin, J. H. Song, G. H. Lim, B. Lim, J. J. Park and U. Jeong, *Adv. Mater.*, 2014, **26**, 3706–3711.
199 Q. Hu, G. He, B. He, Q. Gao, Y. Liu, G. Zhou and J. Yang, *IEEE Trans. Electron Devices*, 2024, **71**, 3258–3264.
200 T. T. Bui, J. Lee, D.-Y. Jeon, K. Kim, M. Rim, K.-U. Jeong and J.-H. Lee, *Adv. Mater. Technol.*, 2025, **10**, e00732.
201 L. Song, L. Luo, X. Li, D. Liu, N. Han, L. Liu, Y. Qin, J. C. Ho and F. Wang, *Adv. Electron. Mater.*, 2019, **5**, 1800707.
202 J. W. Baek, S. Han, S. E. Lee, J. Ahn, C. Park, J. S. Nam, Y. H. Kim, E. Shin, M. Kim, J.-S. Jang, J. Kim, H. J. Park and I.-D. Kim, *ACS Nano*, 2024, **18**, 19568–19580.
203 X. An, Y. Liu, Y. Sun, X. Zhang, Y. Liu, Y. Tao, L. Guo, X. Jiang and M. Gao, *Chem. Eng. J.*, 2024, **487**, 150675.
204 B. Nandhakumar, R. S. Ghuge, Y. Sivalingam and A. V. Radhamani, *Chem. Eng. J.*, 2025, **522**, 166388.
205 C. K. Qiu, L. Wang, F. An, H. Zhang, Q. R. Li, H. Z. Wang, M. J. Li, J. Y. Guo, P. L. Jia, Z. W. Liu, L. Zhu, W. Xu and D. Z. Zhang, *Rare Met.*, 2025, **44**, 1170–1181.
206 J. Liu, J. N. Zhang, Q. Yu, Y. M. Liu, X. L. Zhang, G. Q. Zhu, Y. M. Jia, H. B. Lu, J. Z. Gao, H. J. Wang and B. P. Zhu, *Adv. Funct. Mater.*, 2025, **35**, 2410833.
207 J. Huang, Y. Hao, M. Zhao, W. Li, F. Huang and Q. Wei, *ACS Appl. Mater. Interfaces*, 2021, **13**, 24774–24784.
208 Y. Yang, Y. Yang, J. Huang, S. Li, Z. Meng, W. Cai and Y. Lai, *Adv. Fiber Mater.*, 2023, **5**, 1505–1518.
209 S. Kumar, R. K. Jha, B. Thakur, T. Biswas, J. K. Anand, C. Soren, D. Banswar, S. Singh, S. Singh, S. Sinha-Ray and A. Goswami, *J. Mater. Chem. A*, 2025, **13**, 7786–7803.
210 X. Wang, X. Guan, Z. He, L. Li, Y. Gao, D. Tan, T. Yin, H. Fu and B. Xu, *Nano Energy*, 2025, **142**, 111287.
211 S. Bairagi, I. Shahidul, C. Kumar, A. Babu, A. K. Aliyana, G. Stylios, S. C. Pillai and D. M. Mulvihill, *Nano Energy*, 2023, **118**, 108962.
212 Y. C. Qi, J. X. Jiang, F. Chen, J. H. Zhou, J. H. Liang, J. J. Fu, Y. Q. Yang, Y. C. Ding, Z. J. Zheng and Q. Y. Huang, *Small*, 2025, **21**, 2504556.
213 S. Wang, P. Fan, W. Liu, B. Hu, J. Guo, Z. Wang, S. Zhu, Y. Zhao, J. Fan, G. Li and L. Xu, *ACS Nano*, 2024, **18**, 31737–31772.
214 C. Liu, S. Wang, N. Wang, J. Yu, Y.-T. Liu and B. Ding, *Nano-Micro Lett.*, 2022, **14**, 194.

 